Technische Universität München
Physik Department
Lehrstuhl für Topologie Korrelierter Elektronensysteme

Thermodynamic and Kinetic Stability of Magnetic Skyrmions

Dipl.-Phys. Univ. Marco Halder

Vollständiger Abdruck der von der
Fakultät der Physik der Technischen Universität München
zur Erlangung des akademischen Grades eines

Doktors der Naturwissenschaften (Dr. rer. nat.)

genehmigten Dissertation.

Vorsitzender:		Prof. Dr. Michael Knap
Prüfer der Dissertation:	1.	Prof. Christian Pfleiderer, Ph.D.
	2.	Priv.-Doz. Hans-Gregor Hübl

Die Dissertation wurde am 02.07.2018 an der Technischen Universität München eingereicht und durch die Fakultät für Physik am 05.10.2018 angenommen.

Contents

Motivation

The study of phase transitions is at the very heart of condensed matter physics and essential for many aspects of modern technology. Phase transitions are governed by thermodynamics and kinetics, determining whether and how a transition occurs. The fundamental principle of thermodynamic stability is that a system strives for the lowest state of free energy. As such, the change of a control parameter such as temperature, pressure or magnetic field, may induce a spontaneous phase transition if the free energy of a new state falls below the free energy of the current state. Two types of phase transitions with fundamentally different transition kinetics may be distinguished, namely discontinuous and continuous phase transitions, denoted as first-order and second order phase transitions, respectively. While second-order phase transitions evolve by a continuous evolution of states, with each state lower in free energy, first-order phase transitions occur via a fluctuation-induced nucleation and subsequent growth [1–3]. This involves the formation of an energetically costly interface surrounding the nucleus, imposing an energy barrier which kinetically stabilizes the current state. The emergence of hysteresis, supercooling, or superheating effects at a first-order phase transition is thus a manifestation of kinetic stabilization and, in fact, sufficient to identify a phase transition as first-order [3] Moreover, the presence of energy barriers in the phase transition allows the formation of glasses and other kinetically arrested states. It must be noted that other aspects such as disorder may itself affect or impose an energy barrier, as it is observed for example in disorder-broadened first-order phase transitions [3–6]. In contrast to thermodynamically stable states, kinetically arrested states are subject to relaxation effects due to thermal agitation. The study of the relaxation dynamics may thus give access to the associated energy scales.

Magnetic hysteresis shares many similarities with first-order phase transitions. The magnetization process in bulk magnets is a nucleation and growth process of magnetic domains and has been described by theories akin to those for first-order phase transitions [7]. The presence of hysteresis itself is a clear indicator for long-lived non-equilibrium states [8]. Analogous to first-order phase transitions, magnetic hysteresis is accompanied by thermal relaxation effects which are commonly referred to as magnetic viscosity, with first reports dating back to 1893 [9]. Magnetic viscosity is of utmost importance for modern technology as it limits the stability of information stored in magnetic recording

media [10, 11]. In this context, the relaxation arises from an Arrhenius type thermal activation process across energy barriers, known as Néel-Brown relaxation in the field of magnetism. Ultimately, the underlying physics is governed by Kramers escape rate theory [11, 12], which has applications in various fields of science including chemistry, biology and even financial sciences[13–15]. Experimentally, the relaxation is often found to follow a logarithmic dependence on time, arising from a broad distribution of activation energies. Owing to the universality of the underlying physics, similar relaxation behavior is found in a variety of systems including elastic deformations, dielectrics, superconductors, spin-glasses, and ferromagnets [9, 16–25].

This thesis concerns with magnetic skyrmions, a noncollinear magnetic texture consisting of nanometer-sized spin-whirls, which has attracted considerable interest due to its potential for future spintronics applications. Due to the nontrivial topology of the spin texture, magnetic skyrmions are robust against perturbations, prohibiting a continuous transformation into a topologically trivial state, such as a ferromagnet. Based on the nontrivial topology of the magnetic texture, the nucleation and annihilation of skyrmions thus involves a first-order phase transition and is therefore subject to hysteresis, relaxation, and metastability. Using measurements of the magnetization, ac-susceptibility, nonlinear ac-susceptibility, and specific heat we investigate the formation and decay of skyrmion order, addressing the thermodynamic and kinetic stability of skyrmions.

This thesis is structured as follows. In Chapter. 1, we begin with brief introduction of the nucleation and growth mechanism, magnetic viscosity and magnetocrystalline anisotropy, which serves as a basis for the interpretation of experimental data presented in later chapters. In Chapter 2 we provide a compact overview of the material class of cubic chiral magnets, addressing the generic phase diagram, the skyrmion lattice, emergent electrodynamics, topological stability and nucleation and annihilation of skyrmions. This is followed by a specific introduction of $Fe_{1-x}Co_xSi$ and Cu_2OSeO_3, the chiral magnets investigated during this thesis. In Chapter 3 we summarize the experimental methods, techniques and analyses used throughout this thesis. In Chapter 4 we report a comprehensive study of a nonequilibrium skyrmion phase in the chiral magnet $Fe_{0.5}Co_{0.5}Si$, addressing the stability and the underlying energetics of the metastable state. In Chapter 5, we present an extensive study of the magnetic properties of Cu_2OSeO_3, focussing on a second skyrmion phase and a tilted-concial phase, stabilized by cubic anisotropies. In Chapter 6, we end this thesis with a summary and a brief outlook.

CHAPTER 1

Nucleation and Relaxation Kinetics

In this chapter we briefly introduce the nucleation and growth mechanism, the theory of magnetic viscosity and magnetocrystalline anisotropy. This serves as a basis for the understanding of the following chapters.

1.1 Nucleation and Growth

First-order phase transitions are a common phenomenon in nature. An archetypal example of a first-order transition is the freezing of water or analogously the inverse process, the melting of ice. It is well known that first-order phase transitions proceed via nucleation and subsequent growth of thermal fluctuation induced embryos of the stable phase within an unstable medium. In the following, we will attempt to give a brief introduction to classical nucleation theory, the most common approach to describe the nucleation process [26].

Let g_α and g_β be the free energy densities of the low and high-temperature state, respectively, with $g_\alpha \leq g_\beta$ at low temperatures and $g_\beta \leq g_\alpha$ at high temperatures. The mean field transition temperature, T_m, is then defined as the intersection of g_α and g_β. Starting in the β-state at high temperatures, the formation of a nucleus of volume V of the low temperature phase changes the total free energy by

$$\Delta G_V = V(g_\alpha - g_\beta) = V\Delta g \tag{1.1}$$

and may lower the free energy as soon as the temperature falls below T_m. The creation of a nucleus, however, inevitably involves the formation of an energetically costly interface between both phases with

$$\Delta G_\mathrm{S} = S \cdot \sigma \tag{1.2}$$

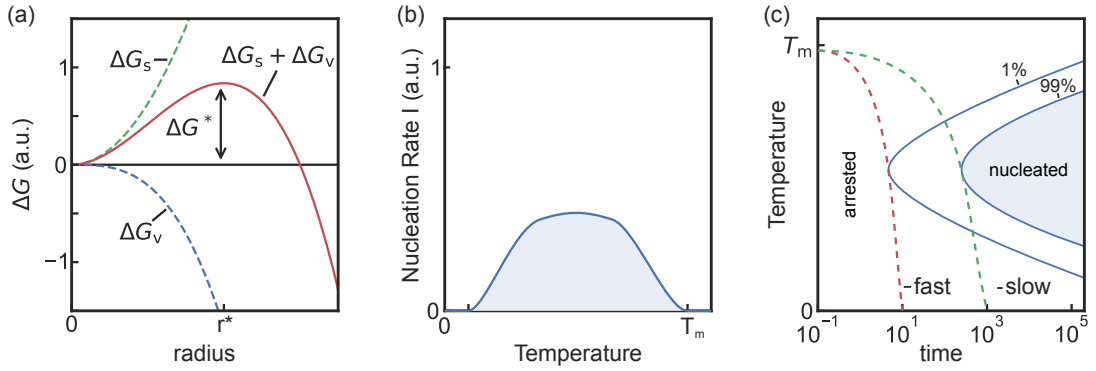

Figure 1.1: (a) Volume fraction, ΔG_V, surface fraction, ΔG_S and total free energy contribution, ΔG, of a spherical nucleus as a function of radius, r. The total free energy contribution reaches its highest value at the critical radius, r^*. (b) Schematic of the nucleation rate as a function of temperature. (c) Schematic of time-temperature-transformation diagram. Solid blue lines mark a 1 % and 99 % degree of transformation from the high-temperature state to the low-temperature state. Red and green dashed line correspond to a fast and slow cooldown. The high-temperature state is kinetically arrested if cooled faster than the critical cooling rate, as illustrated by the dashed red line.

where S is the surface of the nucleus and $\sigma > 0$ a specific surface energy density, e.g., the surface tension in liquid-solid transformations. Assuming, for the sake of simplicity, a spherical nucleus with radius r, the total change in energy reads

$$\Delta G = \Delta G_S + \Delta G_V = \underbrace{4\pi r^2 \cdot \sigma}_{\text{surface}} + \underbrace{\frac{4}{3}\pi r^3 (g_\alpha - g_\beta)}_{\text{volume}} . \tag{1.3}$$

Shown in Fig. 1.1(a) are the volume fraction, ΔG_V, surface fraction, ΔG_S and the total free energy contribution ΔG as a function of the nucleus radius. The free energy reaches a maximum at a critical radius r^*, with

$$\Delta G^* = \frac{16}{3}\pi \frac{\sigma^3}{\Delta g} \tag{1.4}$$

and corresponds to the thermodynamic energy barrier, depending on the thermodynamic driving force. A second activation energy that must be considered is the kinetic activation energy, Q, for the formation of the interfaces. It corresponds to the activation energy of diffusion in structural transitions. The nucleation rate is then given by the sum of both

activation energies [27], reading

$$I = I_0 \exp\left(-\frac{Q + \Delta G^*}{k_\mathrm{B} T}\right) = I_0 \cdot \underbrace{\exp\left(-\frac{Q}{k_\mathrm{B} T}\right)}_{\text{kinetic}} \cdot \underbrace{\exp\left(-\frac{\Delta G^*}{k_\mathrm{B} T}\right)}_{\text{thermodynamic}}. \tag{1.5}$$

A schematic of the nucleation rate as a function of temperature is shown in Fig. 1.1(b). Close to the mean-field ordering temperature, the nucleation rate is small, owing to the small thermodynamic driving force, yielding a sizeable thermodynamic energy barrier. With decreasing temperature, the energy difference between both phases increases and the thermodynamic energy barrier is reduced. As a result, the nucleation rate increases notably. With decreasing temperature, the kinetic energy barrier gains in importance and ultimately leads to a reduction in the nucleation rate towards low temperatures. As a result, the phase transformation depends decisively on the cooling rate.

Shown in Fig. 1.1(c) is a schematic of a time-temperature-transformation diagram, illustrating the cooling rate dependence. Solid lines indicate the temperature-dependent time required to transform 1 % or 99 % of the high-temperature phase into the low-temperature phase. A complete transformation would take place, if cooled sufficiently slow, indicated with a green dashed line. The high-temperature phase, however, is arrested if cooled faster than the critical cooling rate, shown as a dashed red line. In liquid to solid transitions, this mechanism leads to the formation of structural glasses [3].

The critical cooling rate may vary drastically between different systems and depends sensitively on the kinetic energy barrier, i.e., the diffusivity in structural transitions [28] In strong glass formers, such as O-terphenyl, cooling at moderate rates is sufficient to arrest the high-temperature state [3]. Metallic glasses, in contrast, require violent quenching of the high temperature state ($\geq 1 \times 10^6\,\mathrm{K/\,min}$) [3].

As a final remark, the discussion so far concerned a homogeneous nucleation process, that may occur anywhere throughout the sample. In contrast, the formation of nuclei at defects or surfaces may reduce the thermodynamic energy barrier by decreasing the surface between both phases and is known as heterogeneous nucleation. Heterogeneous nucleation may occur earlier but is limited in location.

1.2 Magnetic Viscosity

Relaxation effects are observed in many areas of physics and often share a generic mechanism. A logarithmic relaxation as it is often found in magnetic relaxation experiments is also found in elastic deformations, dielectrics, superconductors, spin-glasses and ferromagnetic fine particles [9, 16–25]. In ferromagnets it is termed "magnetic after effect" ("magnetische Nachwirkung") or magnetic viscosity and may be explained by a broad but flat distribution of activation energies. In this section, we introduce the theory of magnetic viscosity and show how the logarithmic relaxation arises naturally from a broad but flat distribution of activation energies, which are triggered by a relaxation front advancing logarithmically in time. This section serves as a basis for the interpretation of magnetic relaxation data, presented in a later chapter.

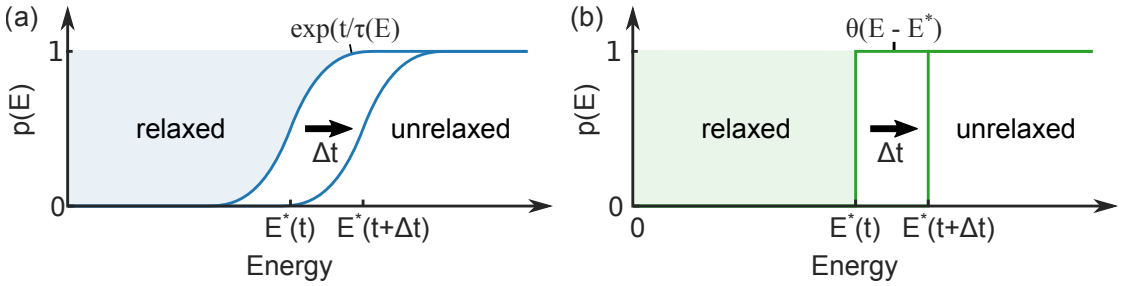

Figure 1.2: Schematics of the advancement of the relaxation front (a) and the approximation (b) with time. Figure adapted from [24, p. 335].

In magnetic relaxation experiments, the magnetization is often found to follow a logarithmic time dependence, that may be described by the relation

$$M(t) = K + S\ln(t/t_0), \tag{1.6}$$

with the magnetic viscosity constant S and material and experiment specific parameters K and t_0. This is the widely used magnetic viscosity relation. The divergence for $t \to 0$ and $t \to \infty$, however, shows that Eq. 1.6 is necessarily an approximation. Moreover, a change in t_0 is indistinguishable from a shift in K. An enhanced approximation, especially at short times, is given by

$$M(t) = M(0) + S\ln(1 + t/t_0), \tag{1.7}$$

with $M(0)$ corresponding to the magnetization at the starting time, and the time constant t_0. Here, $M(0)$ and t_0 have distinct roles but are still empiric parameters.

Following G. Bertotti, the emergence of a logarithmic time dependence may be understood as follows [24, pp. 329–346]: The lifetime associated with an activation energy in the interval $E \to E + dE$ may be written as

$$\tau(E) = \tau_0 exp\left(\frac{E}{k_B T}\right), \tag{1.8}$$

where τ_0 represents attempt time. The change in magnetization may be expressed as

$$\Delta M(t) = M(0) - M(t) = \int_0^\infty \Delta m(E)\left[1 - exp\left(-\frac{t}{\tau(E)}\right)\right] n(E)dE, \tag{1.9}$$

where $\tau(E)$ is given by Eq. 1.8. Here, $\Delta m(E)$ corresponds to the change in magnetic moment associated with the metastable units governed by the activation energy E and $n(E)$ is normalized according to

$$N = \int_0^\infty n(e)dE \tag{1.10}$$

to the number of metastable units per unit volume N. Eq. 1.9 may be simplified by introducing the effective energy barrier distribution,

$$p(E) = \frac{\Delta m(E) n(E)}{N \langle \Delta m \rangle} \tag{1.11}$$

with the normalization condition

$$\int_0^\infty p(E) dE = 1. \tag{1.12}$$

and the average magnetic moment per metastable unit

$$\langle \Delta m \rangle = \frac{1}{N} \int_0^\infty \Delta m(E) n(E) dE. \tag{1.13}$$

This gives

$$\Delta M(t) = N \langle \Delta m \rangle \left[1 - \int_0^\infty \exp\left(-\frac{t}{\tau(E)} \right) p(E) dE \right] \tag{1.14}$$

As $\tau(E)$ depends exponentially on E, this leads to a sharp cutoff around the Energy E^* for which $\tau(E) = t + \tau_0 \approx t$ with

$$E^*(t) = k_\mathrm{B} T \ln(1 + \frac{t}{\tau_0}), \tag{1.15}$$

depending logarithmically on time.

A schematic of the exponential in Eq. 1.14 as a function of energy is depicted in Fig. 1.15(a). For $E > E^*$ the exponential is almost 1 corresponding to the unrelaxed units. Conversely, for $E < E^*$ the exponential drops to zero corresponding to the units that are relaxed. The transition occurs in an energy region of about $k_\mathrm{B}T$ with respect to E^*. Therefore, if the distribution is approximately constant in an energy region of the order of $k_\mathrm{B}T$, the exponential in Eq. 1.14 can be replaced by a step function $\theta(E - E^*(t))$ indicated in Fig. 1.15(b). The magnetic relaxation itself is triggered by the logarithmic evolution of E^* with time. With the definition of E^*, the relaxation of the magnetization may be written as

$$\Delta M(t) = N \langle \Delta m \rangle \int_0^{E^*(t)} p(E) dE \tag{1.16}$$

The relaxed magnetization, expressed in terms of the average value of the energy distribution,

$$p_\mathrm{avg}(E) = \frac{1}{E^*} \int_0^{E^*} p(E) dE \tag{1.17}$$

is given by

$$\Delta M(t) = N \langle \Delta m \rangle \, p_{\mathrm{avg}}(E^*) k_{\mathrm{B}} T \ln\left(1 + \frac{t}{\tau_0}\right) \tag{1.18}$$

This means that whenever $p_{\mathrm{avg}}(E^*)$ is flat one expects a logarithmic dependence on time. Note that, experimentally it is difficult to determine the initial magnetization at $t = 0$ due to the fact that changing the field or temperature as well as the measurement take time. As a result one does not observe $M(t) - M(0)$ but $M(t + t_0) - M(t_0)$ instead, representing

$$M(t) = M(0) + Sln(1 + t/t_0), \tag{1.19}$$

with $t_0 \gg \tau_0$. This corresponds to the relaxation relation considered above (c.f. Eq. 1.7).

1.3 Magnetocrystalline Anisotropy

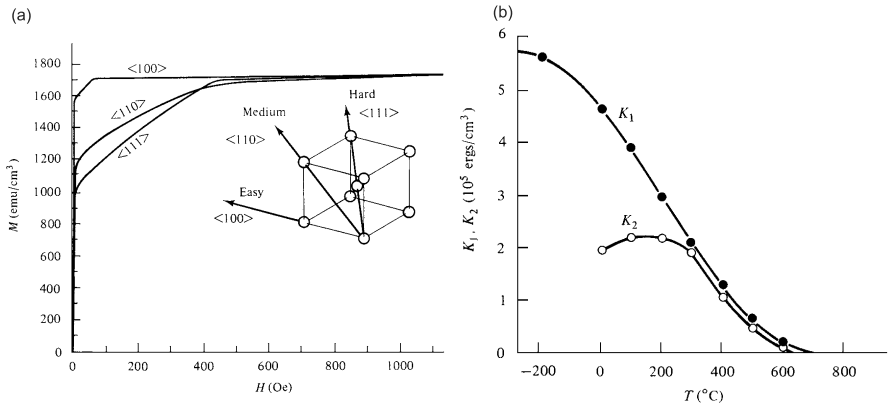

Figure 1.3: (a) Magnetization curves of single crystalline iron. (b) Temperature dependence of the anisotropy constants of iron. Graphs taken from [29, p. 199] and [29, p. 228], respectively.

Magnetocrystalline anisotropy is the directional dependence of the magnetic properties of a material in relation to its crystal lattice and was first discovered by K. Beck in 1918 in cubic Fe-Si steel single crystals [30]. Magnetic anisotropy is of utmost importance in modern technology. Being a prerequisite for magnetic hysteresis in ferromagnets, magnetic anisotropy plays an important role in magnetic memory data storage technology and permanent magnets.

As an example, the field dependent magnetization curves for all major cubic axes of single crystalline iron are shown in Fig. 1.3(a). The magnetic field required to saturate iron is lowest in the $\langle 100 \rangle$ orientation and highest in the $\langle 111 \rangle$ orientation. The $\langle 100 \rangle$ axis is therefore referred to as *easy*, the $\langle 111 \rangle$ as *hard*.

Table 1.1: Directions of easy, medium, and hard magnetization in a cubic crystal [29, p. 202]

.

K_1	+	+	+	-	-	-
K_2	$+\infty$ to $-9/4K_1$	$-9/4K_1$ to $-9K_1$	$-9K_1$ to $-\infty$	$-\infty$ to $9/4\|K_1\|$	$9/4\|K_1\|$ to $9\|K_1\|$	$9\|K_1\|$ to $+\infty$
EASY	$\langle 100 \rangle$	$\langle 100 \rangle$	$\langle 111 \rangle$	$\langle 111 \rangle$	$\langle 110 \rangle$	$\langle 110 \rangle$
MEDIUM	$\langle 110 \rangle$	$\langle 111 \rangle$	$\langle 100 \rangle$	$\langle 110 \rangle$	$\langle 111 \rangle$	$\langle 100 \rangle$
HARD	$\langle 111 \rangle$	$\langle 110 \rangle$	$\langle 110 \rangle$	$\langle 100 \rangle$	$\langle 100 \rangle$	$\langle 111 \rangle$

The orientation dependence may be described by an additional phenomenological contribution to the free energy F, denoted as F_{aniso}, taking the symmetries of the crystal lattice into account. The free energy,

$$F = F_{\text{iso}} + F_{\text{aniso}}, \tag{1.20}$$

is thus comprised of an isotropic and an anisotropic contribution. The anisotropy energy, F_{aniso}, is typically expanded in powers of the direction cosines of $\mathbf{M}$ relative to the crystal axes. For cubic crystals, the allowed terms up to 6th order are given as

$$F_{\text{aniso}} = K_0 + K_1(\hat{M}_x^2\hat{M}_y^2 + \hat{M}_y^2\hat{M}_z^2 + \hat{M}_z^2\hat{M}_x^2) + K_2(\hat{M}_x^2\hat{M}_y^2\hat{M}_z^2) + ... \tag{1.21}$$

with the direction cosines defined as

$$\hat{M}_i = \frac{M_i}{|\mathbf{M}|}. \tag{1.22}$$

Higher order anisotropies can be neglected in most cases. The isotropic K_0 constant does not generate a direction dependency and is therefore ignored. The easy, medium and hard axis of the system is thus determined by the values of K_1 and K_2, were six different cases can be distinguished, summarized in Table 1.1.

Note that the expansion in direction cosines is ambiguous and different symmetry equivalent definitions of the anisotropy energy can be used. E.g. an up to a constant equivalent fourth order term is

$$K_1'(\hat{M}_x^4 + \hat{M}_y^4 + \hat{M}_z^4). \tag{1.23}$$

K_1 and K_1' are related as follows

$$K_1 = -2K_1'. \tag{1.24}$$

The anisotropy constants typically have a strong temperature dependence and vanish at the transition temperature. This is shown for iron in Fig. 1.3(b). As a consequence, the magnetic properties can change dramatically with temperature. Therefore, it is of great interest to determine the anisotropy constants as a function of temperature.

CHAPTER 2

Chiral Magnets

This chapter introduces the class of cubic chiral magnets which includes a variety of materials with different electronic properties, notably metals, semiconductors, and insulators. Nonetheless, the magnetic properties show a remarkably universal behavior, which we introduce in the following chapter. This chapter is organized as follows: We begin with an introduction of the generic magnetic phase diagram in Sec. 2.1. Next, in Sec. 2.2 we introduce the skyrmion lattice in bulk systems, followed by a brief introduction of the emergent electrodynamics in Sec. 2.3. In Sec. 2.4 we address the concept of topological stability, followed by discussion of the nucleation and annihilation mechanism of magnetic skyrmions in Sec. 2.5. We complete the chapter with a discussion of the material specifics of $Fe_{1-x}Co_xSi$ in Sec. 2.6 and Cu_2OSeO_3 in Sec. 2.7, respectively.

2.1 Generic Magnetic Phase Diagram

Cubic chiral magnets share a lack of inversion symmetry in their crystal structure, with most known materials belonging to space group $P2_13$. The only exceptions so far are the recently discovered β-Mn type Co-Zn-Mn alloys crystalizing in space groups $P4_132$ or $P4_332$ [32–34]. While containing a large variety of different material classes such as metals (e.g. MnSi), semi-metals (e.g. $Fe_{1-x}Co_xSi$) or even insulators (e.g. Cu_2OSeO_3), cubic chiral magnets are exceptionally similar in their magnetic properties, resulting in a generic phase diagram illustrated in Fig. 2.1.

The magnetic properties of these materials arise from a well-defined hierarchy of energy scales formed by the ferromagnetic exchange, the Dzyaloshinskii-Moriya interaction, and magnetocrystalline anisotropy, listed in decreasing order [35]. The magnetic properties of cubic chiral magnets may be described elegantly in the framework of a phenomenological Ginzburg-Landau theory. The free energy density may be expanded in terms of a dimensionless order parameter vector field ϕ, related to the magnetization as $M = \mu\phi$

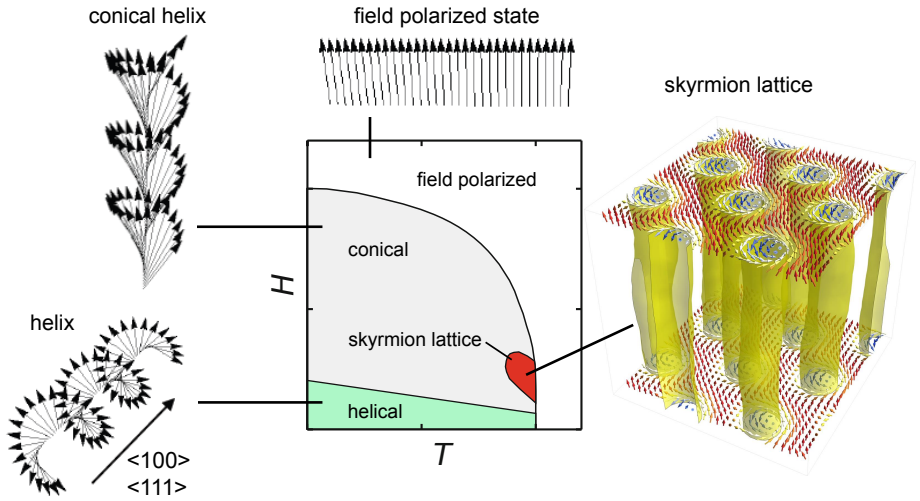

Figure 2.1: Generic magnetic phase diagram of the cubic chiral magnets with weak cubic anisotropies. Schematics visualize the spin configurations of the individual phases. The phase diagram comprises a helimagnetic state at low fields, a conical state at intermediate fields, a field-polarized state at high fields and low temperatures, and the skyrmion lattice state in finite fields, just below the ordering temperature. Figure adapted from Ref. [31, p. 3].

with $\mu = \mu_B/f.u.$, i.e. one Bohr magneton per formula unit. The free energy density up to fourth order in ϕ reads [31, p. 6]

$$f = \frac{r}{2}\phi^2 + \frac{u}{4!}(\phi^2)^2 - \underbrace{\mu_0\mu\phi\mathbf{H}}_{\text{Zeeman}} + \underbrace{\frac{J}{2}\left[(\nabla\phi_x)^2 + (\nabla\phi_y)^2 + (\nabla\phi_z)^2\right]}_{\text{Exchange}} \tag{2.1}$$

$$+ \underbrace{D\phi(\nabla\times\phi)}_{\text{Dzyaloshinskii-Moriya}} + \underbrace{\frac{J_{\text{cub}}}{2}\left[(\partial_x\phi_x)^2 + (\partial_y\phi_y)^2 + (\partial_z\phi_z)^2\right]}_{\text{Exchange Anisotropy}} + \ldots\,, \tag{2.2}$$

where, the first and second term represent the mean-field Landau parameters with $r = r_0(T - T_c)$ tuning the phase transition and $u > 0$ ensuring the stability of the system. These terms are sufficient for a qualitative description of most magnetic properties. For a quantitative description, however, additional terms might be necessary such as higher order anisotropies, dipolar interactions, or thermal fluctuations.

On the largest scale, ferromagnetic exchange favors a parallel alignment of the spins, while the Dzyaloshinskii-Moriya interaction, resulting from the lack of inversion symmetry, favors a perpendicular arrangement of the spins. This results in long wavelength modulated magnetic textures with a characteristic length scale given by the wave vector $|\mathbf{Q}| = D/J$ [31, p. 33] and ultimately leads to a helical ground state in zero field, depicted schematically in Fig. 2.1.

Due to cubic symmetry, several energetically degenerate helix orientations exist, leading

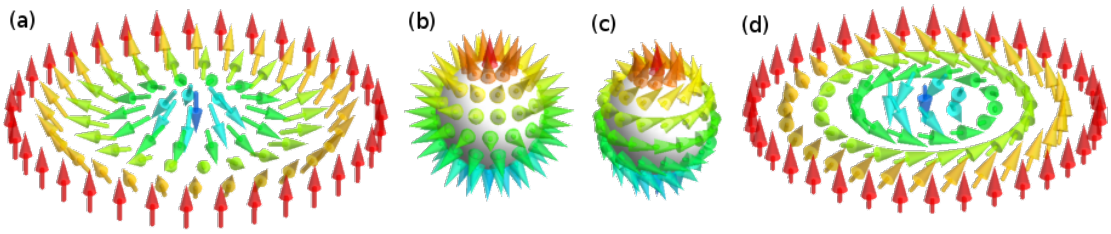

Figure 2.2: Skyrmions in real space and order parameter space. Achiral Néel skyrmion in real space (a) and order parameter space (b). Chiral Bloch skyrmion in order parameter space (c) and real space (d). Figure adapted from Ref. [42].

to a multi-domain ground state with the propagation vectors either aligned along the $\langle 100 \rangle$ or the $\langle 111 \rangle$ directions [36]. The exchange anisotropy, representing the leading order gradient term of the cubic anisotropy, is sufficient to lift the rotational degeneracy of the helical state in zero field, selecting either a $\langle 100 \rangle$ or $\langle 111 \rangle$ propagation [36]. As a function of increasing magnetic field, the helices start to deform and transform into a single domain conical state at the critical field H_{c1}. A further increase in field leads to a closing-in of the spins into field direction, collapsing into a field polarized state at the upper critical field H_{c2}.

In a small temperature and field region in the vicinity of the ordering temperature, T_c, a small phase pocket exists, hosting the skyrmion lattice phase. It was first discovered in MnSi in 2009 using small-angle neutron scattering [37] and consists of a two-dimensional triangular lattice of skyrmions in a plane perpendicular to the external magnetic field. Almost twenty years earlier, inspired by vortex lattices in type-II superconductors, Bogdanov and coworkers expanded the Bak-Jensen model of chiral magnets and showed that skyrmionic solutions with skyrmions on a triangular lattice could be thermodynamically stable in finite field ranges if uniaxial anisotropies are present [38–40]. The skyrmion lattice phase in the cubic chiral magnets, however, turned out to be stabilized by thermal fluctuations instead of uniaxial anisotropies. This is reflected by the existence of the skyrmion lattice phase for all field directions relative to the crystal lattice [37, 41].

2.2 Magnetic Skyrmion Lattice

Skyrmions were first proposed in a theoretical model of nucleons by Tony Skyrme in 1962 [43]. Skyrme showed that nucleons could emerge as quantized topological soliton solutions of the pion field. Since then, the concept has expanded into a wide variety of fields in physics, such as astrophysics, string-theory, and condensed-matter physics [37, 44, 45]. In the context of this study, we are concerned with magnetic skyrmions, a whirling spin texture, in which stability and dynamic properties are strongly determined by the non-trivial topology. The latter is reflected by the fact that it's impossible to continuously deform the topologically non-trivial texture of a magnetic skyrmion into a trivial texture such as a ferromagnet.

The topology of a magnetic texture is characterized by its topological index, a quantized

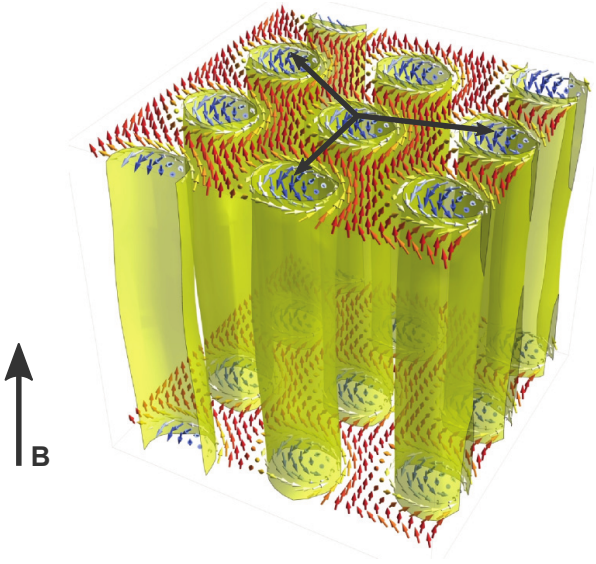

Figure 2.3: Illustration of the spin structure of a triangular skyrmion lattice. The spin structure may be approximated as a superposition of three helical modulations within a plane perpendicular to the external magnetic field. The propagation direction of each helix is indicated as a black arrow. Figure from Ref. [46].

integer number also referred to as winding number or topological charge. It can be understood by surjectively mapping the magnetic texture onto a unit sphere in order parameter space [42]. The topological index that classifies these mappings is defined as:

$$n = \frac{1}{4\pi} \int \mathbf{M} \left(\partial_x \mathbf{M} \times \partial_y \mathbf{M} \right) \mathrm{d}x \, \mathrm{d}y \tag{2.3}$$

with $n = \pm 1$ in case of skyrmions. It counts the number of times, the magnetic texture wraps the unit sphere.

A skyrmionic texture in real space, as shown in Fig. 2.2(a), is equivalent to a hedgehog in order parameter space, shown in Fig. 2.2(b), completely wrapping the unit sphere once. In contrast, topologically trivial magnetic textures, such as ferromagnets or helices, do not entirely cover the unit sphere.

Aside from the achiral skyrmion, shown in Fig. 2.2(a), also called Néel skyrmion, another topologically equivalent skyrmion exists, the so-called Bloch skyrmion. This chiral skyrmion may be constructed by combing the hedgehog of Fig 2.2(b), as shown in Fig 2.2(c), and projecting it back into real space (Fig 2.2(d)). Chiral skyrmions are the prevalent type of skyrmions in cubic chiral magnets, the material class investigated in this work.

In three-dimensional chiral magnets, skyrmions form tube-like magnetic structures, where the two-dimensional spin structure is stacked ferromagnetically along a specific direction, typically defined by the magnetic field. Similar to Abrikosov lattices in type-II superconductors, the skyrmions arrange as two-dimensional triangular lattices, illustrated

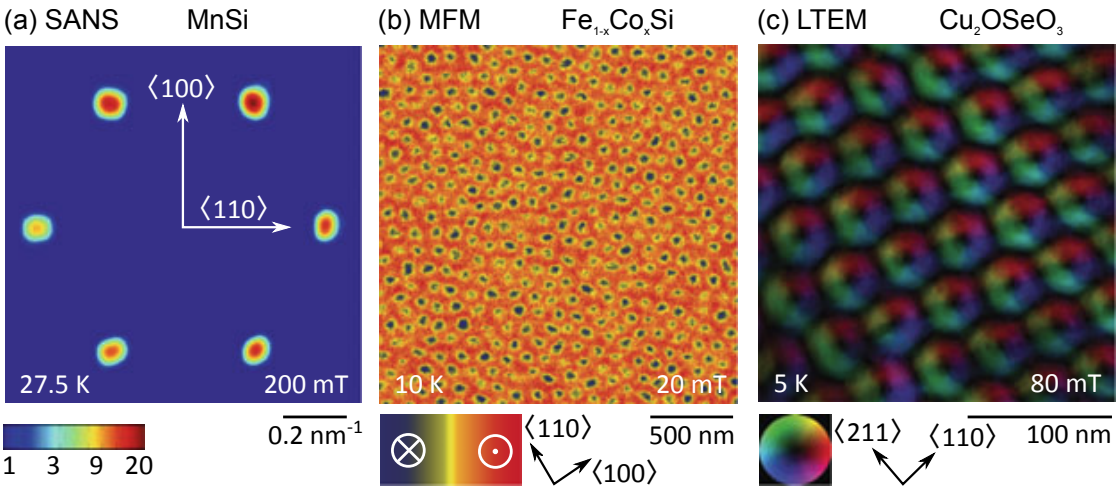

Figure 2.4: Typical measurement data of the skyrmion lattice, probed by small-angle neutron scattering (SANS) [37, 47] (a), magnetic force microscopy (MFM) [46] (b) and Lorentz force transmission electron microscopy (LTEM) [49, 50] (c). Figure adapted from Ref. [31].

in Fig. 2.3. Due to its periodic arrangement, the skyrmion lattice may be described as a series expansion in reciprocal space. To first order in q, the skyrmion lattice may be approximated as a superposition of a ferromagnetic component and three helical modulations at an angle of 120° within a plane perpendicular to the external magnetic field. The propagation direction of each helix is indicated in Fig. 2.3 by a black arrow. To accurately describe the field dependence of the spin texture, however, higher orders are necessary [47, 48].

Experimentally, the skyrmion lattice has been investigated with a variety of techniques. Three prominent examples are shown in Fig. 2.4. The first detection of a skyrmion lattice was reported in a seminal work of Mühlbauer and coworkers, using small-angle neutron scattering on MnSi [37]. Scattering techniques, such as small-angle neutron scattering (SANS), probe the skyrmion lattice in reciprocal space. The periodic nature reveals itself as a sixfold scattering pattern, as shown in Fig. 2.4(a). Additionally, weak higher-order scattering has been identified in MnSi in a subsequent high-precission SANS study [47].

The first real-space observation of a skyrmion lattice reported shortly afterwards was by Yu and coworkers using Lorentz-transmission electron microscopy (LTEM) on thinned $Fe_{1-x}Co_xSi$ samples [50]. LTEM is a sensitive tool to probe the in-plane spin arrangement but is limited to thin samples. A typical LTEM image is shown in Fig. 2.4(c). Another real-space technique is magnetic force microscopy (MFM). MFM probes the out-of-plane magnetization at the surface of a sample and in contrast to LTEM, it is not limited to thinned samples. A typical MFM recording of a skyrmion lattice is presented in Fig. 2.4(b) [46].

2.3 Emergent Electrodynamics

A particular consequence of the topological nature of magnetic skyrmions is their emergent electrodynamics. When a conduction electron travels through a slowly varying topologically nontrivial magnetic texture, it's spin continually adapts adiabatically to the local magnetic environment, illustrated in Fig. 2.5(a). In doing so, the spin picks up a geometric phase, the so-called Berry phase. The effects of the Berry phase pickup may be elegantly described as an Aharonov-Bohm phase arising from a fictitious magnetic field $\mathbf{B}^{\text{em}}$ acting on the electron [51]. Following Refs. [51–53], the emergent magnetic field exerts a fictitious Lorenz force

$$\mathbf{F} = -e\mathbf{v_s} \times \mathbf{B}^{em} \tag{2.4}$$

with $\mathbf{v_s}$ being the conduction electron velocity, which leads to an additional contribution to the Hall resistivity, the so called topological Hall resistivity[51, 52]

$$\rho_{xy}^{\text{top}} = PR_0B_z^{\text{em}} \tag{2.5}$$

with the normal Hall constant, R_0, and the effective spin polarization ratio, P. The emergent magnetic field B_z^{em} is given by

$$\mathbf{B}^{\text{em}} = \Phi_0\mathbf{\Phi} \tag{2.6}$$

Here, $\Phi_0 = h/e$ is the flux quantum of a single skyrmion and $\mathbf{\Phi}$ is the winding density defined by

$$\Phi^{\mu} = \frac{1}{8\pi}\epsilon_{\mu\nu\lambda}\hat{n} \cdot (\partial_{\nu}\hat{n} \times \partial_{\lambda}\hat{n}), \tag{2.7}$$

where $\epsilon_{\mu\nu\lambda}$ is the antisymmetric unit tensor and $\hat{n} = \mathbf{M}/|M|$ the magnetic unit vector.

The topological Hall effect was first measured by A. Neubauer and coworkers investigating MnSi [51]. They detected a topological Hall resistivity of 4.5 nΩ cm, as shown in Fig. 2.5(b) and (c), thereby providing the first experimental evidence of the non-trivial topological nature of magnetic skyrmions. Further measurements by Ritz and coworkers on MnSi using hydrostatic pressure revealed an almost ten-times larger, generic topological Hall resistivity in the zero-temperature limit, equivalent to an emergent magnetic field of $B_{\text{eff}} = -13.15\,\text{T}$ [52]. They further showed that at elevated temperatures the intrinsic Hall resistivity is suppressed by finite temperature effects [52]. Measurements on nanostructured FeGe Hall bar devices revealed discretized steps in the topological Hall signal, related to the creation or annihilation of single skyrmions, which not only confirms the quantized nature, but also the feasibility of single skyrmion detection, a key ingredient for future spintronics applications [55].

Another remarkable aspect of skyrmion lattices are spin-transfer torque effects. In analogy to the magnetic structure exerting a force on the electron, the electron exerts a counter-force on the magnetic structure. This effect is well-known from ferromagnets, where spin-polarized currents are used to move magnetic domain walls and spin-transfer torque is now widely used in commercial STT-MRAM memory devices [56–60].

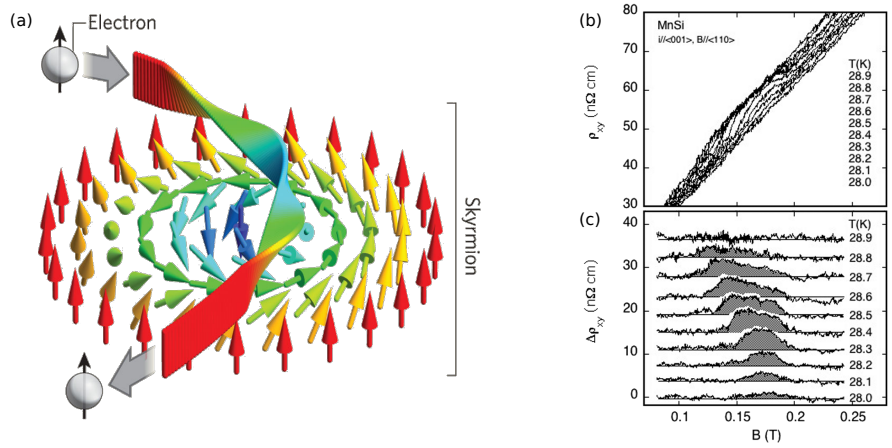

Figure 2.5: (a) Magnetic moment of the conduction electron adapting adiabatically to the local magnetic environment. (b) Hall resistivity as a function of field in MnSi in the temperature and field region around the skyrmion lattice phase. Topological contributions of the skyrmion lattice is visible as a tiny bump. (c) Topological contribution to the Hall resistivity as a function of field. Figures reproduced from (a) Ref. [54] and (b), (c) Ref. [51].

Spin-transfer torque effects in skyrmion lattices were first observed by Jonietz and coworkers. Using small-angle neutron scattering, they detected a rotation of the scattering pattern when the applied dc current exceeded a certain threshold. In contrast to ferromagnetic domain walls, however, the threshold current of $1 \times 10^6\,\mathrm{A\,m^{-2}}$ is nearly six orders of magnitude smaller, demonstrating the efficientcoupling of spin currents to the magnetic texture. Due to the limitations of small-angle neutron scattering not being able to detect translational movements of the skyrmion lattice, an additional small temperature gradient was applied causing gradients in the relevant forces, which in turn caused tiny rotational torques only strong enough to rotate the unpinned skyrmion lattice.

A skyrmion lattice drifting with the velocity v_d, were each skyrmion carries one quantum $-2\pi\hbar/q^e$ of emergent flux, implies in analogy to Faraday's law of induction, the emergence of an electric field,

$$\mathbf{E}^\mathrm{e} = \mathbf{v}_\mathrm{d} \times \mathbf{B}^\mathrm{e}, \tag{2.8}$$

which inherits the quantized nature of $\mathbf{B}^\mathrm{e}$ and has been confirmed in dc current biased Hall-effect measurements [61].

2.4 Topological Stability

The topological classification of field configurations is a powerful concept, that has successfully been applied to various fields in physics, including quantum field theory, liquid crystals, superfluids and magnetic systems [37, 46, 62–66]. For the topological comparison of field configurations, each field configuration is mapped from real space (or reciprocal

space), S^n, onto a target manifold constituting the order parameter space, S^m, according to $f : S^n \to S^m$. In magnetic systems, the mapping corresponds to the vector field of the magnetization $\mathbf{M}(\mathrm{r})$. If two mappings f and g, i.e. two magnetic textures, may be continuously deformed into each other without resorting to the discreteness of the lattice, then both mappings are homotopically equivalent and belong to the same homotopy group $\pi_n(S^m)$ [65].

Two different kinds of topological classifications may be further distinguished [46, 65, 67, Supp.]

(i) Non-singular configurations or textures, with a non-vanishing order parameter throughout the sample, such as sine-Gordon solitons or skyrmions, classified by the homotopy group $\pi_d(S^m)$ of order d, where d is the dimensionality of space [65, 67, 68].

(ii) Singular configurations or defects, with a vanishing order parameter at the core, classified by the lower homotopy groups $\pi_r(S^m)$ with lower order r, defined by the dimensionality of the defect, d', according to $r = d - d' - 1$ [65, 67].

A two-dimensional magnetic vortex in an ideal easy-plane ferromagnet is a perfect example of a singular topological defect. The rotation of the magnetization, $\mathbf{M}$, by 2π when traveling around the core implies a vanishing magnetization within the core. The topological classification of singular defects is achieved by mapping the order parameter on a surface enclosing the defect to a sphere in order parameter space. For a two-dimensional vortex, this implies a mapping of the order parameter on a path surrounding the vortex to a 1-sphere.

In contrast, a skyrmion is a perfect example of a non-singular solitonic spin texture. It is subject to a specific boundary condition, which is a constant magnetization at infinity, $m_\infty = \mathrm{const}$. The topological classification is realized by a stereographic projection of the entire spin structure onto a 2-sphere.

As a word of caution, although from a topological point of view both types of non-trivial field configurations contain an infinite energy barrier, the energy barrier in real physical systems is always finite [65, 66, 69].

First, the description of physical systems by an order parameter field implies a finite rigidity of the field, which in turn constrains the size of the energy barriers [66]. In magnetic systems, this rigidity is referred to as spin wave stiffness and defines the energy scale for a rupture of the continuous spin texture. This is corroborated, for example, by studies of magnetic vortex core reversal processes or annihilation of single skyrmions, where finite energy barriers, tightly linked to the spin-wave stiffness, were found [70–72]. Second, the energetic constraints in field configurations of restricted dimensionality, such as Ising systems or easy-plane ferromagnets are always finite, albeit large and the escape of the field configuration through restricted dimensions is possible. Third, the finite dimension of real samples provides another destruction path – the surface. The nontrivial defect may simply be pushed out through the surface. In small-scale systems, such as nano racetracks, this is considered a major relaxation mechanism for magnetic skyrmions

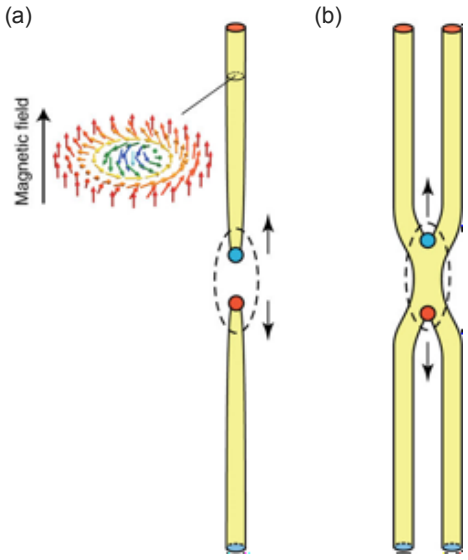

Figure 2.6: Schematic of monopole/antimonopole mediated skyrmion decay. Disintegration occurs either by pinching-off a single skyrmion tube (a) or coalescence of two skyrmion tubes (b). Monopoles and antimonopoles are displayed as red and blue dots, respectively. (a), (b) taken from Ref. [74].

[73]. Fourth, the discretization of the atomic lattice may itself limit the applicability of a continuum description.

2.5 Nucleation and Annihilation

Due to the topologically non-trivial structure, skyrmions cannot be created or destroyed by continuous deformation of the spin structure. Instead, more complex processes are involved. Theoretically, multiple pathways for the annihilation of skyrmions have been identified These include [73, 75, 76]

(i) compression of the skyrmion with a final collapse of the core,

(ii) annihilation of the skyrmion at the surface, pushing it out sideways, and

(iii) disintegrating the skyrmion by means of a singular, hedgehog-like defect, a so-called Bloch point.

The dominant mechanism depends on the dimensionality and the environment of skyrmions. The first two mechanisms are believed to play an essential role in two dimensional systems only [73]. In bulk systems, where skyrmions exist as tube-like spin whirls, the disintegration by means of Bloch-points, is believed to be the dominant relaxation mechanism. Here, two types of Bloch point mediated skyrmion decay may be distinguished: First, the coalescence of skyrmion tubes (Fig.4.12(b)) and second, the rupture of skyrmion tubes

(Fig. 4.12(a)). Since skyrmions carry a quantized emergent magnetic flux, Bloch points unwinding the skyrmion act as monopoles or anti-monopoles of the emergent field, either sourcing or sinking one quantum of the emergent magnetic flux [46]. Blue dots (anti-monopole) and red dots (monopole) in Fig. 2.6(a) and (b) indicate the emergent magnetic charge of the Bloch-point. The unwinding occurs as a two stage process, analogous to the nucleation and growth process in ordinary first-order phase transitions: First, a single (anti-)monopole is created at the surface or a monopole-antimonopole pair is created in the bulk. Second, the (anti-)monopole moves towards the surface, removing a single quantum of emergent flux. The direction of motion of (anti-)monopole is determined by the sign of the emergent magnetic charge with monopoles moving in field direction and antimonopoles against the field direction [46]. The driving force of the (anti-)monopoles results from the difference in free energy density between metastable and stable state Δg. The transformation of a skyrmion line segment of length x leads to a change in free energy $\Delta G \propto \Delta g \cdot x$ and may be described as a line tension [72]. Furthermore, theoretical studies of a single skyrmion within a helical environment have revealed an energy barrier of $E_{\mathrm{A}} \approx 6J$ for the nucleation of monopole-antimonopole pairs in zero field [72].

The nucleation or annihilation of skyrmions inevitably involves the formation of interfaces between the two phases. In view of the tube-like structure of skyrmions, the interface may be decomposed into a longitudinal and a radial contribution. The (anti-)monopoles discussed previously represent the longitudinal interface, terminating the skyrmion tubes. A second contribution arises from the radial adaption of the skyrmion spin texture to the surrounding environment and may impose an additional energy penalty. This is corroborated by the recent observation of the preferred formation of skyrmion clusters within the helical and conical phase, which minimize the surface area between skyrmion and non-skyrmion states [77, 78]. The radial interfacial energy is particularly important in a conical environment, since the longitudinal modulation of the conical helix is clearly incompatible with the rotational symmetry of a skyrmion. This leads to the formation of an energetically costly spiraling interface surrounding the skyrmion [78, 79]. Moreover, as shown in a recent preprint, the interfacial energy penalty reaches it's largest value at a magnetic field of $0.4 \cdot H_{\mathrm{c2}}$ [80]. Since the skyrmion lattice state and the conical state exhibit the smallest difference in free energy at the same magnetic field of $0.4 \cdot H_{\mathrm{c2}}$, this may explain the exceptional stability of non-equilibrium skyrmion lattices within the conical phase. Deleting a single skyrmion of a metastable skyrmion lattice at $H = 0.4 \cdot H_{\mathrm{c2}}$ thus requires the largest amount of interfacial energy while gaining the least amount of free energy from the conversion of a volume fraction into the conical state [80].

2.6 Chiral Magnetism in $Fe_{1-x}Co_xSi$

$Fe_{1-x}Co_xSi$ is a material that is particularly well suited for the study of nonequilibrium skyrmion states. The electric and magnetic properties of $Fe_{1-x}Co_xSi$, a pseudo-binary system of the paramagnetic insulator FeSi [81] and the diamagnetic metal CoSi [82], vary substantially with the doping concentration, x. The substitution of Fe atoms with Co atoms acts as electron doping, leading to an insulator-to-metal transition at $x = 0.02$ [83]

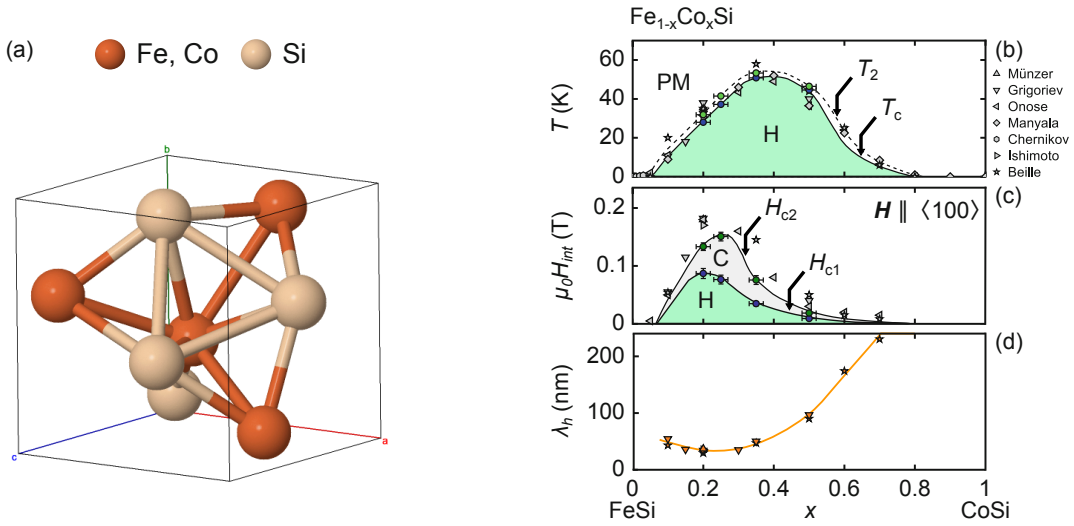

Figure 2.7: (a) Cubic crystal structure of $Fe_{1-x}Co_xSi$. (b)–(d) Ordering temperature, critical fields, and helix wavelength as a function of the doping concentration, x, in $Fe_{1-x}Co_xSi$. Figure adapted from Ref. [31, p. 14].

and chiral magnetism in a wide doping range from $0.05 \leq x \leq 0.7$ [84–86]. The variations of the magnetic ordering temperature, critical fields and helix wavelength as a function of x are shown in Fig. 2.7.

The ordering temperature, a measure of the exchange energy $J \propto k_B T_c$, reaches it's largest value of $T_c \simeq 60\,\mathrm{K}$ at a concentration of $x \simeq 0.5$, as shown in Fig.2.7(b). The helix wavelength,

$$\lambda = \frac{2\pi}{Q} = 2\pi \frac{J}{D}, \tag{2.9}$$

as shown in Fig.2.7(d), is determined by the ratio of J and D [31, 36, 87, 88] and varies from more than 200 nm above $x \approx 0.7$ down to 50 nm at $x \approx 0.25$, where D is the strongest in relation to J. This is consistent with the critical field,

$$H_{c2} \approx JQ^2 \frac{\phi}{\mu_0 \mu} \propto D^2/J, \tag{2.10}$$

being the largest at $x \approx 0.25$ [31, 88, 89].

A peculiar feature of $Fe_{1-x}Co_xSi$, is the formation of a metastable skyrmion lattice under field cooling. It has been demonstrated early that field cooling across the skyrmion lattice state using moderate cooling rates ($\approx 10\,\mathrm{K\,min^{-1}}$) is sufficient for the skyrmion lattice phase to survive as a metastable state down to lowest temperatures [90]. This is illustrated in Fig. 2.8(a), (b) showing the magnetic phase diagrams obtained after zero-field cooling and field cooling. Following zero-field cooling, the skyrmion lattice state is confined to a narrow region below the ordering temperature. In contrast, following field

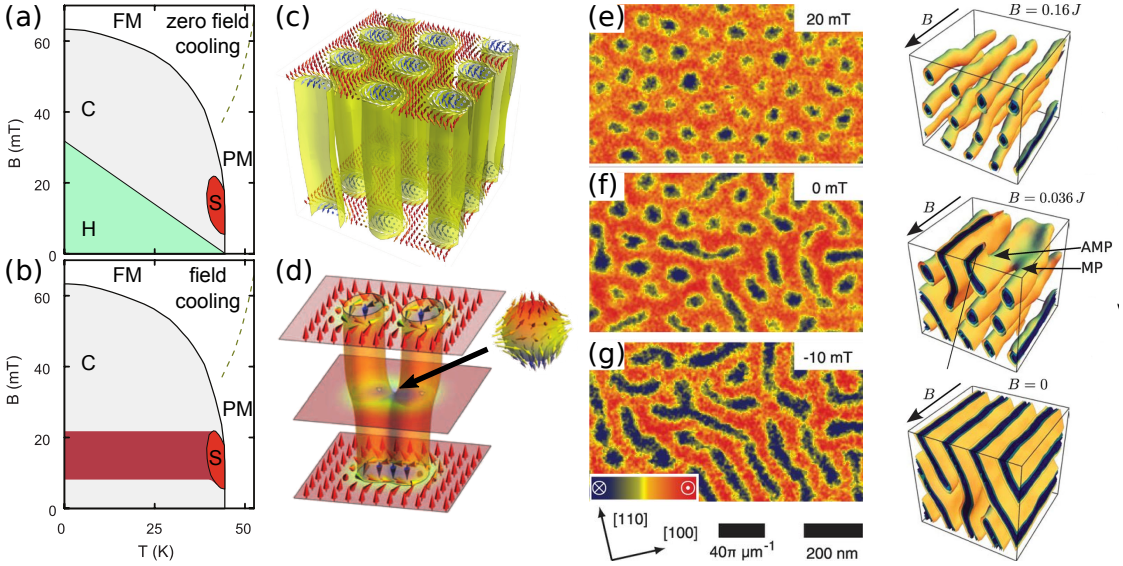

Figure 2.8: Magnetic phase diagram of $Fe_{0.5}Co_{0.5}Si$ with $\mathbf{B} \parallel \langle 110 \rangle$ after zero-field cooling (a) and field cooling (b). We distinguish helical (H, green), conical (C, grey), skyrmion lattice (S, red), paramagnetic (PM, white) and ferromagnetic state (FM, white). (c) Typical spin configuration of the skyrmion lattice. (d) Schematic of the coalescence of two skyrmions. A magnetic point defect carrying a single quantum of emergent magnetic flux, a so called emergent magnetic monopole, is situated at the merging point indicated with the black arrow. It acts as a zipper merging two skyrmions together. (e)–(g) Typical MFM images of the metastable skyrmion lattice recorded at 10 K after field cooling in $B = 20\,\mathrm{mT}$. With a successive reduction of field skyrmions (blue dots) start to merge, forming elongated structures resembling a strongly unordered helical state. (h) Contour surfaces of typical spin configurations extracted from Monte Carlo simulations, corresponding to the MFM measurement protocol.

cooling the skyrmion lattice extends down to lowest temperatures. Since the first discovery in $Fe_{1-x}Co_xSi$, metastable skyrmion lattices have been reported in various other systems, including MnSi, Cu_2OSeO_3, $Co_8Zn_8Mn_4$ and $Co_9Zn_9Mn_4$ [33, 34, 74, 91, 92]. In the β-Mn type materials, $Co_8Zn_8Mn_4$, and $Co_9Zn_9Mn_4$, field cooling across the stable skyrmion lattice phase is sufficient to generate the non-equilibrium skyrmion lattice phase, similar to $Fe_{1-x}Co_xSi$, while additional measures such as rapid quenching or electric fields are neccessary in MnSi [74, 91] and Cu_2OSeO_3 [93]. This is attributed to structural disorder, prevalent in $Fe_{1-x}Co_xSi$ and the β-Mn type chiral magnets.

The ability to create metastable skyrmion states is tightly linked to the topological protection of the non-trivial spin structure, providing a finite energy barrier separating the skyrmion state from trivial order (cf. Sec. 2.4). Microscopically, the transformation of skyrmions into trivial magnetic states involves the creation of high-energy transition states, which have been identified as hedgehog-like point defects, so-called Bloch points

[46, 72]. The topological unwinding process has been studied in $Fe_{0.5}Co_{0.5}Si$, using magnetic force microscopy, numeric simulations, and theoretical calculations [46]. By field cooling a $Fe_{0.5}Co_{0.5}Si$ sample in an applied field of $B = 20\,\mathrm{mT}$, Milde and coworkers were able to stabilize the skyrmion lattice down to 10 K, where the enhanced magnetic contrast enabled the detection with magnetic force microscopy. This allowed them to track the evolution of the magnetic state as a function of field on the surface of the sample. It is found that with a reduction of field, skyrmions disappear by coalescence forming elongated structures, resembling strongly disordered helices, as shown in Fig. 2.8(e)–(f). This process is mediated by Bloch points acting as zippers, merging two skyrmions. The coalescence of two skyrmions is shown schematically in Fig. 2.8(d). In contrast, the disintegration of skyrmions at high fields occurs by a Bloch point mediated pinch-off of single skyrmion strings [72, 74, 94]. Since each skyrmion is associated with a single quantum of emergent magnetic flux, Milde and co-workers realized that Bloch points unwinding the skyrmion act as monopoles or anti-monopoles of the emergent field, either sourcing or sinking one quantum of the emergent magnetic flux.

Lorentz transmission electron microscopy experiments on heavily thinned $Fe_{0.5}Co_{0.5}Si$ samples revealed an Arrhenius-type exponential decay of the skyrmion lattice [95]. Surprisingly, however, the exponential prefactor, τ_0, the so-called attempt time exhibits a strong field dependence as-well and leads to a drastic reduction of the lifetime of the skyrmion lattice in field regions where a long lifetime is expected from the activation energy alone. The experimentally observed attempt times vary largely, from ultra-fast values of $1 \times 10^{-37}\,\mathrm{s}$ to macroscopic timescales of $1 \times 10^{-2}\,\mathrm{s}$, as a result of entropic effects, known as enthalpy-entropy compensation.

In conclusion, $Fe_{1-x}Co_xSi$ serves as an ideal model system to study skyrmion lattices far from equilibrium. Nonetheless, previous studies on $Fe_{1-x}Co_xSi$ have been limited in a number of ways. First, a detailed evaluation of the thermodynamic signatures of the nonequilibrium skyrmion lattice state, such as the magnetization, is still missing in literature, as well as a thorough analysis of the stability of the metastable state against temperature and field. Most studies have only focussed on selected temperatures or fields. A direct comparison with metastable skyrmion states reported in other materials is therefore not possible. Secondly, the relaxation behavior and the underlying energetics have so far been studied in heavily thinned samples only, where the low dimensionality and the interfacial effects are known to alter the underlying energetics [50, 96, 97]. For instance, the heavily thinned samples show a significantly reduced ordering temperature ($\approx 20\,\%$) compared to the bulk [95]. Moreover, previous studies have not been able to quantitatively reproduce the theoretically predicted activation energies [72, 94, 95].

2.7 Chiral Magnetism in the Magnetoelectric Insulator Cu_2OSeO_3

The cubic chiral magnet Cu_2OSeO_3 is the second material investigated in this thesis. Cu_2OSeO_3, discovered in 1976 [99], was the first insulating material in which a skyrmion lattice [49, 100] was found. In contrast to the metallic chiral magnets MnSi, FeGe or

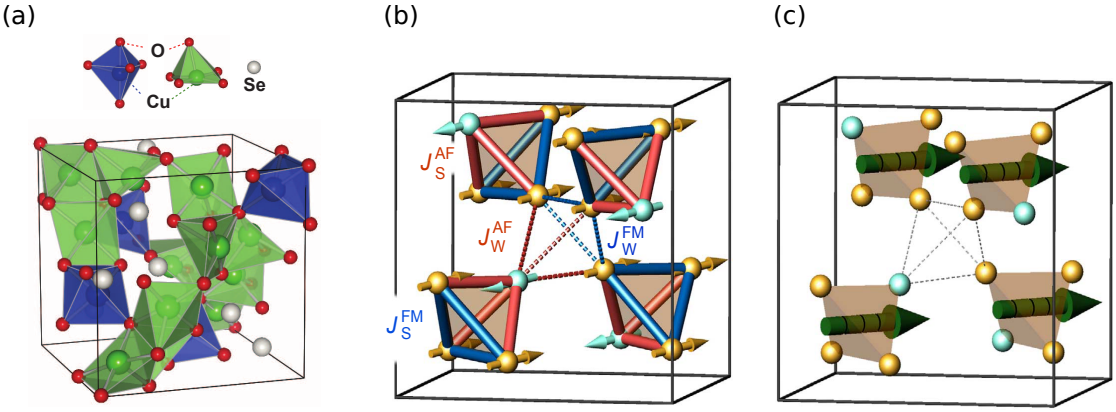

Figure 2.9: (a) Crystal structure of Cu_2OSeO_3. Two different Cu^{2+} sites may be distinguished, either surrounded by a square pyramid (green) or a bipyramid (blue) of oxygen atoms. (b) Crystallographic unit cell, containing four tetrahedra of strongly interacting magnetic Cu^{2+} ions. Ferromagnetic(red) and antiferromagnetic (blue) interactions between the Cu^{2+} lead to a 3-up-one-down spin arrangement in each tetrahedron. Interaction strength is indicated by the thickness of the connecting lines and much weaker between different tetrahedron. (c) The positions of the effective spins per tetrahedra (grey) correspond to the Mn sites in MnSi. Figure (a) adapted from Ref. [49]. Figure (b), (c) reproduced from Ref. [98].

$Fe_{1-x}Co_xSi$, Cu_2OSeO_3 has a more complex unit cell. The conventional cubic unit cell, with a lattice constant of $a = 8.928(3)$ Å [99], depicted in Fig. 2.9(a), consists of 8 formula units, resulting in 56 atoms instead of 8. Two different Cu^{2+} sites may be distinguished, either surrounded by a square pyramid or a trigonal bipyramid of oxygen ligands, in a 3:1 ratio [49, 101, 102].

Numerous measurements such as magnetization, high-resolution x-ray diffraction, neutron powder diffraction and NMR identified a ferrimagnetic order below $T_c = 58.8\,\mathrm{K}$ as the magnetic ground state [101, 103–105]. Bos, however, pointed out that ferrimagnetism in zero field is incompatible with the symmetries of the point group $P2_13$ without a reduction in symmetry of the crystal lattice [103, 106]. Nonetheless, no reduction in symmetry could be found [103–105]. This ambiguity was resolved by Seki et. al. who identified the ground state as a helical modulation, compatible with the symmetries [49].

The magnetic building blocks of Cu_2OSeO_3 are two kinds of Cu_4 tetrahedra with either strong or weak exchange coupling between the Cu^{2+} ions, depicted in Fig. 2.9(b). Both ferromagnetic and antiferromagnetic exchange is present according to DFT calculations by Janson and coworkers [98]. The interaction strength, indicated by the thickness of the connecting lines, is much weaker between Cu^{2+} ions of different tetrahedra compared to the strength of Cu^{2+} ions of the same tetrahedron. Quantum-mechanical treatment of a single tetrahedron yields a 3-up-1-down spin-triplet configuration with $S = 1$ separated

by a large gap of $\Delta = 275\,\mathrm{K}$ from the lowest-lying excitation [98]. The large excitation gap allows the treatment of the spin configuration as an effective moment. The positions of the effective triplets, shown in Fig. 2.9(c) as grey arrows, correspond to the Mn sites in MnSi. It is the Dzyaloshinskii-Moriya interaction between these effective triplets that leads to the helical ground state in Cu_2OSeO_3.

In contrast to many other chiral magnets, the insulating nature of Cu_2OSeO_3, in particular the large Mott gap, facilitates the investigation of magnetic properties using optical transmission techniques [107]. This has been exploited in various spectroscopic studies, ranging from microwave to optical frequencies [107–112].

In addition to chiral magnetic interactions, the cubic chiral space group $P2_13$ permits piezoelectricity and piezomagnetism. A prerequisite for the occurrence of magnetoelectric effects, however, are insulating electrical properties as the screening of electric fields by conduction electrons prohibits the magnetoelectric coupling in bulk metallic systems. Both requirements are met in Cu_2OSeO_3 and indeed magnetoelectric effects are observed at the onset of magnetic order [49, 103, 113, 114] and, in particular, within the skyrmion lattice phase [49, 114]. The electric field control of magnetic textures, most notably skyrmions, is of great relevance for future applications, as it provides a Joule-heating free control mechanism [115]. The effects of dc electric fields on skyrmion order in Cu_2OSeO_3 that have been demonstrated include manipulation of the skyrmion lattice orientation [116, 117] as well as enhanced or suppressed stability of the skyrmion phase [93, 118].

Given the similarity of the magnetic properties of Cu_2OSeO_3 with other chiral magnets, our recent discovery of two additional magnetic phases came as a major surprise [119]. Using small-angle neutron scattering (SANS), we have identified a second skyrmion phase, and a tilted conical phase, emerging at low temperatures for fields along $\langle 100 \rangle$ only.

Shown in Fig. 2.10 are schematics of the intensity patterns in reciprocal space of all five modulated magnetic structures and typical scattering images. Small colored spheres illustrate the location of scattering intensity in reciprocal space. The scattering intensities are located on the surface of a sphere, shown in blue shading, with a characteristic radius $|Q| \approx D/J$ (cf. Sec. 2.1). The crystallographic $\langle 100 \rangle$ orientations are visualized as black arrows. The detection plane, probed by the SANS experiment, is illustrated as a grey rectangle. The five different intensity patterns shown correspond to the well established intensity patterns of the helical (green), conical (grey) and high-temperature skyrmion (light red) state as well as the recently discovered tilted conical (dark grey) and low-temperature skyrmion state (dark red). In this context it is important to note the different orientations of the applied magnetic field and the detection plane with respect to the crystallographic orientations.

The domain structure of the helical state leads to scattering intensity along all $\langle 100 \rangle$ magnetic easy axes at a wavevector of $\pm Q$, as shown in Fig. 2.10(a1). Likewise, the single domain conical state, as shown in Fig. 2.10(a2), is characterized by scattering intensity at $\pm Q$ along the direction of the magnetic field. It is important to note that when the magnetic field is applied along a $\langle 100 \rangle$ axis, the conical intensity is indistinguishable from one of the three helical domains. In contrast, the scattering intensity of the conventional high-temperature skyrmion lattice, as shown in Fig. 2.10(a3), is located in a plane perpendicular to the magnetic field and obeys a sixfold symmetry that, unlike the helical

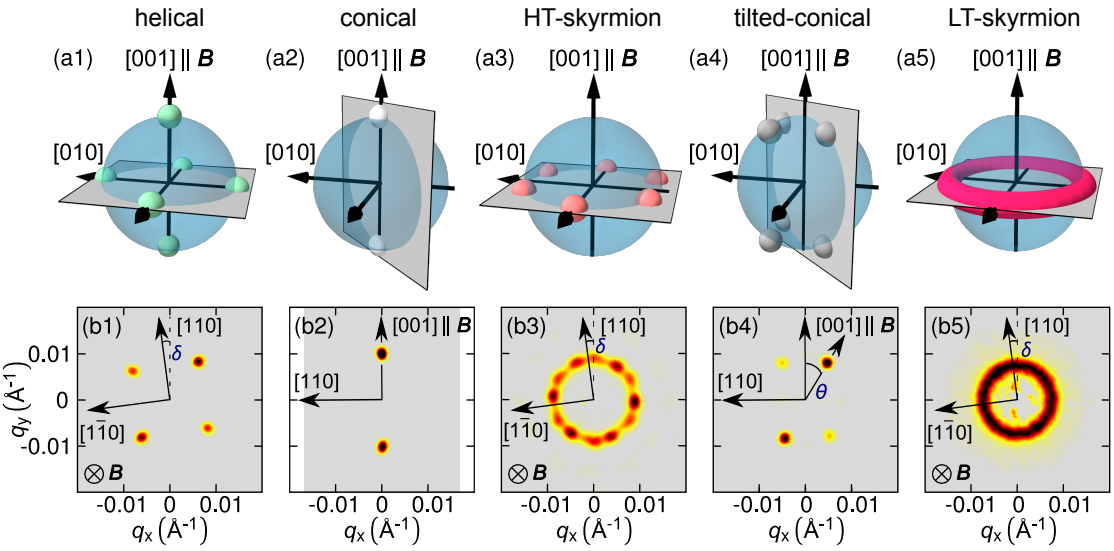

Figure 2.10: Schematics of the characteristic intensity patterns in reciprocal space and typical scattering images of helical [(a1), (b1)], conical [(a2), (b2)], high-temperature skyrmion [(a3), (b3)], tilted-conical [(a4), (b5)] and low-temperature skyrmion order [(a5), (b5)]. The blue shaded sphere indicates the characteristic length scale of the magnetic modulations. The grey plane corresponds to the detection plane. Note the direction of field with respect to crystal orientation and detection plane. Figure provided by Alfonso Chacon.

state, results from a single domain multi-q state.

The intensity patterns of the recently discovered tilted-conical state and the low-temperature skyrmion state, are illustrated in Fig. 2.10(a4) and (a5), respectively. The tilted conical phase is comprised of a conical modulation, tilted against the field direction, with the tilting angle increasing with field. In accordance with symmetry one observes four equivalent domains, yielding, in total, eight diffraction spots. Similar to the high-temperature skyrmion phase, the intensity of the low-temperature skyrmion phase emerges in a plane perpendicular to the applied magnetic field. Unlike the high-temperature skyrmion lattice, however, a ring of intensity instead of a sixfold pattern is observed, suggesting that, despite being the ground state, long range order is not yet fully developed. This is attributed to a weak effective anisotropy of the in-plane orientation of the skyrmion phase in the ⟨100⟩ orientation. It has been demonstrated that the hexagonal scattering pattern may be recovered by tilting the sample slightly against the field direction. This is attributed to a slight increase of the effective in-plane anisotropy with tilting due to in-plane magnetic field components, locking the skyrmion lattice in place.

The magnetic phase diagrams as determined by SANS are shown in Fig. 2.11(a)–(d) and were inferred from temperature sweeps following three distinct temperature vs. field protocols, namely zero-field cooled/field heated (ZFC/FH), field cooled/field heated

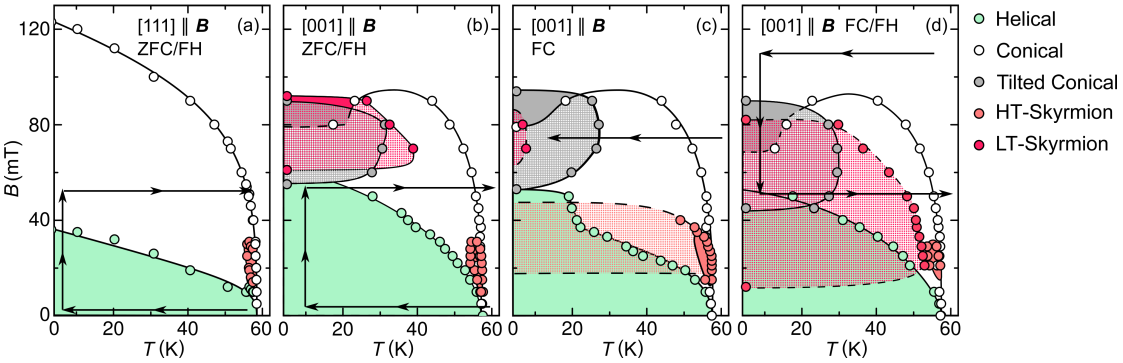

Figure 2.11: Orientation and history dependence of the magnetic phase diagrams inferred from small-angle neutron scattering. Three distinct temperature vs field protocols may be distinguished, namely zero-field cooled/field heated (ZFC/FH), field cooled/field heated and high-field cooled/field heated. (a) Magnetic phase diagram for $\mathbf{B} \parallel \langle 111 \rangle$ following ZFC/FH. (b)–(d) Magnetic phase diagram for $\mathbf{B} \parallel \langle 100 \rangle$ following ZFC/FH, FC/FH, and HFC/FH, respectively. Figure adapted from Ref. [119].

(FC/FH) and high-field cooled/field heated (HFC/FH).

Shown in Fig. 2.11(a) is the magnetic phase diagram observed for $\mathbf{B} \parallel \langle 111 \rangle$ under ZFC/FH. It resembles the generic phase diagram of the chiral magnets (cf. Sec. 2.1) with the helimagnetic ground state, the conical state at intermediate fields, the field polarized state at high fields and low temperatures, and the skyrmion lattice state at finite fields and high temperatures just below T_c.

In contrast, the magnetic phase diagram of the $\langle 100 \rangle$ orientation, observed under ZFC/FH, FC/FH and HFC/FH, as shown in Fig. 2.11(b)–(d), hosts two additional magnetic phases, namely a low-temperature skyrmion phase and a tilted-conical phase. The tilted conical phase emerges at the border of the conical to field-polarized transition, corresponding to a temperature and field region in which strong dissipation effects have been reported previously [120]. The second skyrmion phase emerges at low temperatures and finite fields, disconnected from the conventional high-temperature skyrmion phase and exhibits highly hysteretic phase boundaries. In all temperature vs field protocols, the intensity of the low-temperature skyrmion phase emerges within the temperature and field range of tilted-conical phase, but may exceed beyond as shown following ZFC/FH and HFC/FH in Fig. 2.11(b) and (d), respectively.

The formation of the low-temperature skyrmion phase and the tilted conical phase for field along $\langle 100 \rangle$ only demonstrates that cubic anisotropies must play an essential role. The importance of anisotropies is further underpinned by free energy calculations based on Ginzburg-Landau theory, including exchange, Dzyaloshinskii-Moriya, Zeeman and dipolar interactions as well as cubic anisotropies. Using realistic quantitative values

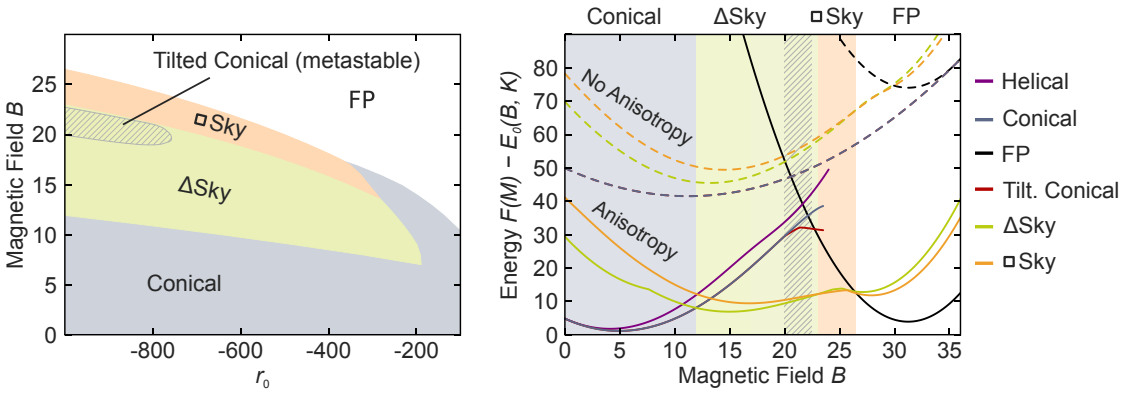

Figure 2.12: (a) Mean-field magnetic phase diagram as a function of r_0 and B for a cubic anisotropy of $K = 0.0004U$. We distinguish conical, tilted conical, field-polarized state (FP), triangular skyrmion lattice state (Δ-Sky), and square-lattice skyrmion state ($\square$-Sky). Hatched region marks the metastable tilted conical phase. (b) Field dependence of the free energy of various magnetic states at $r_0 = -1000D^2/J$ for vanishing cubic anisotropy (dashed lines) and easy $\langle 100 \rangle$ cubic anisotropy with $K = 0.0004U$ (solid lines). An offset function, $E_0(B, K) \propto B^2$, has been subtracted for clarity and the dashed lines are further shifted vertically. Figure adapted from Ref. [119].

and including the lowest order conventional cubic anisotropy term,

$$-K \int \left(M_x^4 + M_y^4 + M_z^4\right) \mathrm{d}V, \tag{2.11}$$

the experimentally observed phase diagram may be reproduced. This is shown in Fig. 2.12(a), presenting the mean-field phase diagram as a function of magnetic field, B, and the Landau parameter, r_0, tuning the distance to the ordering temperature, with large negative values corresponding to low temperatures. Similar to the experiment, skyrmion order is found at finite fields and low temperatures. The tilted conical phase, however, is identified as a metastable state. This is further illustrated in Fig. 2.12(b), showing the typical field dependence of the free energy of various magnetic states at low temperatures. Dashed lines correspond to free energy calculations for vanishing anisotropy ($K = 0$), while solid lines represent free energy calculations for finite cubic anisotropy with easy $\langle 100 \rangle$ anisotropy.

For vanishing anisotropy, only a conical ground state at low fields and a field-polarized state at high fields is found, consistent with literature [37]. In contrast, for sufficiently strong cubic anisotropy, with $K > K_\mathrm{c}$, a skyrmion ground states emerges. The critical anisotropy constant expressed in units of energy density, $K_{\sigma,\mathrm{c}} = K_\mathrm{c} \cdot M_\mathrm{s}^4$, reads

$$\frac{K_{\sigma,\mathrm{c}}}{\mu_0 H_{\mathrm{c2}}^{\mathrm{int}} M_\mathrm{s}} = 0.07, \tag{2.12}$$

with the saturation magnetization, M_s, and the upper critical field, $H_{\mathrm{c2}}^{\mathrm{int}}$, in case of vanishing anisotropy. The term $\mu_0 H_{\mathrm{c2}}^{\mathrm{int}} M_\mathrm{s}$, proportional to the ratio D^2/J [88], represents

the isotropic energy contribution necessary to transform the helimagnetic ground state at $B = 0$ into the field polarized state, assuming a vanishing anisotropy. Therefore, when the anisotropy energy along the $\langle 100 \rangle$ axis is larger than 7 % of the isotropic energy, a skyrmion phase may emerge.

In addition, at high fields, a metastable tilted conical phase is found, lower in energy than the conical or field-polarized state but always higher compared to skyrmion order. Unlike the skyrmion order, the transition from conical or field-polarized state into the tilted conical state involves a second-order phase transition and thus occurs immediately when the free energy of the tilted conical phase is lower, which may explain the phase coexistence observed experimentally.

Theoretically, triangular and square lattices of skyrmions, as well as modulated skyrmion textures (not shown), are found to be very close in energy. The ring-like scattering intensities observed experimentally make it difficult to identify the underlying skyrmion lattice structure unambiguously. Nonetheless, by tilting the sample slightly against the field direction, the hexagonal scattering pattern has been recovered. Moreover, preliminary results at high fields appear to be compatible with the square lattice arrangement.

In summary, strong magnetocrystalline anisotropies of the cubic chiral magnet Cu_2OSeO_3 yield two additional magnetic phases, that have not been observed in any other chiral magnet, namely a low-temperature skyrmion phase and a tilted-conical phase. The underlying generic mechanism may allow for similar observations in other materials if the cubic anisotropy is sufficiently strong. Nonetheless, important questions remain. These concern the thermodynamic signatures of the new phases and in particular the potential differences between the low-temperature skyrmion phase and the conventional skyrmion phase at high temperatures. In view of the highly hysteretic phase boundaries, the question remains concerning the extent of the thermodynamically stable field range of the low-temperature skyrmion phase. Either, the skyrmion order is thermodynamically stable in a wide field region, as predicted by theory, yet unable to nucleate in most regions or it is confined to a narrow field region but extends beyond it as a metastable state, implying an incomplete theory.

2.8 Aims and Objectives of this Thesis

The overall purpose of the present study is the investigation of thermodynamically and kinetically stabilized skyrmion order and is divided into two parts.

In the first part, presented in Chapter 4, we focus on a nonequilibrium skyrmion phase, emerging under field cooling in the chiral magnet $Fe_{0.5}Co_{0.5}Si$. We seek to investigate the stability of the nonequilibrium skyrmion phase against temperature and field and aim to identify the underlying energetics. We report a comprehensive magnetization and ac-susceptibility study of a nonequilibrium skyrmion lattice state in single crystal $Fe_{1-x}Co_xSi$. We find the metastable skyrmion lattice covering a significant portion of the phase diagram, extending into the field polarized state and even negative magnetic fields. The relaxation dynamics is studied with time-dependent magnetization measurements. Using master curve scaling, we extract the distribution of activation energies in zero

field. We find a barrier distribution consisting of a topological monopole-antimonopole nucleation barrier superimposed on a broad distribution of activation energies, yielding a skyrmion lattice state, stabilized beyond topological protection. We discuss, in detail, the field dependence of the metastable skyrmion phase and provide a direct comparison of nonequilibrium skyrmion lattice phases, where we identify generic behavior.

The second part of this thesis, reported in Chapter 5, focuses on a low-temperature skyrmion phase, thermodynamically stabilized by cubic anisotropies. We aim to identify the thermodynamic signatures of the low-temperature skyrmion phase and the tilted concial phase, recently discovered in Cu_2OSeO_3, and seek to gain further understanding of the strong hysteretic effects associated with the low-temperature skyrmion phase. Moreover, as cubic anisotropies are believed to play a key role in the stabilization of these novel phases, we set out to quantitatively infer the cubic anisotropy constant. We present a comprehensive study of the magnetic properties of single-crystal Cu_2OSeO_3, conducted in parallel with the neutron scattering study, reported in Ref. [119]. By means of measurements of the magnetization, ac-susceptibility, and specific heat, we track the influence of crystal orientation, cooling history and demagnetizing effects on the formation of skyrmion order. We find clear thermodynamic signatures of both low-temperature skyrmion phase as well as the tilted conical phase, restricted to the $\langle 100 \rangle$ orientation only, confirming the observations of neutron scattering. Based on the extensive data, we infer the magnetic phase diagram of Cu_2OSeO_3 for magnetic fields along the $\langle 111 \rangle$, $\langle 110 \rangle$, and $\langle 100 \rangle$ crystallographic orientation. Using two different temperature vs field protocols we investigate the hysteretic effects associated with the low-temperature skyrmion phase. We show that the strong dissipation effects reported earlier [121] originate from the tilted conical phase and are accompanied by signatures in higher harmonics of the ac-susceptibility. We further demonstrate the influence of demagnetizing fields on the low-temperature behavior, showing that signatures of the low-temperature skyrmion phase smear out and become undetectable at large demagnetizing field. From the magnetization measurements, we quantitatively estimate the cubic anisotropy constant and demonstrate how cubic anisotropies influence the energy landscape of chiral magnets. In addition, we study the nucleation of the low-temperature skyrmion phase through first-order reversal curve measurements and find compelling evidence that the low-temperature skyrmion lattice phase requires the tilted-conical phase to lower the nucleation barrier.

In conclusion, the first part of this study provides valuable insights into the stabilizing kinetics of nonequilibrium skyrmion phases and as metastable skyrmions are a key requirement for future spintronics applications, may contribute to the understanding of the underlying energetics, whose knowledge is fundamental for the engineering of future spintronic applications. The second part revisits the influence of cubic anisotropy on chiral magnets and establishes cubic anisotropy as a novel stabilization mechanism for skyrmion order, that has not been considered before.

CHAPTER 3

Experimental Methods

This chapter describes the methods used in the experimental studies and analyses reported in this thesis. Section 3.1 describes the characteristics of the samples investigated as part of this study. The measurement techniques and the characteristics of the experimental apparatus employed in this work are introduced in Sec. 3.2 and Sec. 3.3, respectively. Details of the data analysis are presented in Sec. 3.4

3.1 Samples

The study of the non-equilibrium skyrmion lattice state reported in Chapter 4, was conducted on a high-quality single crystal sample of $Fe_{0.5}Co_{0.5}Si$. A cuboid sample was cut from a large single crystal ingot, grown by optical float zoning. The sample dimensions as determined with an optical microscope are $3.4 \times 1.1 \times 1.1\,\mathrm{mm}^3$. A summary of the sample characteristics is given in Tab. 3.1. The sample was oriented in field such that $B \parallel \langle 110 \rangle$, with the $\langle 110 \rangle$ axis corresponding to a short axis of the sample. This orientation was chosen to match a neutron scattering experiment.

The study of the low-temperature skyrmion lattice in Cu_2OSeO_3, reported in Sec. 5, was carried out on five samples of high quality. All samples were prepared from large high-quality single crystal ingots, grown using a chemical vapor transport technique and are of comparable high quality. Oriented cuboid samples were cut using a wire saw and carefully grinded into the final dimensions. The majority of the data was collected on two samples, namely VTG-1-19 ($\langle 100 \rangle$ orientation) and VTG-1-20 ($\langle 110 \rangle$ and $\langle 111 \rangle$ orientation). Additional samples with different demagnetizing factors were investigated to study the effects of dipolar interactions. The sample masses, dimensions, orientations and demagnetizing factors are summarized in Table 3.1.

Table 3.1: Dimensions (a, b, and c), orientation of the magnetic field B, applied along the a dimension, corresponding demagnetization factors N and designation of the $Fe_{0.5}Co_{0.5}Si$ and Cu_2OSeO_3 single-crystal samples investigated as part of this study.

Material	Dimension (a [mm] x b[mm] x c[mm])	Orientation $B \parallel \langle hkl \rangle \parallel a$	N	Sample
$Fe_{0.5}Co_{0.5}Si$	$1.1 \times 3.4 \times 1.1$	$\langle 110 \rangle$	0.07	OFZ58-3-1-6
Cu_2OSeO_3	$3.00 \times 0.50 \times 0.50$	$\langle 100 \rangle$	0.07	VTG1-10-1
Cu_2OSeO_3	$1.85 \times 0.86 \times 0.78$	$\langle 100 \rangle$	0.18	VTG1-18-2
Cu_2OSeO_3	$0.86 \times 1.85 \times 0.78$	$\langle 100 \rangle$	0.39	VTG1-18-2
Cu_2OSeO_3	$0.15 \times 0.85 \times 1.88$	$\langle 100 \rangle$	0.77	VTG1-18-3
Cu_2OSeO_3	$1.87 \times 1.28 \times 1.53$	$\langle 100 \rangle$	0.28	VTG1-19
Cu_2OSeO_3	$1.76 \times 1.27 \times 1.74$	$\langle 110 \rangle$	0.29	VTG1-20
Cu_2OSeO_3	$1.74 \times 1.27 \times 1.76$	$\langle 111 \rangle$	0.30	VTG1-20

3.2 Experimental Techniques

In this section, we focus on the experimental techniques employed in the data acquisition during this work, namely magnetization, ac-susceptibility, nonlinear ac-susceptibility and specific heat measurements.

3.2.1 Extraction Magnetometry

Induction techniques are common methods to determine the magnetization of a sample. Moving a magnetic sample through a pickup coil generates, according to Faraday's law of induction, an electromotive force

$$\epsilon_{\mathrm{emf}} \propto \frac{\mathrm{d}\Phi}{\mathrm{d}t} \tag{3.1}$$

proportional to the change in magnetic flux. Two common methods based on this principle are the vibrating sample magnetometer and the extraction type magnetometer. In the vibrating sample magnetometer, the magnetic sample is moved periodically through a pick-up coil, generating a sinusoidal induction signal, proportional to the magnetization. In extraction type magnetometers, the sample is moved at a high velocity through a pick-coil. The magnetic moment is then determined by correlating the time-dependent induction signal with a reference curve.

3.2.2 AC Susceptibility

AC-susceptibility measurements are another important tool in the arsenal of a solid state physicist and are widely used in the study of magnetic materials and magnetic phase

transitions. In ac-susceptibility measurements, a small time varying magnetic field

$$H_{\mathrm{ac}}(t,\omega) = H_{\mathrm{ac}} \cos \omega t \tag{3.2}$$

is applied to the sample and the resulting time varying magnetic response

$$M(t,\omega) = M' \cos \omega t + M'' \sin \omega t \tag{3.3}$$
$$= H_{\mathrm{ac}}(\chi' \cos \omega t + \chi'' \sin \omega t) \tag{3.4}$$

is detected. Here, χ' and χ'' are the in-phase and out-of-phase components of the complex susceptibility $\chi_{\mathrm{ac}} = \chi' + i \cdot \chi''$. In the zero frequency limit, χ' corresponds to the differential susceptibility $\mathrm{d}M/\mathrm{d}H$ but differs for higher frequencies due to dynamic effects. Because of this, χ is also referred to as dynamic susceptibility. The out-of-phase component, χ'', is related to dissipation processes, mainly electrical eddy currents, viscous relaxation processes and weak field hysteresis [122]. Both eddy currents and viscous relaxation processes manifest as a frequency dependence in χ''. Contrary, the weak field hysteresis is independent of frequency but depends on the ac amplitude instead. As a final remark, viscous relaxation processes may also lead to quantitative differences between χ' and $\mathrm{d}M/\mathrm{d}H$.

Demagnetizing Effects

To determine the intrinsic properties of a magnetic material, demagnetizing effects must be taken into account. These influence the internal magnetic field, the magnetic susceptibility as well as the shape of the magnetization curve. To obtain the internal field, the external applied field must be corrected by the demagnetization field H_d resulting from the divergence of the magnetization vector on the surface:

$$H_{\mathrm{int}} = H_{\mathrm{ext}} + H_{\mathrm{d}}. \tag{3.5}$$

For uniformly magnetized samples the demagnetizing field is linearly related to the magnetization M by the so called demagnetization factor N, according to

$$H_{\mathrm{d}} = -NM. \tag{3.6}$$

The true internal susceptibility χ_{in} and the measured susceptibility χ_{ext} are related as follows [123]:

$$\chi_{\mathrm{in}} = \frac{\chi_{ext}}{1 - N\chi_{ext}} \tag{3.7}$$

For nonzero frequencies the susceptibilities are complex quantities. Separating equation 3.7 into real and imaginary part results in

$$\chi'_{\mathrm{int}} = \frac{\chi'_{ext} - N(\chi'^2_{ext} + \chi''^2_{ext})}{N^2(\chi'^2_{ext} + \chi''^2_{ext}) - 2N\chi'_{ext} + 1}, \tag{3.8}$$

$$\chi''_{\mathrm{int}} = \frac{\chi''_{ext}}{N^2(\chi'^2_{ext} + \chi''^2_{ext}) - 2N\chi'_{ext} + 1}. \tag{3.9}$$

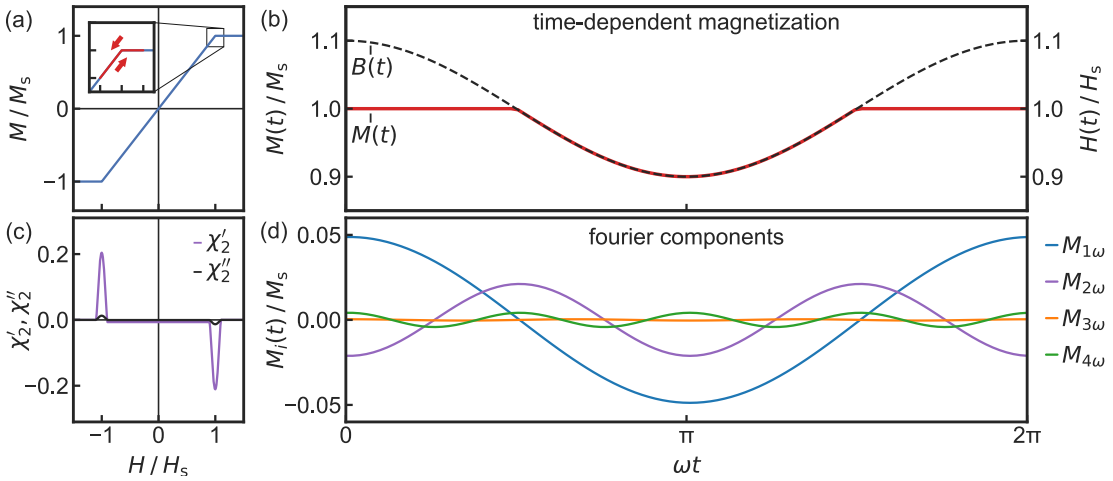

Figure 3.1: Even harmonic generation at the approach to saturation. (a) Schematic field dependence of a soft ferromagnet. (b) Time dependent magnetic response (solid red line) to an oscillating field of the form $H(t) = 0.1 \cdot H_\mathrm{s} \cos \omega t + H_\mathrm{s}$ (dashed black line). The path of the oscillating magnetization as a function of field is illustrated in the inset of (a). (c) Second harmonic susceptibility as a function of field. (d) Fourier components of the magnetic response up to fourth-order.

3.2.3 Nonlinear Harmonic Susceptibility

In general, the magnetic response of a sample to an external magnetic field

$$H(\omega, t) = H_\mathrm{dc} + H_\mathrm{ac} \cos \omega t$$

may be expressed as a Fourier expansion:

$$M(\omega, t) = M_0 + \sum_{n=1}^{\infty} \left(M'_n \cos n\omega t + M''_n \sin n\omega t \right) \tag{3.10}$$

$$= \chi_\mathrm{dc} H_\mathrm{dc} + H_\mathrm{ac} \sum_{n=1}^{\infty} \left(\chi'_n \cos n\omega t + \chi''_n \sin n\omega t \right) \tag{3.11}$$

where

$$\chi'_n = \frac{1}{\pi H_\mathrm{ac}} \int_0^{2\pi} M(\omega, t) \cos n\omega t \ \mathrm{d}\omega t, \tag{3.12}$$

and

$$\chi''_n = \frac{1}{\pi H_\mathrm{ac}} \int_0^{2\pi} M(\omega, t) \sin n\omega t \ \mathrm{d}\omega t \tag{3.13}$$

Measuring higher harmonics can provide insightful information. The emergence of a second harmonic as a function of temperature in zero field indicates a spontaneous magnetic moment and thus a ferromagnetic transition [124]. In contrast, a peak in the third harmonic as a function of temperature at zero field is a clear indicator for a magnetic transition in general (e.g. paramagnetic to spin-glass) and is not limited to ferromagnetic order [124].

Furthermore, deviations of the field dependence of the magnetization from the linear behavior inevitably lead to higher harmonics. In the following, the approach to saturation in a soft ferromagnet is used as an example to illustrate the emergence of even harmonics in the ac-susceptibility. In this example, hysteretic effects are neglected. Fig. 3.1(a) schematically shows the field dependence of the magnetization of a soft ferromagnet. The magnetization increases linearly with field until saturation M_s is reached at a critical field H_s. The application of a small sinusoidal magnetic excitation field, biased by H_s, leads to a time-dependent magnetization (see Fig. 3.1(b)), where the magnetization oscillates along the hysteresis curve around H_s illustrated in the inset of Fig. 3.1(a) in red. During the negative half cycle, the magnetization is not yet fully saturated resulting in a response proportional to the excitation field. During the positive half-cycle, however, the magnetization is saturated resulting in a constant response. The overall response, shown in Fig. 3.1(b), is therefore strongly anharmonic and consist entirely of even higher harmonics. A separation of $M(t)$ in Fourier components up to fourth order is shown in Fig. 3.1(d) for clarity. Measuring the 2nd harmonic susceptibility χ_2 as a function of field thus leads to a graph as shown in Fig. 3.1(c). χ_2 is zero over the entire field range, except for two peaks at the positive and negative saturation fields.

As an interesting fact, note that higher harmonics do not contribute to energy dissipation. The energy dissipation per cycle, W, is calculated as the area enclosed by the M-H loop

$$W = \mu_0 \oint M(\omega,t)\ \mathrm{d}H(\omega,t) \tag{3.14}$$

$$= -\mu_0 \omega H_\mathrm{ac} \oint \left[M_0 + \sum_{n=1}^{\infty} \left(M_n' \cos n\omega t + M_n'' \sin n\omega t \right) \right] \sin \omega t\ \mathrm{d}t \tag{3.15}$$

$$= -\mu_0 \pi \chi_1'' H_\mathrm{ac} \tag{3.16}$$

and depends only on the imaginary part of the first harmonic χ_1''.

3.2.4 Temperature vs. Field Protocols

In view of strong hysteretic effects associated with the magnetic properties of skyrmion phases, four different cooling protocols, illustrated in Fig. 3.2(a)–(d), were used in this work, namely

- Zero-field cooling (ZFC): (i) The sample was first cooled to the desired target temperature in zero field. (ii) Subsequently, data was recorded in a field sweep with increasing magnetic field from $H = 0$ to $H > H_{c2}$ (Fig. 3.2(a)).

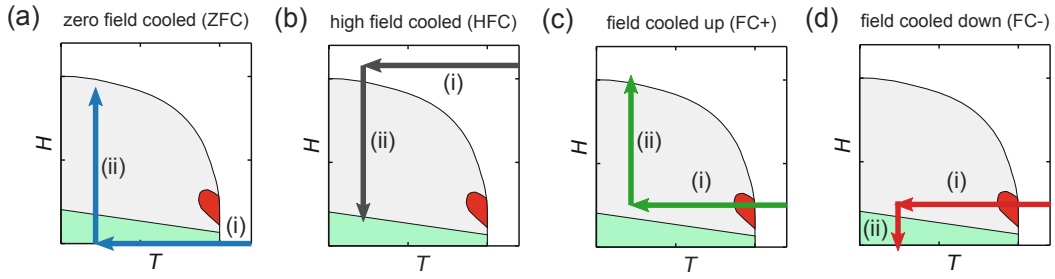

Figure 3.2: Schematics of all measurement protocols used, namely zero-field cooling (a), high-field cooling (b), and field cooling across the skyrmion lattice state with a subsequent field increase (c) or decrease (d), denoted as ZFC, HFC, FC+ and FC-, respectively.

- High-field cooling (HFC): (i) A large magnetic field was applied well above the upper critical field H_{c2} before cooling to the desired target temperature. (ii) Subsequently, data was recorded in a field sweep under decreasing field from $H > H_{c2}$ to $H < -H_{c2}$ (Fig. 3.2(b)). Note that due to symmetry, we do not distinguish between initial high field cooling in positive fields or negative fields. In addition, we have carefully checked that the behavior following HFC is equivalent to the behavior recorded under decreasing field from well above H_{c2} after initial ZFC. This applies to both $Fe_{0.5}Co_{0.5}Si$ and Cu_2OSeO_3. Therefore we refer to both as HFC.

- Field cooling (FC): (i) The sample was cooled to the target temperature across the skyrmion lattice state in an applied magnetic field of $B = 10\,\mathrm{mT}$. Typical cooling rates were of the order $\approx 5\,\mathrm{K\,min^{-1}}$ if not otherwise stated. (ii) Data was then recorded with increasing (Fig. 3.2(c)) or decreasing field (Fig. 3.2(d)), denoted as FC+ or FC-, respectively.

Additionally, we have employed first-order reversal curve type measurements in the investigation of the low-temperature skyrmion phase in Cu_2OSeO_3. First order reversal curves (FORC) are typically used to investigate the irreversible behavior of ferromagnetic systems [125–127] and denote a special type of minor hysteresis loop. Fig. 3.3 schematically explains the FORC measurement at the example of a hard ferromagnet. A single FORC measurement is recorded in a two stage process and may described as follows:

(i) Starting in the saturated state, the field is reduced to a reversal field denoted as B_{rev}.

(ii) Subsequently, data is taken while increasing the field until the saturated state is recovered.

The magnetization is thus a function of two variables, the reversal field B_{r} and the applied field B. This process is then repeated for various reversal fields. Disparities between FORC curves are then directly related to irreversible processes. In this context it should

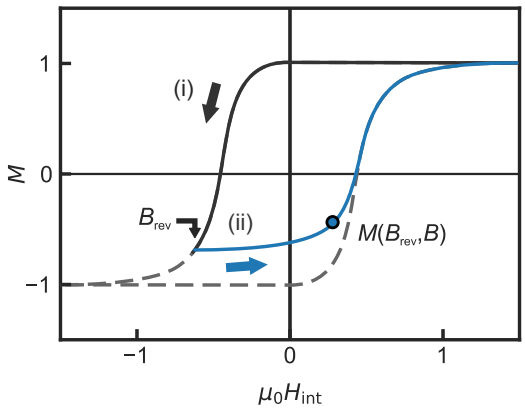

Figure 3.3: Schematic illustrating the first-order reversal curve (FORC) protocol. (i) From the saturated state, the field is reduced to a reversal field, B_{rev}. (ii) Data is taken while increasing the field again towards the saturated state.

be noted that unlike classical FORC analysis, we do not calculate a FORC distribution from the measured magnetization curves.

3.2.5 Specific Heat Calorimetry

The most common method to determine the specific heat of a sample is the heat pulse method. Here, a heating pulse is applied to a sample, weakly linked to a thermal bath, and the resulting temperature response of the sample is measured. A block diagram is shown in Fig. 3.4(a).

The temperature response is governed by a first order differential equation:

$$C\frac{\mathrm{d}T(t)}{\mathrm{d}t} = -K_{\mathrm{p}}(T(t) - T_{\mathrm{bath}}) + P(t). \tag{3.17}$$

Here, $C = C_{\mathrm{s}} + C_{\mathrm{p}}$ is the combined heat capacity of the sample C_{s} and the platform C_{p} and K_{p} is the heat conductance of the thermal link between platform and thermal bath. The coupling between sample and platform is assumed to be perfect, yielding $K_{\mathrm{s}} = \infty$. Moreover, the temperature of the platform, T, is thus equal to the temperature of the sample. The temperature of the bath is denoted as T_{b}.

Solving this differential equation for a step-like heat pulse $P(t) = P_0 \cdot \theta(t)$ applied to the platform leads to a temperature response of the form

$$T(t) = \frac{P_0}{K}\left[1 - e^{-\frac{K}{C}t}\right] \tag{3.18}$$

which in turn may be fitted to the measured temperature response to obtain C. This equation is equivalent to the loading curve of a capacitor exposed to a constant voltage, hence the name heat capacitance. For better convergence, it is helpful to fit the cooling curve as well, where the heater is switched off again. To determine the heat capacity of

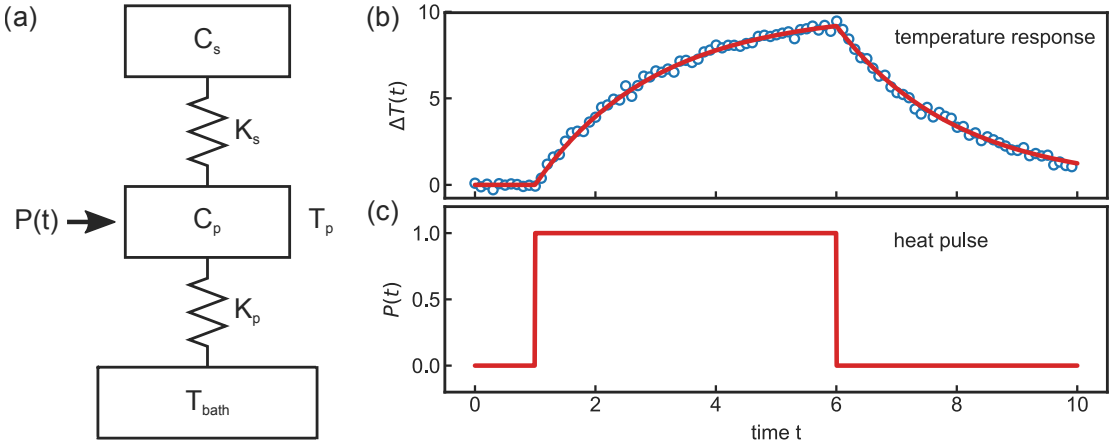

Figure 3.4: (a) Block diagram of the specific heat setup. A sample with a specific heat C_s is coupled via a heat link K_s to a platform with a specific heat C_p. The coupling between sample and platform is assumed to be perfect, giving $K_s = \infty$. The platform is weakly coupled to thermal bath T_{bath} via the heat link K_p. A heat pulse $P(t)$ is applied to the platform and the temperature response of the platform T_p is measured. (b) Simulated temperature response (blue symbols) and fit (red line) to the heat pulse shown in (c).

the sample the heat capacity of the platform has to be subtracted, which is measured in a heat pulse experiment without a sample. A typical temperature response and the fitted single-τ model are illustrated in Fig. 3.4(b), the corresponding heat pulse is shown in Fig. 3.4(c). Note that the temperature rise has to be small for the assumption of a constant specific heat during the heat pulse.

3.3 Experimental Apparatus

3.3.1 Quantum Design PPMS

The Quantum Design Physical Property Measurement System (PPMS) is a static flow cryostat equipped with various measurement options. The available temperature range is 1.8 K to 400 K. During this thesis two PPMS cryostats one with a 9 T the other with a 14 T superconducting magnet were used. Both superconducting magnets can be operated in persistent mode, allowing for extremely stable magnetic fields.

3.3.2 Magnetization and AC Susceptibility Measurements in the PPMS

The ACMS-option enables the PPMS to measure the ac-susceptibility as well as the dc-magnetization with the same hardware. It consists of a coil inset, a servo motor and measurement electronics. The coil inset consists of a compensated ac-excitation coil and a set of detection coils. Two single-turn low inductance calibration coils allow for the

direct measurement of the instrumental phase shift for each data point, increasing the precision of the susceptibility measurements.

The dc magnetization was measured by means of an extraction method with a sensitivity range from 2.5×10^{-5} emu up to 5 emu utilizing the servo motor to move the sample through the detection coils. The ac-susceptibility works by applying a small sinusoidal magnetic excitation field and measuring the response of the sample. By means of a correlation method, the real and imaginary part of the magnetic response, denoted as χ' and χ'', as well as higher harmonics up to the 10th order may be determined simultaneously. The available frequencies and field strengths range from 10 Hz to 10 kHz and 0.17 µT to 1.7 µT respectively.

The sample was mounted with GE-varnish and Teflon tape onto a Delrin sample holder at the end of a sample rod. If not otherwise stated an excitation frequency of $f = 911$ Hz and an excitation amplitude of $B_{\mathrm{ac}} = 0.1$ mT was used for the measurements.

3.3.3 Specific Heat Measurements in the PPMS

The HC-option provides the capability to measure the specific heat of a sample. The sample is mounted on a $3 \times 3\,\mathrm{mm}^2$ Al2O3 platform using Apiezon-N grease. The platform is equipped with a resistive heater and a thermometer and is itself weakly coupled to the thermal bath by thin platinum wires. By applying a small step like heat pulse and recording the temperature response of the platform the specific heat may be determined. The heat capacity is extracted automatically by fitting the temperature response curve. Two models are available. The simple but fast single-τ model assumes perfect coupling between sample and platform. The advanced two-τ model models the finite thermal coupling between platform and sample. The model resulting in the best fit is chosen automatically.

3.4 Data Analysis

This section summarizes the analyses methods uses in this dissertation, namely master-curve scaling and the extraction of magnetocrystalline anisotropies based on magnetic work and critical fields.

3.4.1 Master Curve Scaling

The time-temperature superposition principle is a widely used concept in the field of glass forming liquids and polymers and has also been successfully applied to superconductors, spin-glasses and ferromagnets [128–133]. The basic concept behind time-temperature superposition is that a change in temperature has the same effect as the advancement of time by a specific amount. To be more precise, let $G(t, T)$ be a physical parameter such as viscosity that depends on both time and temperature, then the time-temperature superposition principle states that

$$G(t, T) = G(t/t_0, T_0), \tag{3.19}$$

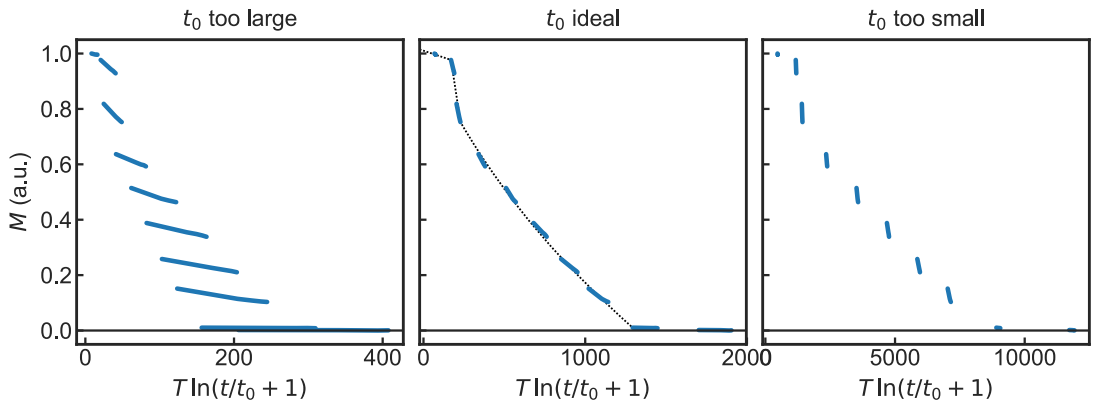

Figure 3.5: Illustration of master curve scaling with the scaling factor t_0 underemphasizing time (a), properly chosen (b) and overemphasizing time (c). Blue shaded line segments show typical relaxation data as a function of $T\ln(t/t_0+1)$. Dashed black line in (b) acts as a guide to the eye.

Here, t_0 acts as a shift factor rescaling the time axis. If the shift factor t_0 is known, the prediction of long time behavior, at temperatures where measurements would require experimentally inaccessible timescales, from measurements at different temperatures on accessible timescales is possible. The combination of several measurements at various temperatures to a single, smooth curve at a reference temperature is known as the master curve scaling. Note that in general t_0 is not a constant, but may also be temperature-dependent.

As shown in Sec. 1.2, the magnetic viscosity originates from a broad distribution of activation energies which are triggered by a relaxation front, $E = k_\mathrm{B}T\ln(t/t_0+1)$, advancing linear in temperature but logarithmically in time. This allows us to construct a master curve from relaxation data by determining the constant shift factor t_0. In Sec. 4.2, this concept will be applied to magnetic relaxation data of a metastable skyrmion lattice.

The construction is carried out according to the following protocol:

1. For each relaxation measurement subtract the magnetization value following zero-field cooling at the corresponding temperature. This is necessary because the finite remanence of the superconducting magnet leads to a non-vanishing magnetization of the helical groundstate.

2. Correct for the temperature dependence of the magnetic moment by dividing through the normalized saturation magnetization $M_s(T)/M_s(T=0)$. The saturation magnetization is extracted from a temperature sweep at $B = 9\,\mathrm{T}$, deep in the field polarized state. This correction improves the results as the temperature dependence breaks the time-temperature superposition principle. Note that this is not a large correction, as the saturation magnetization reduces by approximately 10 % from 2 K to 30 K.

3. Plot as a function of $T\ln(t/t_0+1)$ and vary the shift factor t_0 until all relaxation measurements align to form a single, smooth curve.

The effects of the shift factor are illustrated in Fig. 3.5. A properly chosen shift factor is illustrated in Fig. 3.5(b). A shift factor underemphasizing and overemphasizing time is shown in Fig. 3.5(a) and Fig. 3.5(c), respectively.

3.4.2 Extraction of Cubic Anisotropy Constant from Magnetic Work

By determining the magnetic work required to drive the system into saturation from magnetization curves, we are able to determine the anisotropy constants. The magnetic work is defined as

$$W = \int B \, \mathrm{d}M \tag{3.20}$$

and corresponds to the area between the ordinate and the magnetization curve in a $M(B)$ diagram illustrated in Fig, 3.6. The difference of magnetic work between different orientations directly corresponds to the difference in anisotropy energy between them. By measuring the magnetization curves of a cubic crystal in the three main axes, the anisotropy constants K_1 and K_2 can be determined as follows: The anisotropy energy for the three main axes is given by

$$F_{100} = K_0, \tag{3.21}$$

$$F_{110} = K_0 + \frac{K_1}{4}, \tag{3.22}$$

$$F_{111} = K_0 + \frac{K_1}{3} + \frac{K_2}{27} \tag{3.23}$$

with

$$\hat{\mathbf{M}}_{100} = \begin{pmatrix} 1 & 0 & 0 \end{pmatrix}, \tag{3.24}$$

$$\hat{\mathbf{M}}_{110} = \frac{1}{\sqrt{2}} \begin{pmatrix} 1 & 1 & 0 \end{pmatrix}, \tag{3.25}$$

$$\hat{\mathbf{M}}_{111} = \frac{1}{\sqrt{3}} \begin{pmatrix} 1 & 1 & 1 \end{pmatrix}. \tag{3.26}$$

By equating the energies with the work in the corresponding directions and solving the resulting system of equations one obtains:

$$K_0 = W_{100}, \tag{3.27}$$

$$K_1 = 4(W_{110} - W_{100}), \tag{3.28}$$

$$K_2 = 27(W_{111} - W_{100}) - 36(W_{110} - W_{100}). \tag{3.29}$$

Care has to be taken to avoid common pitfalls. In addition to magnetocrystalline anisotropy, other effects can also lead to magnetic anisotropy with shape and magnetoelastic anisotropy being the most important ones.

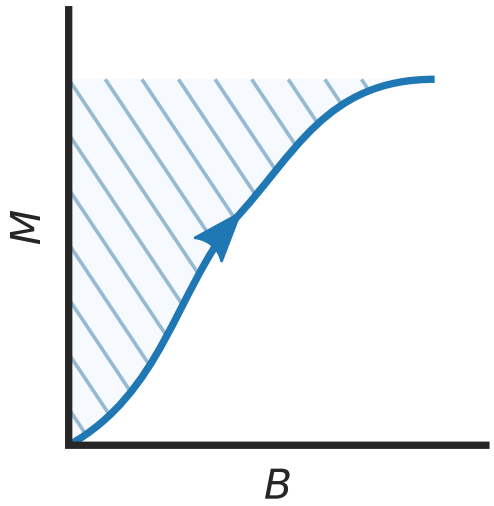

Figure 3.6: Magnetization as a function of field. Shaded area between ordinate and magnetization curve corresponds to work done in magnetization.

Magnetoleastic anisotropy can be largely avoided by not straining the specimen. It is however not possible to avoid shape anisotropy. Instead, the influence of shape anisotropy must be eliminated by appropriate geometries and careful demagnetization correction.

Furthermore, the accuracy depends on the precise measurement of the magnetization. During this work it has been shown that the magnetization value measured in the PPMS reacts sensitively to the centering of the sample. Thermal expansion of the cryostat after a change of temperature will lead to an off-centering of the sample and in turn to an error in the magnetization measurement.This may be avoided by recentering the sample after each change in temperature.

3.4.3 Extraction of Cubic Anisotropy Constant from Critical Fields

The effects of magnetocrystalline anisotropy on the critical fields of cubic chiral magnets has been investigated by Grigoriev and coworkers[88] based on the Bak-Jennsen model for chiral magnets[36]. The relations for the critical fields inferred in this work, will in-turn allow us to determine the magnetic anisotropy constant.

The analysis, following Grigoriev and coworkers, may be summarized as follows [88]:

Starting from a standard Bak-Jensen model,

$$\begin{aligned}\mathcal{H} = \int \mathrm{d}^3 r \Bigg[& \underbrace{\frac{J}{2a}(\nabla \mathbf{M})^2}_{\text{Exchange}} + \underbrace{\frac{D}{a^2}\mathbf{M}\cdot(\nabla\times\mathbf{M})}_{\text{Dzyaloshinskii-Moriya}} \\ & \underbrace{-\frac{1}{a^3}\mathbf{M}\cdot\mathbf{B}}_{\text{Zeeman}} + \underbrace{\frac{K}{a^3}(M_x^4+M_y^4+M_z^4)}_{\text{cubic anisotropy}} \\ & \underbrace{-\frac{J_{ea}}{2a}\left[(\nabla_x M_x)^2+(\nabla_y M_y)^2+(\nabla_z M_z)^2\right]}_{\text{Exchange Anisotropy}}\Bigg].\end{aligned} \tag{3.30}$$

including exchange interaction, Dzyaloshinskii-Moriya interaction, Zeeman interaction and cubic anisotropies, the energy of a conical helix solution

$$M(\mathbf{r}) = M_\mathrm{s}\left[\hat{\mathbf{c}}\sin\alpha + \left(\mathbf{A}e^{i\mathbf{k}\cdot\mathbf{r}} + \mathbf{A}^* e^{-i\mathbf{k}\cdot\mathbf{r}}\right)\cos\alpha\right] \tag{3.31}$$

may be minimized with respect to the propagation vector, $\mathbf{k}$, and the opening angle, α. The first term represents the ferromagnetic component of the helix, the second term represents the spiraling component perpendicular to the propagation direction. The amplitude vector $\mathbf{A}$ is defined as $\mathbf{A} = (\hat{\mathbf{a}} - i\hat{\mathbf{b}})/2$, with the unit vectors $\hat{\mathbf{a}}$, $\hat{\mathbf{b}}$ and $\hat{\mathbf{c}}$ forming a right handed orthogonal frame.

Assuming a helical propagation aligned along the field direction, corresponding to the conical state, yields

$$M_\mathrm{s}H = \frac{7}{4}KW(\theta_\mathrm{H},\phi_\mathrm{H})\sin^3\alpha + \left[MAk^2 - \frac{3}{4}KW(\theta_\mathrm{H},\phi_\mathrm{H})\right]\sin\alpha, \tag{3.32}$$

where θ_H and ϕ_H represent the orientation of the magnetic field, H, in spherical coordinates and A is the spinwave-stiffness. The cubic invariant $W(\theta_\mathrm{H},\phi_\mathrm{H})$ is defined as

$$W(\theta_\mathrm{H},\phi_\mathrm{H}) = 10C - 6 = \begin{cases} 4 & \langle 100\rangle \\ -1 & \langle 110\rangle \\ -8/3 & \langle 111\rangle \end{cases} \tag{3.33}$$

with $C = \sum_j c_j^4$. If $K\cdot W \geq 0$, Eq. 3.32 has a solution for $\sin\alpha = 0$ at

$$M_\mathrm{s}H_{\mathrm{c}2} = Ak^2 + W(\theta_\mathrm{H},\phi_\mathrm{H})\cdot K \tag{3.34}$$

In contrast, if $K\cdot W \leq 0$ the solution depends on the ratio of the Dzyaloshinskii-Moriya interation and the cubic anisotropy. For $M_\mathrm{s}Ak^2 \geq \frac{18}{4}|K\cdot W|$, Eq. 3.32 has a solution for $\sin\alpha = 0$ at

$$M_\mathrm{s}H_{\mathrm{c}2} = Ak^2 - |W(\theta_\mathrm{H},\phi_\mathrm{H})\cdot K| \tag{3.35}$$

In contrast, for $K \cdot W \leq 0$ and $M_s A k^2 \leq \frac{18}{4}|K \cdot W|$ the conical helix solution becomes unstable at a finite opening angle

$$\alpha_{c2} = \sqrt{\frac{4}{21}\frac{M_s A k^2}{|K \cdot W|} + \frac{1}{7}} \tag{3.36}$$

with the corresponding critical field

$$H_{c2} = \sin \alpha_{c2} \left(\frac{2}{3} A k^2 + \frac{1}{2}\frac{|K \cdot W|}{M_s} \right) \tag{3.37}$$

Based on these relations, the anisotropy constant, K, may be inferred from measurements of H_{c2} in two orientations. Assuming measurements of H_{c2} of the $\langle 111 \rangle$ and $\langle 110 \rangle$ orientations and a negative K constant, Eq. 3.34 yields

$$K = Ms \frac{H_{c2}^{111} - H_{c2}^{110}}{W^{111} - W^{110}} = -\frac{3}{5} M_s \left(H_{c2}^{111} - H_{c2}^{110} \right). \tag{3.38}$$

By measuring H_{c2} along $\langle 111 \rangle$ and $\langle 110 \rangle$ we are thus able to infer the cubic anisotropy constant, K, as a function of temperature.

CHAPTER 4

Nonequilibrium Properties of the Skyrmion Lattice in $Fe_{0.5}Co_{0.5}Si$

In this section we report a comprehensive study of the magnetic properties of $Fe_{0.5}Co_{0.5}Si$ focusing on the non-equilibrium skyrmion lattice state. Using magnetization and ac-susceptibility, we investigate the stability and the underlying energetics of the metastable skyrmion lattice as a function of time, temperature, and field.

This chapter is structured in five Sections. In Section 4.1, we present the results of the extensive magnetization and susceptibility measurements, starting with a brief introduction of the key features, followed by a detailed presentation of the magnetization and susceptibility measurements. As a first main result, we report the cooling history dependence of the magnetic phase diagram. In Section 4.2, we address the irreversibilities and relaxation effects associated with the nonequilibrium skyrmion lattice. First, we present typical magnetic relaxation data, recorded in zero-field, followed by an analysis of the relaxation data based on a magnetic viscosity model. Next, we address irreversibilities in the temperature dependence of the magnetic remanence. Finally, we infer the distribution of activation energies using master curve scaling. The discussion of the results is addressed in Section 4.3 and comprised of two parts. First, based on results of the relaxation measurements, we demonstrate that the skyrmion lattice in zero-field is stabilized beyond the topological protection. Secondly, we address the magnetic field dependence of the metastable skyrmion lattice. In Section 4.4, we provide a comparison of nonequilibrium skyrmion lattices in various chiral magnets. We end this chapter with a summary in Section 4.5.

4.1 Magnetization and AC Susceptibility

The presentation of the magnetization and susceptibility data is organized as follows: First, in Sec. 4.1.1, we introduce the key features of the magnetization and susceptibility data. Next, we address the results of the field dependent magnetization measurements for

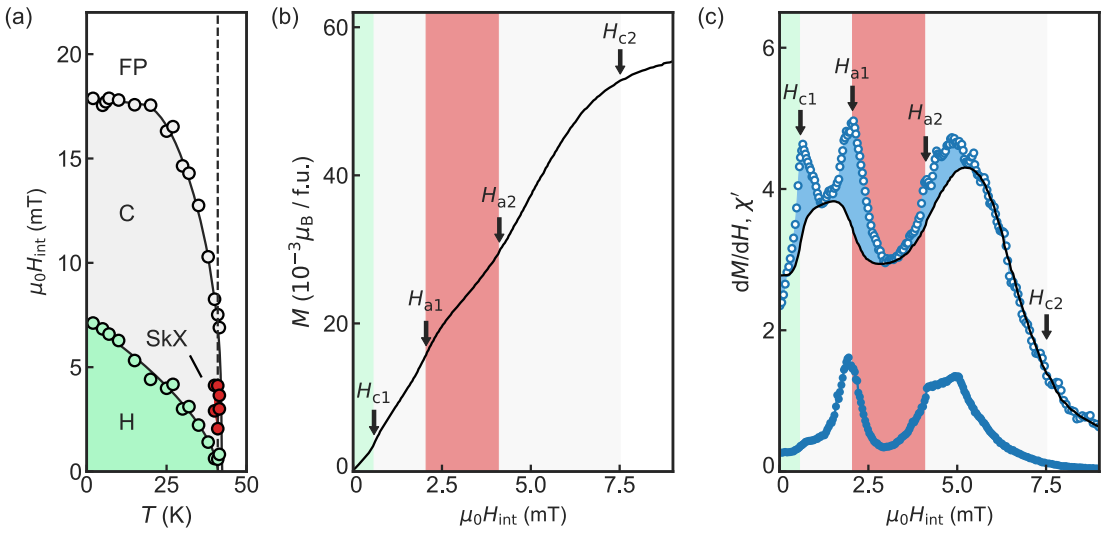

Figure 4.1: Key features of the field dependent magnetization and susceptibility data in $Fe_{0.5}Co_{0.5}Si$. (a) Magnetic phase diagram constructed from isothermal magnetization and susceptibility measurements following zero-field cooling. We distinguish the helical (H, green), conical (C, grey), skyrmion lattice (SKX, red) and field polarized (FP, white) state. Magnetization (b) and susceptibilities (c) as a function of field following ZFC at $T = 41\,\mathrm{K}$. With increasing field, the system transitions, in this order, through helical (green), conical (grey), skyrmion lattice (red), conical (grey) and field polarized state (white), indicated as colored shading of the background.

various temperatures and cooling histories in Sec. 4.1.2. We proceed with an an in-depth presentation of the differential and ac-susceptibility data in Sec. 4.1.3. Finally, we present the history dependent magnetic phase diagrams, inferred from the extensive dataset.

4.1.1 Key Characteristics of the Magnetization and AC Susceptibility

The magnetic phase diagram of $Fe_{0.5}Co_{0.5}Si$ inferred from isothermal magnetization and susceptibility measurements after zero-field cooling is shown in Fig. 4.1(a). It resembles the generic phase diagram as discussed in Sec. 2.1 featuring the helimagnetic ground state (green), the conical state (grey) at intermediate fields and the field polarized state (white) at large fields and low temperatures. The skyrmion lattice state (red) is seen as a small phase pocket at finite fields just below the ordering temperature.

The magnetization and susceptibility as a function of field at $T = 41\,\mathrm{K}$ following ZFC is shown in Fig.4.1(b) and Fig. 4.1(c), respectively. At this temperature the system passes through all magnetic phases, marked by a dashed line in Fig. 4.1(a), thus allowing to address all signatures of the individual phases. With increasing field, the system displays transitions, in this order, between helical (green), conical (grey), skyrmion lattice (red),

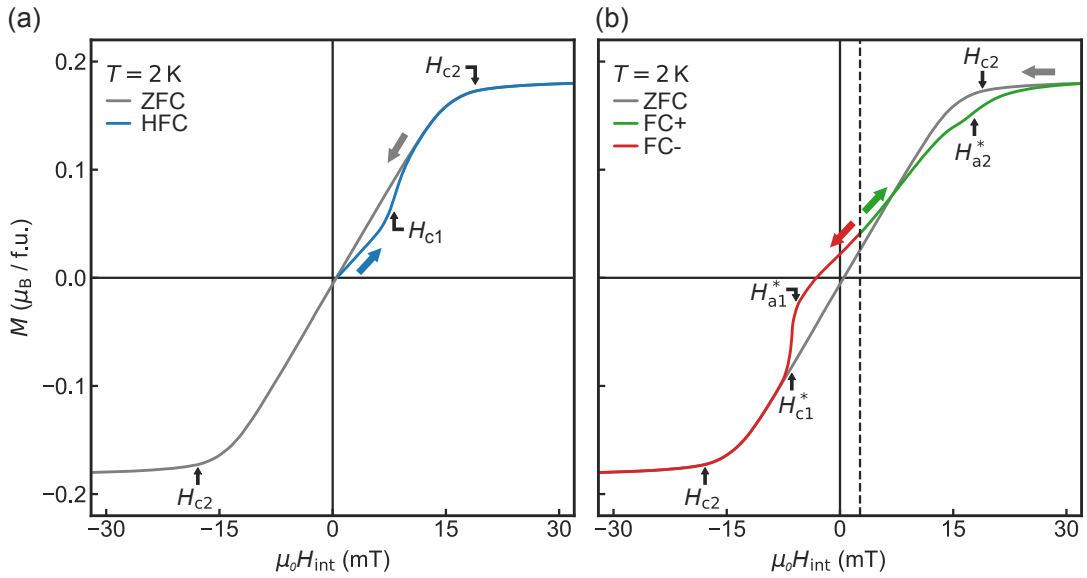

Figure 4.2: Typical magnetization data as a function of internal field recorded at $T = 2\,\mathrm{K}$ following (a) ZFC (blue) and HFC (grey) as well as (b) FC+ (green), FC- (red) and HFC (grey).

conical (grey) and field polarized state (white). The magnetization, shown in Fig. 4.1(b), exhibits a nearly linear field dependence until saturation is reached. A slight decrease of the incline at intermediate fields signals the skyrmion phase. Such small deviations from the linear behavior, however, are best seen in the differential susceptibility, $\mathrm{d}M/\mathrm{d}H$ calculated from the magnetization, as shown in Fig. 4.1(c) (symbols).

As a function of increasing field, three distinct peaks are visible, denoted as H_{c1}, H_{a1} and H_{a2}, respectively. H_{c1} signals the helical to conical transition, whereas H_{a1} and H_{a2} correspond to the conical to skyrmion lattice and skyrmion lattice to conical transitions, respectively. Note that both the helical and the skyrmion lattice state display a reduced susceptibility as compared to the conical state. The transition into the field polarized state is accompanied by a rapid decrease of the susceptibility towards zero, with the critical field H_{c2} defined as the point of inflection. The real part of the ac-susceptibility, χ', is also shown in Fig. 4.1(c) (black line). With the exception of the transition regimes surrounding H_{c1}, H_{a1} and H_{a2}, quantitative agreement between $\mathrm{d}M/\mathrm{d}H$ and χ' is observed. The imaginary part of the ac-susceptibility, χ'', corresponding to the magnetic dissipation, is shown in Fig. 4.1(c) as a blue line. Two large and broad peaks may be seen at H_{a1} and H_{a2} correlating with deviations between $\mathrm{d}M/\mathrm{d}H$ and χ'. These signatures indicate slow relaxation processes and have been studied in detail in $Fe_{1-x}Co_xSi$ and other related compounds [134–137].

Four different cooling protocols were used to investigate the metastable properties of $Fe_{0.5}Co_{0.5}Si$, namely zero-field cooling (ZFC), high-field cooling (HFC), and field cooling (FC±). Specific details of the protocols may be found in Sec. 3.2.4. Typical

isothermal magnetization data recorded at $T = 2\,\mathrm{K}$, following each protocol, are shown in Fig. 4.2(a), (b). The data is shown as a function of internal field, corrected for demagnetizing effects. Colored symbols mark the critical fields, defined from susceptibility data, as shown in Sec. 4.1.3. Following zero field cooling (blue), characteristic signatures of the helical, conical and field polarized state are observed, consistent with literature [135]. At low temperatures, the signatures are much more pronounced compared to $T = 41\,\mathrm{K}$ shown above. Initially, a slow but steady increase of M is observed. When the critical field H_{c1} is reached a reorientation of the helices towards the field direction takes place, the so-called helical-to-conical transition, evident as a steep increase of the magnetization around H_{c1}. With a further increase in field, the magnetization increases linearly until the upper critical field H_{c2} is reached, at which the system enters the field polarized state.

Following high-field cooling (grey), the conical phase is observed over the complete field range $-H_{c2} < H < H_{c2}$ as the helical state at low fields is not recovered. The inability to recover the helical state once the conical state has been reached has been observed before in $Fe_{1-x}Co_xSi$ [90, 135] and might be attributed to strong pinning effects, expected in such a highly doped system where random site disorder is prevalent [138].

Significantly more complex behavior is obtained when the system is cooled in an applied field (FC+, FC-) crossing through the skyrmion lattice phase, here $B = 10\,\mathrm{mT}$. In doing so, the skyrmion lattice is stabilized down to lowest temperatures as a metastable state [46, 90, 95, 135, 139]. Typical magnetization data following FC+ and FC- recorded at $T = 2\,\mathrm{K}$ are shown in Fig. 4.2(f).

Following initial cooldown, an elevated magnetization relative to the ZFC and HFC values is visible. This is consistent with the signatures of a stable skyrmion lattice phase at higher temperatures, albeit much more pronounced. The magnetization curves resulting from a successive increase (FC+, green) or decrease (FC-, red) of the magnetic field deviate from both the ZFC and HFC curves in a broad field range. As the field increases (FC+, green), the magnetization increases almost linearly albeit with a slower rate compared to the HFC data and as a result intersects the HFC curve. Furthermore, the magnetic field necessary to saturate the magnetization is significantly larger compared to the ZFC and HFC curves, indicating the survival of the skyrmion lattice into the field polarized field region up to H_{a2}^{+}. With a reduction in field the magnetization decreases linearly, resulting in a finite remanence, M_R, as well as a finite coercive field H_C. This indicates survival of skyrmions in negative fields as both helical and conical state have vanishing remanence and coercitivity. At the field value of the helical to conical transition at negative fields, $-H_{c1}^{*}$, the excess magnetization rapidly collapses down to the conical value, suggesting complete destruction of the metastable skyrmion state.

4.1.2 Temperature Evolution of the Magnetization

Having defined the key characteristics in magnetization of the metastable skyrmion lattice, we will now discuss the evolution of these features as a function of temperature.

A summary of the cooling history dependent isothermal magnetization measurements at various temperatures is presented in Fig. 4.3(a). The magnetization data is shown

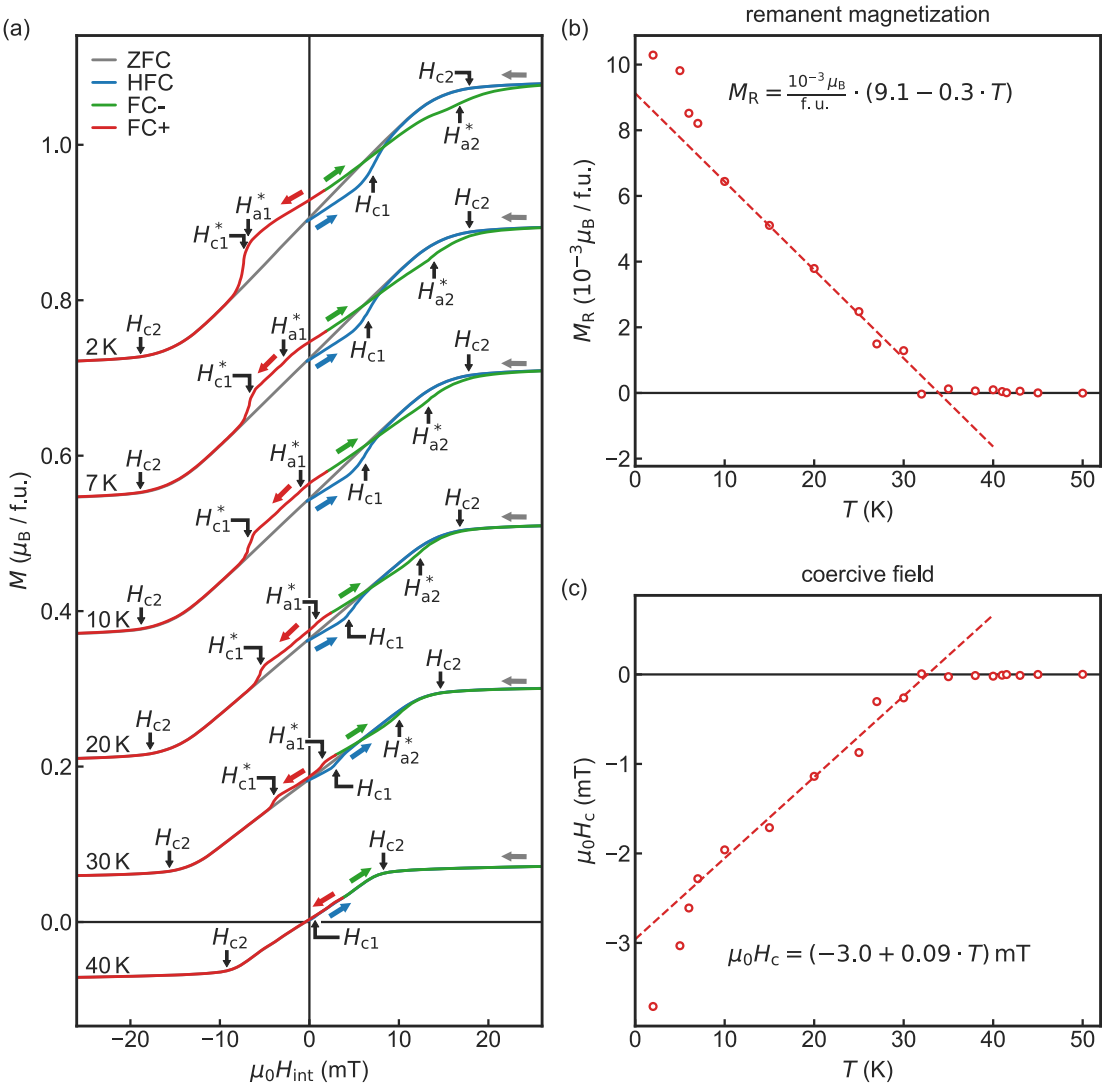

Figure 4.3: (a) Isothermal magnetization measurements at various temperatures following HFC (grey), ZFC (blue), FC+(green) and FC- (red). Data is shown as a function of internal field, shifted vertically for clarity. Colored symbols mark the critical fields. (b),(c) Remanent magnetization M_R and coercitivity field H_C inferred from the FC- data as a function of temperature.

as a function of internal field, corrected for demagnetizing effects. For clarity, the data is shifted vertically. The FC+/FC- data has been recorded following field cooling in an applied field of $B = 10\,\mathrm{mT}$. Note that due to demagnetizing effects, the corresponding internal field varies with temperature.

Both the ZFC and HFC data show qualitatively identical behavior at all temperatures. With increasing temperature, a reduction of the relevant field scales is observed. After field cooling (FC+, green; FC-, red) a significant deviation from both the ZFC (blue) and HFC (grey) curves may be seen, originating from the metastable skyrmion lattice state. At the lowest temperatures, the metastable state is observed in an exceptionally wide field range, extending into the field polarized state at positive fields up to H_{a2}^{+} as well as deep into the negative field region down to H_{c1}^{*}. This is reflected in a considerably larger field necessary to saturate the system at positive fields (FC+, green) compared to the ZFC and HFC curves. With increasing temperature, the field region of the metastable state narrows down significantly. At 40 K, no visual difference is observed between the different cooling histories.

The remanent magnetization at $B = 0$ obtained after field cooling (FC-) is shown in Fig. 4.3(b) as a function of temperature. The presence of a remanent moment shows that a skyrmion carries a finite magnetic moment in zero field. In contrast, the helimagnetic and conical state have no net magnetization in zero field. The remanent magnetization exhibits a linear temperature dependence in a broad temperature range with

$$M_{\mathrm{R}} = 9.1 \times 10^{-3} \frac{\mu_{\mathrm{B}}}{\mathrm{f.u.}} - T \cdot 0.3 \times 10^{-3} \frac{\mu_{\mathrm{B}}}{\mathrm{f.u.} \cdot \mathrm{K}} \tag{4.1}$$

but vanishes above $T \approx 35\,\mathrm{K}$. Below $T \approx 7\,\mathrm{K}$, an enhanced remanence is observed, approximately $\Delta m = 2 \times 10^{-3}\,\mu_{\mathrm{B}}/\mathrm{f.u.}$ larger as expected from the linear dependence at intermediate temperatures.

Similar behavior is observed in the coercive field H_{C}, as shown in Fig. 4.3(c). Below $T \approx 35\,\mathrm{K}$, a coercive field emerges, that is linear in temperature in a broad temperature region. The temperature dependence of H_{C} is given by

$$H_{\mathrm{C}} = 0.09\,\mathrm{mT\,K^{-1}} \cdot T - 3\,\mathrm{mT} \tag{4.2}$$

Below $T \approx 7\,\mathrm{K}$, an enhanced coercive field is observed, approximately $1 \times 10^{-3}\,\mathrm{mT}$ above the extrapolated value.

The cooling rate proves to be a critical parameter in the formation of the metastable skyrmion state. It needs to be large enough to avoid crystallization of the conical ground state. To study the cooling rate dependence in $Fe_{0.5}Co_{0.5}Si$, the sample was field-cooled across the skyrmion lattice phase with various cooling rates down to $T = 2\,\mathrm{K}$. Subsequently, the magnetization was measured as a function of increasing temperature in a constant field of $B = 10\,\mathrm{mT}$. The results are summarized in Fig. 4.4(a), showing the respective magnetization curves for three different cooling rates, namely $1\,\mathrm{K\,min^{-1}}$(purple), $10\,\mathrm{K\,min^{-1}}$(green) and $20\,\mathrm{K\,min^{-1}}$(red). For comparison, blue symbols show the magnetization following initial zero-field cooling. Comparing zero-field and field cooled data at low temperatures, it is evident that the magnetization following field cooling is always larger than the magnetization following zero-field cooling. The differences between ZFC

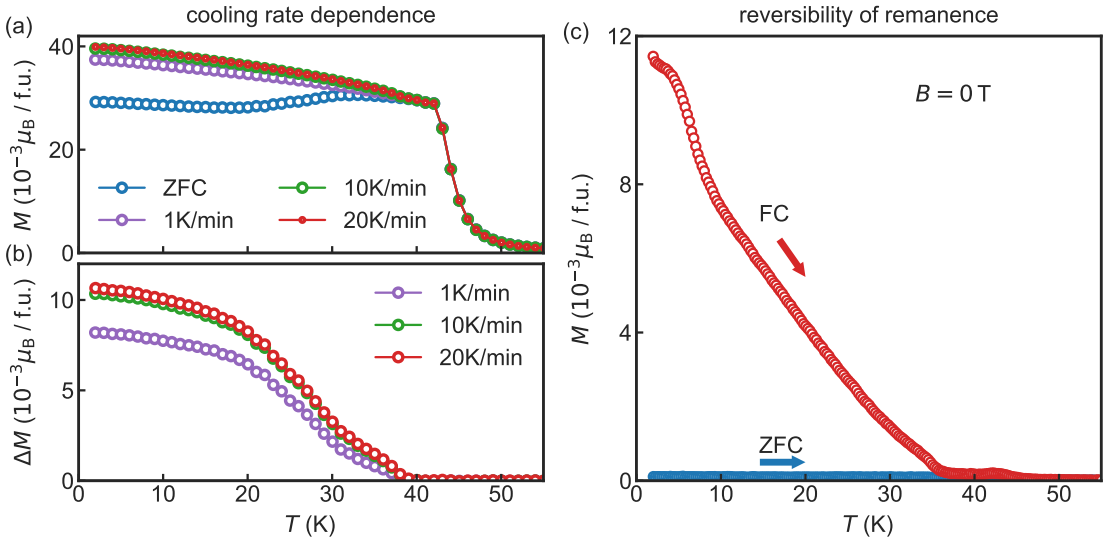

Figure 4.4: Cooling rate dependence and remanence of the metastable skyrmion lattice state. (a) Magnetization as a function of temperature at $B = 10\,\mathrm{mT}$ following FC to $T = 2\,\mathrm{K}$ with various cooling rates ($1\,\mathrm{K\,min^{-1}}$(green), $10\,\mathrm{K\,min^{-1}}$(red), $20\,\mathrm{K\,min^{-1}}$(purple)). Data was recorded while heating. For comparison, blue line shows zero-field-cooled / field-heated data at $B = 10\,\mathrm{mT}$. (b) Difference between field cooled magnetization and zero-field cooled magnetization of panel (a). (c) Magnetization as a function of temperature at $B = 0$. Data was recorded while heating with a sweep rate of $0.25\,\mathrm{K\,min^{-1}}$. Remanent magnetization following FC with a cooling rate of $20\,\mathrm{K\,min^{-1}}$ is shown in red. For comparison, magnetization data following ZFC is shown in blue.

and FC data as a function of temperature are illustrated in Fig. 4.4(b), showing the difference in magnetization $\Delta M = M_{\mathrm{hfc}} - M_{\mathrm{zfc}}$ as a function of temperature. With increasing temperature ΔM decreases and above $T \approx 40\,\mathrm{K}$ differences between all curves are negligible. Comparing the field-cooled data, an increase in magnetization is observed with increasing cooling rate. A sizable increase is seen with a cooling rate of $10\,\mathrm{K\,min^{-1}}$ compared to $1\,\mathrm{K\,min^{-1}}$. A further increase in the cooling rate to $20\,\mathrm{K\,min^{-1}}$ however only leads to a small increase in magnetization. This suggests that most of the sample volume remains in the skyrmion lattice state at cooling rates above $10\,\mathrm{K\,min^{-1}}$. These results are consistent with SANS measurements, which also showed a cooling rate dependence [139].

Fig. 4.4(c) presents the remanent magnetization measured in a temperature sweep following field cooling. After initial field cooling at $B = 10\,\mathrm{mT}$ with a cooling rate of $20\,\mathrm{K\,min^{-1}}$, the magnetization was measured in a temperature sweep from $2\,\mathrm{K}$ to $55\,\mathrm{K}$ in zero field with a heating rate of $0.25\,\mathrm{K\,min^{-1}}$. The resulting magnetization curve resembles the remanent magnetization measured in field sweeps, with an almost linear temperature dependence in a broad temperature range and a step-like increase of the

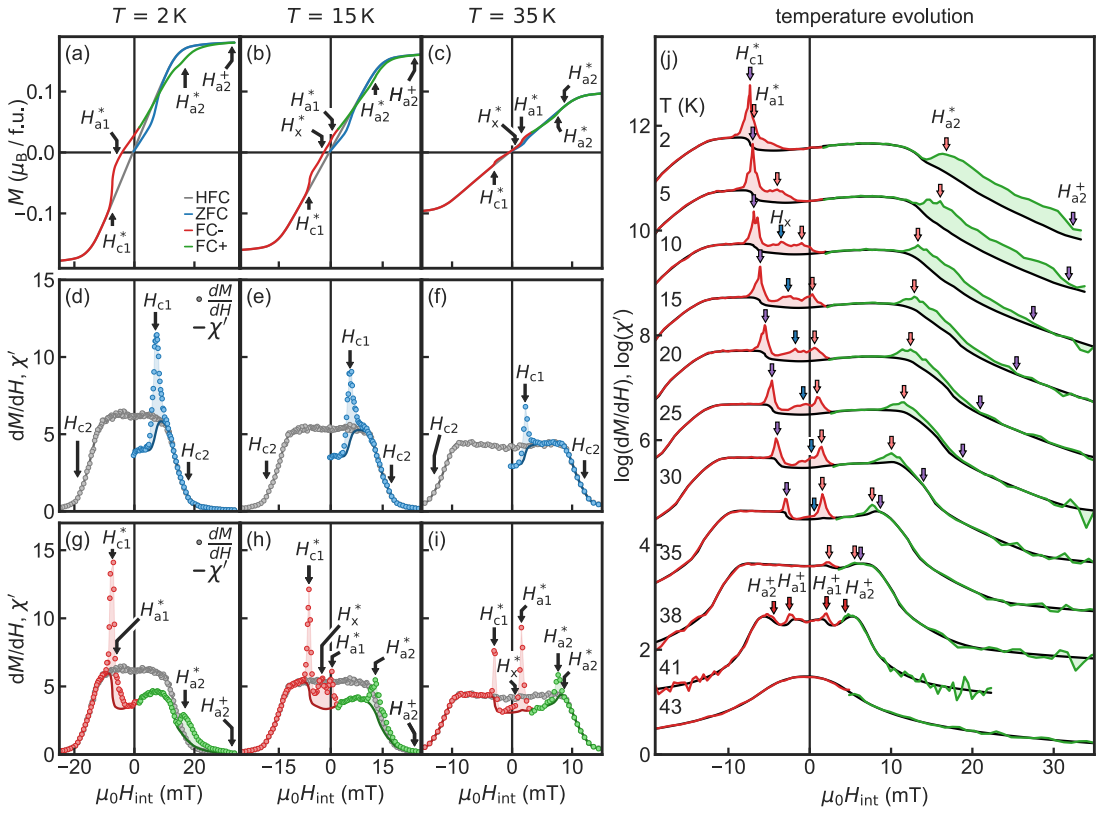

Figure 4.5: Isothermal susceptibility data. (a)–(c) Typical magnetization and susceptibility data recorded in field sweeps at $T = 2\,\mathrm{K}$ (first column), $T = 15\,\mathrm{K}$ (b) and $T = 35\,\mathrm{K}$ following ZFC (blue), HFC (grey), FC+ (green) and FC-(red).

remanten magnetization around $T = 7\,\mathrm{K}$. For comparison, blue symbols demonstrate the measured magnetization following zero-field cooling.

4.1.3 Susceptibility

Having discussed the results of the magnetization measurements, we will now focus on the susceptibility data. Fig. 4.5(a)–(i) displays field dependent magnetization and susceptibility measurements at the three selected temperatures, notably $T = 2\,\mathrm{K}$ (first column), $T = 15\,\mathrm{K}$ (second column) and $T = 35\,\mathrm{K}$ (third column) corresponding to low, intermediate and high temperatures. Data was recorded following ZFC (blue), HFC (grey) and FC (FC+ green, FC- red). The magnetization data is shown in the first row (Fig. 4.5(a)–(c)), for comparison. The susceptibility data following ZFC and HFC is shown in the second row (Fig. 4.5(d)–(f)) and following FC in the third row (Fig. 4.5(g)–(i)). For a better comparison, the HFC susceptibility data is repeated in the third row (Fig. 4.5(g)–(i)).

We begin with a discussion of the ZFC and HFC data. Starting at $T = 2\,\mathrm{K}$, the

differential susceptibility $\mathrm{d}M/\mathrm{d}H$, shown in Fig. 4.5(d) as blue symbols, displays the well known behavior. Starting from $H = 0\,\mathrm{T}$ the system changes from helical to conical order, followed by the field polarized state. This is seen in $\mathrm{d}M/\mathrm{d}H$ as a reduced susceptibility at low fields corresponding to the helical phase followed by a constant plateau in the conical phase and a rapid decline of $\mathrm{d}M/\mathrm{d}H$ down to zero when the field polarized state is entered. The transition fields are marked as H_{c1} and H_{c2}, respectively (c.f. Sec. 4.1.1). The ac-susceptibility χ' (blue line) is in quantitative agreement with $\mathrm{d}M/\mathrm{d}H$ except for a small field range around H_{c1} where slow relaxation processes prevail, attributed to the helix reorientation process [134–137]. The HFC data (grey) shows a similar behavior except for the missing helical phase at low fields, evident from the absence of the minimum in the susceptibility around $H = 0$. This is a well known phenomenon in $\mathrm{Fe}_{1-x}\mathrm{Co}_x\mathrm{Si}$ [46, 90, 135] and suggests a sizable pinning of the helices, possibly due to the prevalent strong compositional site disorder [138].

At intermediate and high temperatures, shown here for the case of $T = 15\,\mathrm{K}$ (Fig. 4.5(e)) and $T = 35\,\mathrm{K}$(Fig. 4.5(f)), the qualitatively same behavior is observed for both ZFC and HFC data. With increasing temperature, only the relevant field scales are reduced.

A markedly more complex behavior is seen when a metastable skyrmion-lattice state is formed when field cooling across the stable skyrmion-lattice phase. Starting again at $T = 2\,\mathrm{K}$ (Fig. 4.5(g)) the field dependent susceptibility differs significantly from that following zero-field or high-field cooling. The susceptibility of the metastable skyrmion lattice measured immediately after field cooling is well below the level of the conical phase and resembles that of the helical phase although an enhanced magnetization is observed (Fig. 4.5(a)). Comparing this with the behavior of the stable skyrmion-lattice phase at high temperatures, we find that the susceptibility of the skyrmion-lattice is again comparable to the helical phase (c.f. Fig. 4.1(c)).

With increasing field (green), both susceptibilities $\mathrm{d}M/\mathrm{d}H$ and χ' remain well below that of the conical state. At high fields approaching saturation the susceptibilities start to decrease strongly. This is comparable to the decrease following HFC occurring in the same field range. During the decrease around $H \approx H_{\mathrm{c2}}$, however, a divergence of the susceptibilities is observed, where $\mathrm{d}M/\mathrm{d}H$ rises above χ' and exhibits a prominent peak denoted as H^{*}_{a2}. The divergent region extends well above H_{c2} deep into the field polarized state up to H^{+}_{a2}, implying a direct transition from the skyrmion to the field-polarized state. Likewise, with a reduction in field (FC-, red), both $\mathrm{d}M/\mathrm{d}H$ and χ' remain below the level of the conical state. At H^{*}_{c1} a sharp maximum appears in $\mathrm{d}M/\mathrm{d}H$ resulting from the collapse of the magnetization down to the value of the conical state (c.f. Fig. 4.5(a)). Furthermore, it is preceded by a small shoulder marked as H^{*}_{a1}. The large peak observed in $\mathrm{d}M/\mathrm{d}H$ is absent in χ'. Rather, χ' jumps directly to the conical level. Above H^{*}_{c1} the conventional behavior is observed with the characteristic field dependence of the conical and the field polarized state at high fields, suggesting a complete destruction of the metastable state. It is worth pointing out that H^{*}_{c1} corresponds to the field scale of the helical to conical transition at H_{c1}, observed after zero-field cooling. The magnetization value, however, is different compared to the magnetization following ZFC.

At $T = 15\,\mathrm{K}$ (Fig. 4.5(h)) several distinct differences may be observed in the field dependence of the susceptibilities $\mathrm{d}M/\mathrm{d}H$ and χ'. Both H^{*}_{a2} and H^{+}_{a2} decrease signifi-

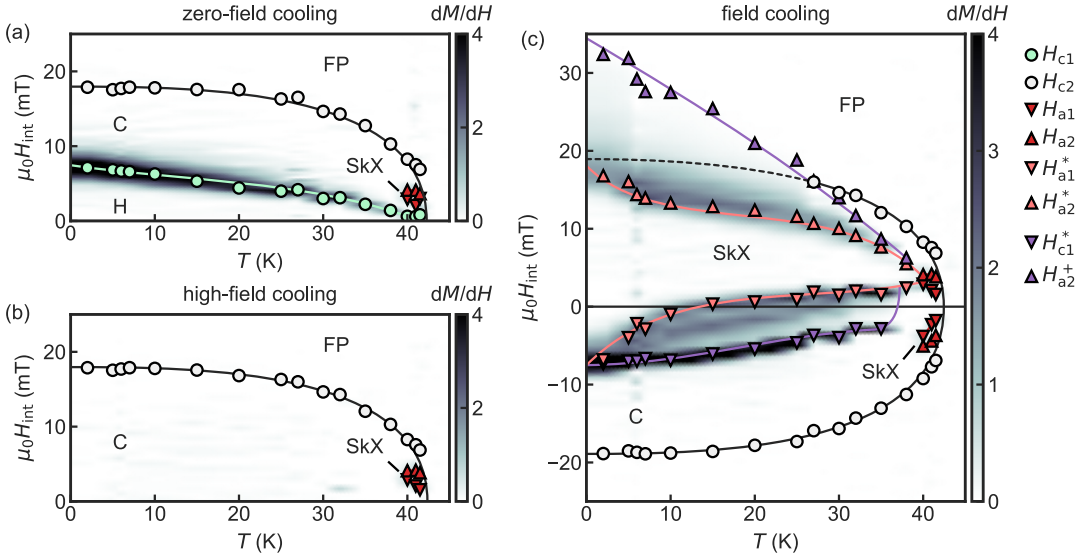

Figure 4.6: Magnetic phase diagram following ZFC (a), HFC (b) and FC (c). Phase boundaries, extracted from susceptibility data, are marked as colored symbols. The colormap reflects $\Delta\chi = \mathrm{d}M/\mathrm{d}H - \chi'$, with dark colors corresponding to large values.

cantely, with H^*_{a2} droping below H_{c2}. Moreover, H^*_{a1} shifts towards positive fields, away from H^*_{c1} and develops into a distinct peak. Between H^*_{a1} and H^*_{c1} both $\mathrm{d}M/\mathrm{d}H$ and χ' do not track each other. $\mathrm{d}M/\mathrm{d}H$ tracks approximately the susceptibility of the conical state, while χ' remains on the level of the helical state. Note that an additional peak of unknown origin emerges in between H^*_{c1} and H^*_{a1}, denoted as H_x.

At $T = 35\,\mathrm{K}$ (Fig. 4.5(i)) the behavior has changed once again. Both H^*_{a2} and H^+_{a2} are further reduced with H^+_{a2} approaching H^*_{a2}. Simultaneously, H^*_{a1} is shifted towards positive fields, narrowing the field region of the metastable skyrmion lattice further. The peak at H^*_{c1} has reduced drastically and H_x has merged with H^*_{a1}.

Fig. 4.5(j) summarizes the evolution with temperature of the field dependent susceptibilities following FC. Note that the logarithm of both dM/dH (colored line) and χ' (black line) is plotted. The data is shifted by a constant offset for clarity. Generally, a smooth evolution of the signatures discussed previously with temperature is observed. Both H^*_{a1} and H^*_{a2} evolve smoothly from H_{a1} and H_{a2}, the phase boundaries of the stable skyrmion lattice phase. Furthermore, the viscous region surrounding H^*_{a2} increases drastically at low temperatures while the viscous region surrounding H^*_{a1} shrinks. H^*_{c1} at negative fields appears to be a hard field limit for the metastable state, below which it does not survive. At $T = 41\,\mathrm{K}$ signatures of the stable skyrmion lattice appear at both positive and negative fields.

4.1.4 Magnetic Phase Diagram

The large amount of data, collected at various temperatures and fields allows the construction of a magnetic phase diagram for each cooling history. The resulting phase diagrams following ZFC, HFC, and FC are shown in Fig. 4.6(a)–(c), respectively. Colored symbols mark the critical fields as defined in earlier sections. The phase diagram is shown with a colormap of the difference of the susceptibilities defined as

$$\Delta\chi = \mathrm{d}M/\mathrm{d}H - \chi'. \tag{4.3}$$

This helps to identify regions in the phase diagram in which relaxation effects occur.

The conventional phase diagram following ZFC is shown in Fig. 4.6(a). It resembles the generic phase diagram of chiral magnets (c.f. Sec. 2.1) with the helimagnetic ground state (H), the conical state at intermediate fields (C), the field polarized state (FP) at high fields and low temperatures and the skyrmion lattice state (SkX) at high temperatures just below T_c and finite fields. A broad region of non-vanishing $\Delta\chi$ is observed around H_{c1}. This frequency dependence is linked to the reorientation process of large domains at H_{c1}. Relaxation effects with finite $\Delta\chi$ also exist in a narrow region surrounding the phase boundary of the skyrmion lattice phase (c.f. Fig. 4.1(c)), but vanish elsewhere. At H_{c2}, for example, no relaxation signal appears as the transition into the field polarized state involves a reversible rotation of the individual spins.

The phase diagram following HFC is shown in Fig. 4.6(b). It is equivalent to the ZFC phase diagram (Fig. 4.6(a)), except for the missing helical phase at low temperatures.

A more complex phase diagram emerges after FC, with the metastable skyrmion lattice covering a major part of the magnetic phase diagram (Fig. 4.6(c)). I may be clearly seen that the phase boundaries of the metastable state (light red symbols) develop smoothly from the phase boundaries of the stable skyrmion lattice phase (red symbols) at high temperatures. Strong relaxation effects (non vanishing $\Delta\chi$) are observed at the phase boundaries of the metastable state, extending up to H_{a2}^{+} at high fields and down to H_{c1}^{*} at low fields. We will show in the following sections that within theses regions, the skyrmion lattice is thermodynamically unstable but kinetically stabilized. In the following sections, we will refer to these regions as the *transition regimes*.

4.2 Magnetic Irreversibility and Relaxation

In this section we will address the stability of the metastable skyrmion lattice state as a function of time. Using time-dependent magnetic relaxation measurements we will investigate the characteristic time and energy scales associated with the decay of the skyrmion lattice in Sec. 4.2.1. We demonstrate that differences in $\mathrm{d}M/\mathrm{d}H$ and χ' are associated with relaxation effects evolving logarithmically in time. The relaxation data is analyzed using a magnetic viscosity model. Sec. 4.2.3 demonstrates the irreversible behavior of the remanent magnetization of the metastable state. In Sec. 4.2.4, we apply so-called master curve scaling to the relaxation data which allows us to extract the distribution of activation energies.

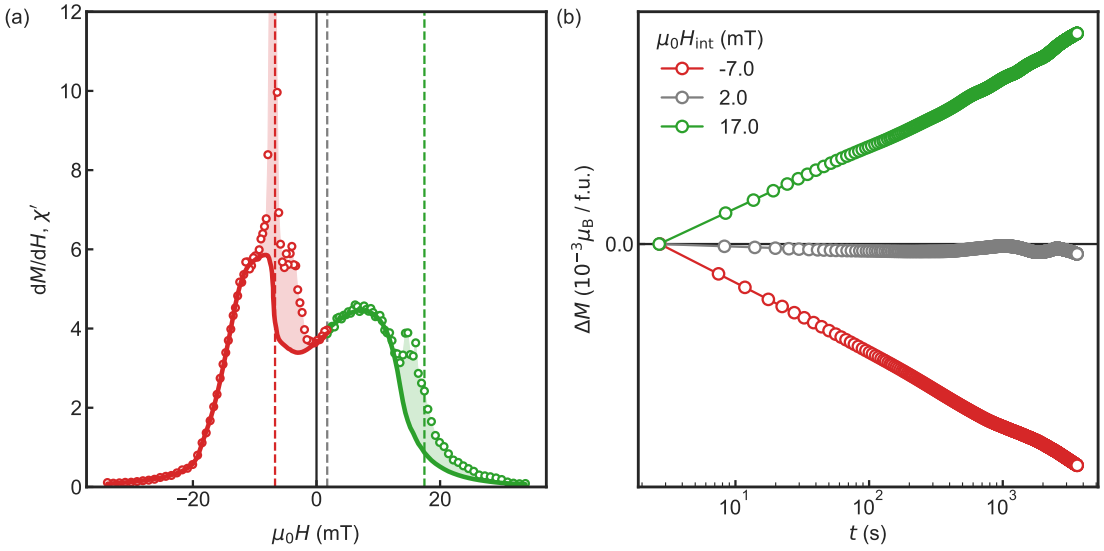

Figure 4.7: Susceptibilities and magnetic relaxation data. (a) Differential susceptibility $\mathrm{d}M/\mathrm{d}H$ (symbols) and real part of ac-susceptibility χ' (lines) as a function of internal field. Data is recorded at $T = 3\,\mathrm{K}$ after field cooling across the skyrmion lattice state. (b) Relaxation of magnetization as a function of time at $T = 3\,\mathrm{K}$ and $H_{\mathrm{int}} = -7\,\mathrm{mT}$, $H_{\mathrm{int}} = 2\,\mathrm{mT}$ and $H_{\mathrm{int}} = 18\,\mathrm{mT}$. Initial magnetization has been subtracted for clarity. Vertical dashed lines in (a) mark fields in which the magnetic relaxation measurements were carried out.

4.2.1 Magnetic Relaxation

The transition from the metastable state to conventional order is characterized by a broad field region in which sizable differences between $\mathrm{d}M/\mathrm{d}H$ and χ' are observed. These differences, as stated before, suggest the presence of slow viscous relaxation processes. To investigate the relaxation process further, we have carried out time-dependent magnetic relaxation measurements.

For these measurements the system was prepared in a similar fashion to the field dependent measurements: First, the sample was cooled to the target temperature in an applied field of $B = 10\,\mathrm{mT}$ across the skyrmion lattice state with a cooling rate of $5\,\mathrm{K\,min^{-1}}$. Subsequently, the field was changed to the desired target field and the measurement was started immediately afterward.

Fig. 4.7(a) presents susceptibility data at $T = 3\,\mathrm{K}$ after field cooling across the skyrmion lattice state. The differential susceptibility $\mathrm{d}M/\mathrm{d}H$ (symbols) and the real part of the ac-susceptibility χ' (lines) are shown as a function of internal field. At both high and low fields, sizable differences between $\mathrm{d}M/\mathrm{d}H$ and χ' may be seen. Typical magnetic relaxation data at $T = 3\,\mathrm{K}$ and three different fields $H_{\mathrm{int}} = -7\,\mathrm{mT}$ (red), $H_{\mathrm{int}} = 2\,\mathrm{mT}$ (grey) and $H_{\mathrm{int}} = 18\,\mathrm{mT}$ (green) are shown in Fig. 4.7(b). Vertical dashed lines in Fig. 4.7(a) mark fields at which the magnetic relaxation measurements were carried out.

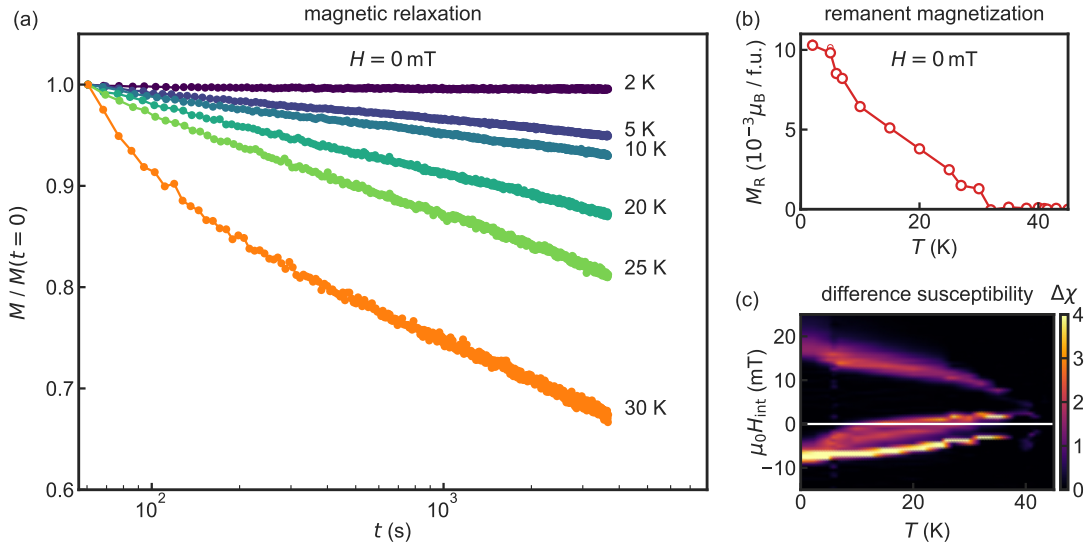

Figure 4.8: Relaxation of the remanent magnetization ($B = 0$) after field cooling across the skyrmion lattice state at various temperatures. (a) Remanent magnetization at selected temperatures as a function of time. Magnetization is normalized to the initial value. (b) Remanent magnetization as a function of temperature. (c) Difference of $\mathrm{d}M/\mathrm{d}H$ and χ' measured in field sweeps following field cooling in 10 mT.

For a better comparison, the initial magnetization value was subtracted.

The relaxation data at $H_{\mathrm{int}} = 2\,\mathrm{mT}$ (grey) was measured immediately after the cool-down without a change of the applied magnetic field. Note that due to demagnetizing effects an applied field of $B = 10\,\mathrm{mT}$ here corresponds to $H_{\mathrm{int}} = 2\,\mathrm{mT}$. On the timescale of the experiment, no significant change in magnetization was observed, suggesting a stable state. In contrast, the relaxation curves at $H_{\mathrm{int}} = 18\,\mathrm{mT}$ (green) and $H_{\mathrm{int}} = -7\,\mathrm{mT}$ (red) show distinct changes as a function of time. As expected, the magnetization decays towards the HFC magnetization value, resulting in an increase of M for $H_{\mathrm{int}} = 18\,\mathrm{mT}$ and a decrease of M for $H_{\mathrm{int}} = -7\,\mathrm{mT}$. Surprisingly, a logarithmic dependence of the magnetization as a function of time is found, which we address in detail in the following sections.

So far we have demonstrated that differences in $\mathrm{d}M/\mathrm{d}H$ and χ' are indeed linked to relaxation effects. We now focus on the relaxation in zero field, where a sizable remanence is found following field cooling. As a reminder, Fig. 4.8(b) repeats the previously shown remanent magnetization as a function of temperature. The remanent magnetization exhibits a linear temperature dependence in a broad temperature range with a step-like increase of M_{R} around $T = 7\,\mathrm{K}$. For comparison, the difference of $\mathrm{d}M/\mathrm{d}H$ and χ' is shown in Fig. 4.8(c) with $H_{\mathrm{int}} = 0$ indicated as a white line. Comparing Fig. 4.8(b) and Fig. 4.8(c), it is evident that the step-like reduction of the remanent magnetization occurs when the system enters the temperature range where sizable differences between $\mathrm{d}M/\mathrm{d}H$

and χ' prevail, and relaxation effects of the remanence are expected.

The relaxation of the remanent magnetization with time is shown in Fig. 4.8(a) for various temperatures. The data is normalized to the initial magnetization value for better comparison. Data are recorded continuously over a period of one hour. The relaxation data is quite revealing in several ways. First, at $T = 2\,\mathrm{K}$, $M(t)$ is almost constant. With increasing temperature, however, the relative relaxation rate increases significantly in strength, indicating a thermally activated relaxation process. Secondly, a logarithmic dependence of the magnetization on time is observed, that may be described by the relation

$$M(t) = K + S \cdot \ln(t/t_0) \tag{4.4}$$

with the magnetic viscosity constant S and material and experiment specific parameters K and t_0. This is the widely used magnetic viscosity relation [18–22, 24] The divergence for $t \to 0$ and $t \to \infty$, however, shows that Eq. 4.4 is necessarily an approximation. Moreover, a change in t_0 is indistinguishable from a shift in K. An improved approximation, especially at short times, is given by

$$M(t) = M(0) + Sln(1 + t/t_0), \tag{4.5}$$

with $M(0)$ corresponding to the magnetization at the starting time, and the time constant t_0. Here, $M(0)$ and t_0 have distinct roles but are still empirical parameters.

4.2.2 Magnetic Viscosity

In the following, we will apply the viscosity model to the relaxation measurements. Fitting the magnetic viscosity model of Eq. 4.5 to the relaxation data at $B = 0$ at various temperatures, we obtain the initial magnetization $M(0)$ and magnetic viscosity parameter S. Both $M(0)$ and S are shown as a function of temperature in Fig. 4.9(a) and Fig. 4.9(b) as black symbols, respectively. $M(0)$ reflects the behavior of the remanent magnetization extracted from hysteresis loops (c.f. Fig. 4.3(b)). That is, a linear temperature dependence below $T \approx 37\,\mathrm{K}$ with a step-like jump of M_R around $T = 7\,\mathrm{K}$. Above $T \approx 37\,\mathrm{K}$, $M(0)$ is essentially zero. The most striking behavior, however, is seen in the temperature dependence of the viscosity parameter S. With decreasing temperature, a sizable viscosity coefficient, S, emerges around $T \approx 37\,\mathrm{K}$, precisely where the remanent magnetic moment appears. From $T \approx 30\,\mathrm{K}$ down to $T \approx 10K$, S remains at an approximately constant value of $S \approx 100 \times 10^{-6}\,\mu_\mathrm{B}$/f.u.. Below $T \approx 10\,\mathrm{K}$, a sharp peak appears with S almost doubling in value, followed by a rapid decrease of S towards zero. That means when the system enters the transition regime, a drastic increase in the decay rate occurs. Within the transition regime, however, the decay rate is almost constant.

A similar analysis at an applied field of $B = 30\,\mathrm{mT}$ yields a different result. The fitted model parameters are shown in Fig. 4.9 as green symbols. Note that the corresponding magnetization value following ZFC has been subtracted from the initial magnetization $M(0)$. As a function of increasing temperature, the initial magnetization is essentially constant up to $T \approx 25\,\mathrm{K}$ and decreases linearly at higher temperatures. Above $T \approx 25\,\mathrm{K}$

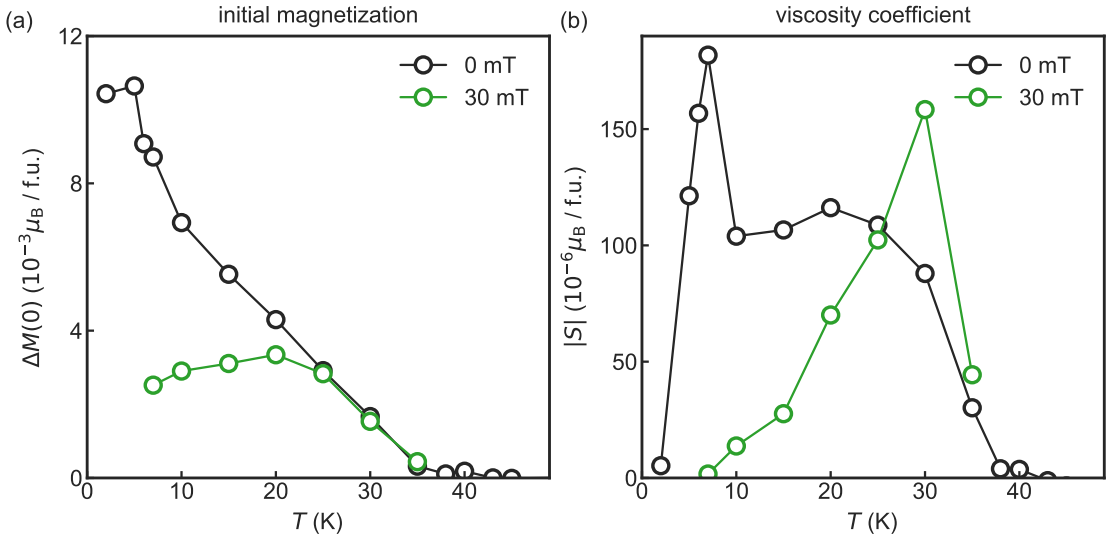

Figure 4.9: Model parameters of fitted relaxation curves at $B = 0\,\mathrm{mT}$ (black) and $B = 30\,\mathrm{mT}$ (green) using the magnetic viscosity model of Eq. 4.5. Initial magnetization $M(0)$ (a) and magnetic viscosity parameter S (b) as a function of temperature.

the fitted initial magnetization of $B = 0$ and $B = 30\,\mathrm{mT}$ are comparable. In contrast to the zero-field data, the viscosity parameter increases linearly up to $T = 30\,\mathrm{K}$, before dropping rapidly.

4.2.3 Irreversibility of the Remanent Magnetization

The remanent magnetization that is observed following field cooling shows an unusual linear dependence on temperature and additionally exhibits logarithmic relaxation effects. Two distinct mechanisms may be responsible for this peculiar temperature dependence. It either shows the intrinsic temperature dependence of a skyrmion lattice in zero field, or it results from an instantaneous decay of volume fractions of the metastable state with temperature. To investigate this open question we have carried out first order temperature reversal measurements according to the following protocol: First the sample was cooled across the skyrmion lattice phase in an applied field of $B = 10\,\mathrm{mT}$ down to $T = 2\,\mathrm{K}$ with a cooling rate of $20\,\mathrm{K\,min^{-1}}$. Then, the applied field was set to zero. Subsequently, the magnetization was recorded while sweeping the temperature with a constant rate of $0.25\,\mathrm{K\,min^{-1}}$. To investigate the reversibility, the sweep direction was reversed at specific temperatures.

The resulting magnetization data as a function of temperature is shown in Fig. 4.10. Colored arrows indicate the sweep direction. The temperature dependent magnetization curve shown in Fig. 4.10(a) corresponds to a temperature sweep from $T = 2\,\mathrm{K}$ to $T = 55\,\mathrm{K}$. It resembles the temperature dependence of the remanent magnetization extracted from

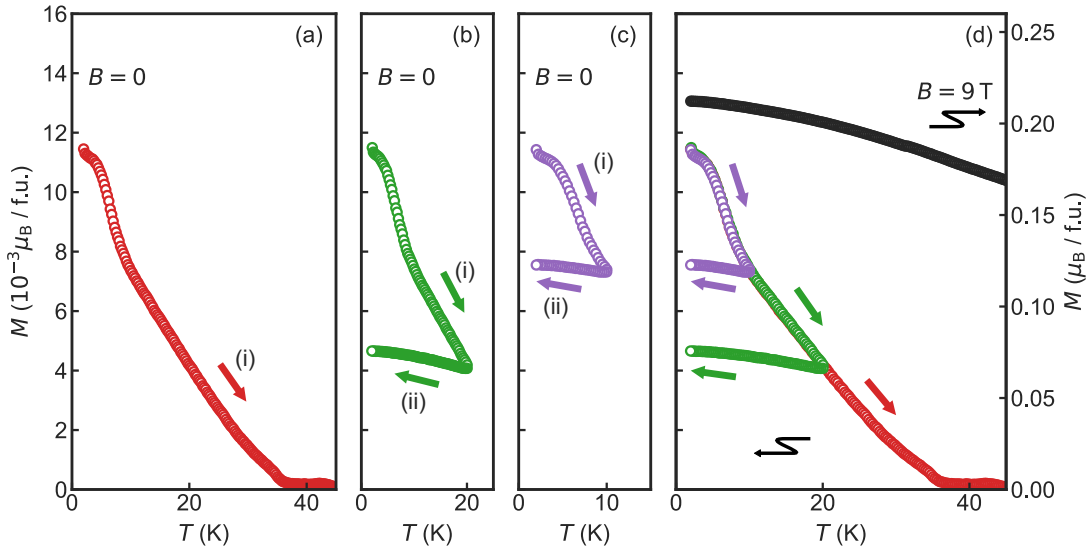

Figure 4.10: Irreversibility of remanent magnetization. (a)–(c) Remanent magnetization as a function of temperature following FC. The sweep direction is indicated with an arrow. For the temperature sweep measurements shown in green (b) and purple (c), the sweep direction was reversed at $T = 20\,\mathrm{K}$ and $T = 10\,\mathrm{K}$, respectively. (d) Comparison of the temperature sweeps shown in (a)–(c) as well as the temperature dependence of the magnetization at $B = 9\,\mathrm{T}$, deep within the field-polarized state.

field scans. That is a linear temperature dependence below $T \approx 37\,\mathrm{K}$ with a step-like change of M_R around $T = 7\,\mathrm{K}$. A drastically different behavior is observed when the sweep direction is reversed at an intermediate temperature as shown in Fig. 4.10(b) and Fig. 4.10(c). Here, the sweep direction has been reversed at $T = 20\,\mathrm{K}$ and $T = 10\,\mathrm{K}$, respectively. A comparison of all temperature sweeps is shown in Fig. 4.10(d).

For increasing temperature, both curves follow the magnetization of the conventional temperature sweep curve, as expected. As the sweep direction is reversed, however, the magnetization remains almost constant and does not track it's previous path. A minor increase of the magnetization with decreasing temperature is seen resulting solely from the increase of the saturation moment with decreasing temperature. This is illustrated in Fig. 4.10(d), showing the temperature dependence of the magnetization at a large magnetic field of $B = 9\,\mathrm{T}$, deep within the field polarized state.

This observation has two implications: First, the increase in temperature obviously triggers part of the remanent magnetization to decay. Second, besides the fact that the remanent magnetization is not recovered, additional relaxation is also not observed when the temperature is reduced.

This may be understood by considering the theory of magnetic viscosity. As shown in Sec. 1.2, the relaxation front, E^*, depends linearly on temperature and logarithmically on time. The resulting implications may be understood with the following Gedankenex-

periment: Assuming that at time t after the beginning of the relaxation, the temperature is changed instantaneously from T to $T + \Delta T$, we will observe a change in magnetization. The change in M results from two individual contributions, a reversible and an irreversible part: The reversible change in M results from the temperature dependence of the ordered magnetic moment. This is indicated in Fig. 4.10(d), showing the saturated moment as a function of temperature (black symbols) extracted from a temperature sweep at $B = 9\,\mathrm{T}$. With an increase in temperature, a clear decrease in magnetic moment is observed. This process is completely reversible and does not involve an energy barrier and therefore no relaxation. The irreversible contribution results from the linear dependence of the relaxation front on temperature. A change in temperature $T \to T + \Delta T$ implies a change in the relaxation energy $E^* \to E^* + \Delta E$. For $\Delta E > 0$ this leads to an instantaneous decay of the volume fractions related to the energy barriers in the interval $[E^*, E^* + \Delta E]$. For $\Delta E < 0$, however, the relaxation front is shifted back to lower energies. The volume fractions in this energy interval have already decayed. As a result, the relaxation halts until the advancement in time compensates for ΔE.

Both situations may be observed in the temperature sweeps of Fig. 4.10. First, as a function of increasing temperature, the relaxation front moves towards larger energies driven by the increase in temperature and the advancement of time. The observed almost linear decrease of M in a broad temperature range implies that the relaxation front E^* advances over a broad but flat distribution of activation energies. By reversing the sweep direction, the relaxation front is forced towards lower energies due to the decrease in temperature. At the same time, the advancement in time forces it towards larger energies. The effect of temperature, however, dominates as the relaxation front advances logarithmically in time.

4.2.4 Distribution of Activation Energies

In this section, we return to the magnetic relaxation data in zero field. We are going to show that all relaxation measurements at different temperatures can be accounted for in terms of a single master curve from which we are going to infer the distribution of activation energies.

The relaxation front for E^*, as discussed in Sec. 1.2, depends on both temperature and time. As a result, relaxation measurements at different temperatures sample different regions of the barrier distribution $n(E)$. Relaxation measurements at low temperatures sample only the low energy region of the barrier distribution. Due to the logarithmic dependence on time huge experimentally inaccessible timescales would be required to reach the high energy regions. These could easily exceed the age of the universe [24]. Relaxation measurements at high temperatures, on the other hand, would require exceptionally fast measurements to sample the low energy portion of the barrier distribution. This makes it difficult, if not impossible, to observe the relaxation over the complete barrier distribution at a single temperature. These difficulties may be overcome with the use of the time-temperature superposition principle.

The time-temperature superposition principle allows for the creation of a single master curve from relaxation measurements at various temperatures. It states that all relaxation

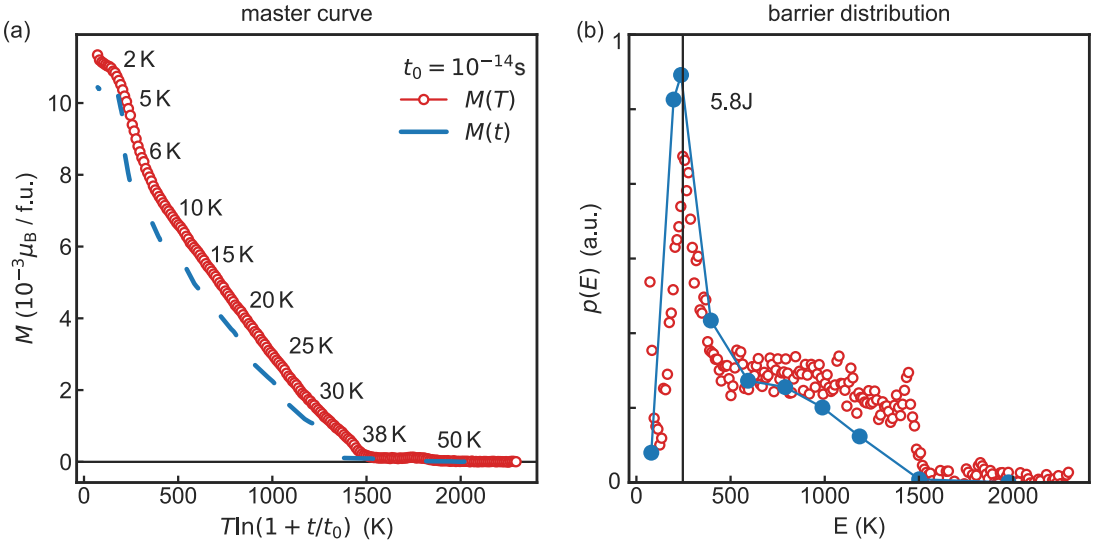

Figure 4.11: (a) Master curve of the remanent magnetization as a function of energy. A characteristic time $t_0 = 1 \times 10^{-14}$ s is observed. Blue line segments correspond to isothermal relaxation measurements at various temperatures. For comparison, red symbols show a temperature sweep from $T = 2$ K to $T = 55$ K with a sweep rate of 0.25 K min^{-1} expressed as a function of energy using the same t_0. (b) Distribution of activation energies, inferred from the master curve (blue). Note that for clarity, only the average gradient of each relaxation measurement, corresponding to the viscosity coefficient, is shown. Additionally, the distribution is also calculated from the temperature sweep (red).

data will merge into a single smooth curve if plotted as a function of the relaxation front energy $E = k_B T \ln(t/t_0 + 1)$. This concept is heavily used in the field of polymer physics and glass-forming liquids, amongst other areas, to extrapolate the viscosity in experimentally unreachable parameter regions [140–142]. It has also been used in spin-glasses, vortex matter and weakly interacting ferromagnetic single domain particle systems to study the magnetic relaxation or magnetic viscosity (hence the name)[129, 131, 132]

Applying the concept of master curve scaling to the relaxation data in zero field, we find that a master curve forms when a characteristic time of $t_0 = 1 \times 10^{-14}$ s is chosen. The master curve constructed from the relaxation data at $B = 0$ is shown in Fig. 4.11(a). Each blue shaded segment corresponds to a relaxation measurement. The master curve has been corrected for the temperature dependence of M_s. Details on how the graph is constructed may be found in Sec. 3.4.1.

With the knowledge of t_0 it is possible to express data recorded in a temperature sweep as a function of the relaxation front energy, as well. This is shown in Fig. 4.11(a) with red symbols corresponding to a temperature sweep from $T = 2$ K to $T = 55$ K at a sweep rate of 0.25 K min^{-1}. As expected, both curves are almost identical. There are however minor

differences, as the temperature sweep data appears slightly larger. This may be explained as follows. The elevated magnetization observed in the temperature sweep results from a faster cooling rate of $20\,\mathrm{K\,min^{-1}}$ during the initial field cooling of the temperature sweep as compared to the $5\,\mathrm{K\,min^{-1}}$ used for the relaxation measurements. As shown in Sec. 4.1.2, this results in a larger remanent magnetization. Furthermore, between the recording of the relaxation data and the temperature sweeps , the PPMS cryostat was out-of-order with the superconducting magnet at room temperature. As a result, slight differences arise due to the remanent field of the superconducting magnet that cannot be avoided. Bottom line, the master curve can be constructed from temperature sweeps when t_0 is known which has several advantages, such as more regular data spacing.

Having demonstrated master curve scaling, we will now show how the effective barrier distribution may be inferred from the master curve. As shown in Sec. 1.2, the relaxation of the magnetization obeys

$$\Delta M(t) = N \langle \Delta m \rangle \int_0^{E^*(t)} p(E) dE \tag{4.6}$$

By taking the derivative of Eq. 4.6 with respect to E^*, we obtain

$$\frac{\mathrm{d}M}{\mathrm{d}E^*} = \frac{\mathrm{d}}{\mathrm{d}E^*} \left(N \langle \Delta m \rangle \int_0^{E^*} p(E) dE \right) = N \langle \Delta m \rangle \, p(E^*) \propto p(E^*) \tag{4.7}$$

This shows that the derivative of the master curve with respect to E^* allows to infer the distribution of activation energies. The numeric derivative of the master curve is shown in Fig. 4.11(b). Red symbols correspond to the numerical derivative of the master curve constructed from the temperature sweep with respect to E^*. For clarity, only the average derivative of each relaxation curve is shown as blue symbols. The barrier distribution consists of a narrow peak at low energies followed by a broad and flat distribution extending up to $E \approx 1500\,\mathrm{K} \approx 35 \cdot J$ with $J \approx T_\mathrm{c} = 42.5\,\mathrm{K}$. The narrow peak is centered at $E = 246\,\mathrm{K} \approx 5.8 \cdot T_\mathrm{c} = 5.8 \cdot J$ which is in exceptional agreement with theoretical calculations of Schütte and coworkers [72]. The implications of this will be discussed in detail in the following section.

Note that the precise determination of t_0 is not critical in the low energy region. Variations of t_0 have only minor effects on the position of the narrow peak. Increasing or decreasing t_0 by an order of magnitude only leads to a shift of $\Delta E \approx \pm 15\,\mathrm{K}$. The influence on higher energy regions is more pronounced.

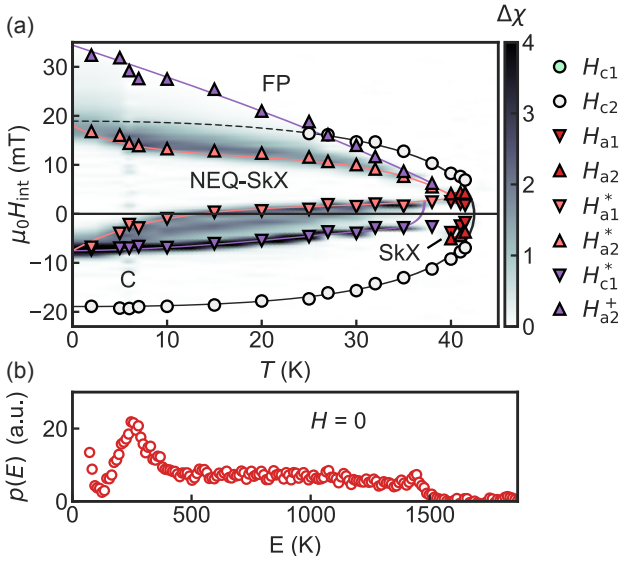

Figure 4.12: (a) Nonequilibirum phase diagram following field cooling (c.f. Fig. 4.6) Light red shading indicates the temperature and field region of the thermodynamically metastable skyrmion lattice. Within the yellow shaded transition region, the skyrmion lattice is thermodynamically unstable but kinetically stabilized. (b) Distribution of activation energies at $B = 0$ (c.f. Fig. 4.11).

4.3 Discussion

The discussion of the experimental results is divided into two parts and proceeds as follows. First, in Sec. 4.3.1, we focus on the relaxation behavior in zero field, where we will show that the nonequilibrium skyrmion lattice is stabilized beyond topological protection. Secondly, in Sec. 4.3.2, we discuss the field dependence of the nonequilibrium skyrmion lattice.

4.3.1 Stabilization Beyond Topological Protection

The characteristics of the metastable state in zero field are of particular interest for potential applications. Experimentally, we observe the metastable skyrmion lattice state at $H = 0$ in an exceptionally wide temperature range, ranging from lowest temperatures up to $T \approx 35\,\mathrm{K} \approx 0.8 T_{c2}$. For temperatures between $7\,\mathrm{K} \leq T \leq 35\,\mathrm{K}$, however, enhanced relaxation effects are observed. Here the sample is located within the transition regime, marked as a purple region within the phase diagram. Nonetheless, the metastable state is still remarkably stable due to the logarithmic dependence on time. At $T = 20\,\mathrm{K}$ for example, an exceptionally long time frame in the order of $1 \times 10^{40}\,\mathrm{s}$ would be required for all skyrmions to relax[1]. This is more than twice the age of the universe.

[1]The time frame is estimated from the relaxation data, under the assumption that the relaxation remains logarithmic at all times.

The effective distribution of activation energies at $H = 0$, as determined from relaxation data in Sec. 4.2.4, is shown in Fig. 4.12(b). It consists of a large peak centered at $E \approx 246\,\mathrm{K} \approx 5.8\,J$ with $J \approx k_\mathrm{B}T = 42.5\,\mathrm{K}$, followed by a broad shoulder extending up to $E \approx 1500\,\mathrm{K} \approx 35\,J$.

The energetics of the unwinding process of a single skyrmion within a helical environment at low fields have been studied theoretically by C. Schütte and A. Rosch [72]. Using micromagnetic simulations based on the stochastic Landau-Lifschitz-Gilbert equation they predict an activation energy for the nucleation of monopole-antimonopole pairs of $E_{\mathrm{MP-AMP}} \approx 5.8\,\mathrm{J}$ in zero field. Similar results have been found for Bloch points in magnetic vortex core reversal processes [70]. This may be understood easily by considering a simple Heisenberg model on a cubic lattice with J being the Heisenberg exchange energy. By nucleating a Bloch point, a magnetic spin configuration with a core of vanishing magnetization, we change the energy of the system by $6J$, a single J for each broken bond between the spin at its six nearest neighbors. By comparing these theoretical predictions with the experimentally determined effective distribution of activation energies we find exceptional agreement of the peak energy with the predicted monopole-antimonopole nucleation barrier, corroborating the theory.

Theoretically, a rapid decay of the metastable skyrmion lattice is expected as soon as the lifetime associated with the nucleation energy barrier is reduced thermally to experimental timescales. This occurs in our experiments at approximately $T \approx 7\,\mathrm{K}$ in zero field and correlates with the appearance of the divergence between $\mathrm{d}M/\mathrm{d}H$ and χ', marked as H^*_{a1}. Surprisingly, the skyrmion lattice survives up to $T = 35\,\mathrm{K}$ despite the thermal energy exceeding the topological protection. This results from the broad distribution of activation energies, extending up to $E = 1500\,\mathrm{K}$, almost six times the topological nucleation barrier. Within this region and on experimentally probed timescales, the skyrmion lattice is thermodynamically unstable but kinetically stabilized. In zero field, the kinetic energy barriers dominate the energetics, yielding a skyrmion lattice stabilized beyond topological protection.

The most likely origin of the broad distribution of activation energies is pinning of (anti-)monopoles, arresting the transition in a transient state. (Anti-)monopoles, in contrast to skyrmions, are particullarily sensitive to pinning due to their singular core [46, 72]. With $Fe_{0.5}Co_{0.5}Si$ known to exhibit strong compositional site disorder, this mechanism is more than likely [90, 138, 143]. This is further corroborated by results of Wild and coworkers[95], reporting an exponential decay of the metastable skyrmion lattice in heavily thinned $Fe_{0.5}Co_{0.5}Si$ platelets using Lorentz transmission electron microscopy. The activation energies inferred by Wild and coworkers of $\Delta E = 32\,\mathrm{meV} \approx 370\,\mathrm{K}$ at $B = 7.3\,\mathrm{mT}$ and $\Delta E = 15\,\mathrm{meV} \approx 175\,\mathrm{K}$ at $B = -2.6\,\mathrm{mT}$ are comparable to the nucleation barrier inferred in this thesis of $\Delta E \approx 246\,\mathrm{K}$ at $B = 0$ (c.f. Sec. 4.2.4). The exponential relaxation suggest further that the broad distribution is absent. Considering that the length of skyrmion tube is of the order of the sample thickness, a reduction in sample thickness reduces the distance that monopoles have to travel, which in turn reduces the likelihood of monopoles to get trapped.

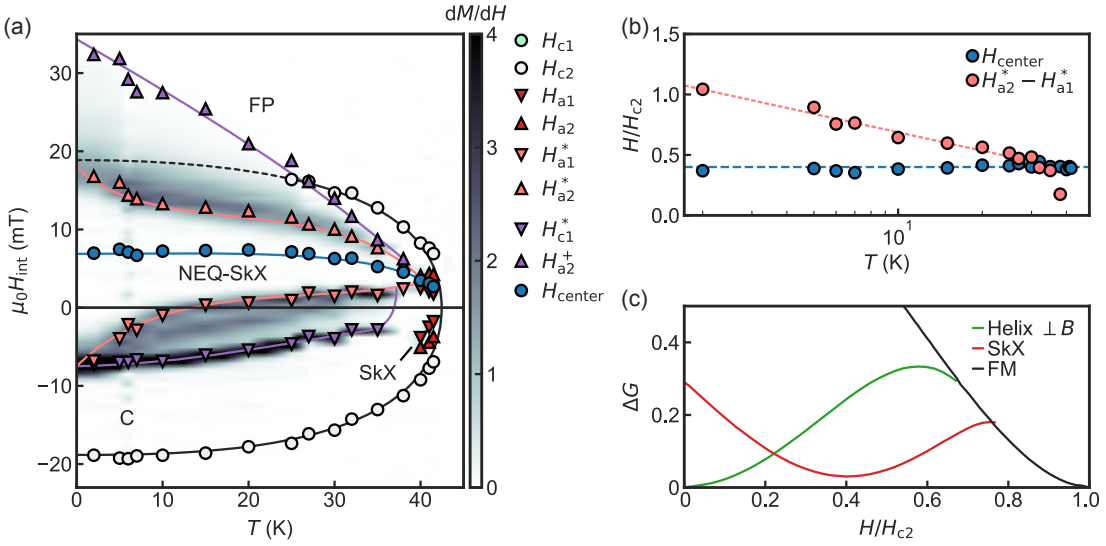

Figure 4.13: (a) Previously shown magnetic phase diagram following FC (c.f. Fig.4.6(c)). The calculated center field $H_{\text{center}} = (H_{a2} + H_{a1})/2$ of the metastable skyrmion lattice state is shown as blue symbols. Blue dashed line corresponds to $0.4H_{c2}$. (b) Temperature evolution of the center field of the skyrmion lattice state (blue symbols) and the width of the skyrmion lattice state (red symbols) normalized to H_{c2}. $B = 0.4 \cdot H_{c2}$ is indicated as a dashed blue line. (c) Field dependent free energy of various magnetic states relative to the conical state. We distinguish a ferromagnetic state(black), a helical state with $\mathbf{B} \perp \mathbf{k}$ (green) and the skyrmion lattice state (red). Data taken from Supplement of [37].

4.3.2 Nonequilibrium Magnetic Phase Diagram

We now turn to the magnetic field dependence of the metastable skyrmion lattice. The metastable state, as depicted in Fig. 4.13(a), is bounded by the transition lines at $H^*_{a1}(T)$ and $H^*_{a2}(T)$ at low and high fields, respectively. As stated before, $H^*_{a1}(T)$ is associated with the monopole-antimonopole nucleation barrier. Similarly, the decay at high fields is expected to proceed via monopoles as well, with H^*_{a2} tracking the nucleation barriers at high fields. At these transition lines, the thermal energy reduces the field dependent lifetime into experimentally probed timescales.

As a function of temperature, the transition lines appear to be centered around a special field value, running in parallel to H_{c2}. To confirm this observation, the calculated center field

$$H_{\text{center}} = \frac{1}{2}\left(H^*_{a1} + H^*_{a2}\right) \tag{4.8}$$

is shown in Fig. 4.13(b) as blue symbols, normalized to H_{c2} . The center field is also plotted within the phase diagram as blue symbols. From the graph in Fig. 4.13(b) it is

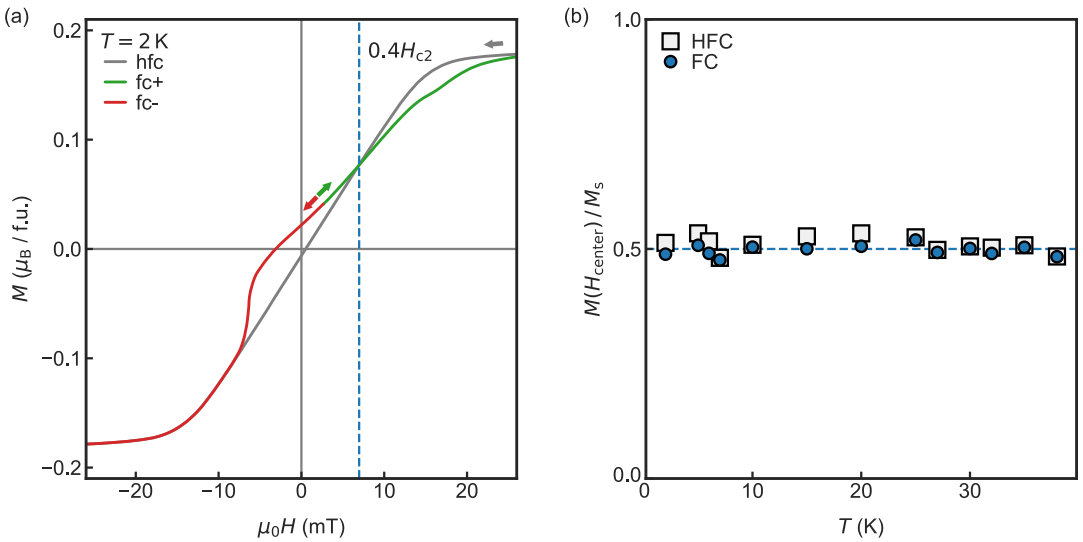

Figure 4.14: (a) Magnetization at $T = 2\,\mathrm{K}$ following HFC (grey), FC+ (green) and FC- (red). Blue dashed vertical line indicates H_{center}. (b) Magnetization value as a function of temperature at the center field $H_{\mathrm{center}} \approx 0.4 H_{\mathrm{c2}}$ following FC (blue) and HFC (grey).

obvious that the critical fields H^*_{a1} and H^*_{a2} are indeed centered around

$$H_{\mathrm{center}} \approx 0.4 \cdot H_{\mathrm{c2}}. \tag{4.9}$$

Comparing this result with theoretical calculations of the field dependent free energy, we find that the energy of the skyrmion lattice with respect to the ground state is minimal at $0.4 \cdot H_{\mathrm{c2}}$ [37]. This is illustrated in Fig. 4.13(c), showing the calculated free energy density of various magnetic states relative to the conical state.

Next we address the variations of the transition lines. The distance between the transition line and the center field

$$H_{\Delta \mathrm{a}} = \frac{1}{2}\left(H^*_{\mathrm{a2}} - H^*_{\mathrm{a1}}\right) \tag{4.10}$$

is shown in Fig. 4.13(b) as red symbols with respect to H_{c2}. With increasing temperature, $H_{\Delta \mathrm{a}}$ decreases proportional to the logarithm of the temperature or in other words, the corresponding temperature increases exponentially as the magnetic field approaches the center field H_{center}. This compares with micromagnetic simulations of Schütte and Rosch [72] who found an exponential dependence of the nucleation rate on field according to $\Gamma \propto \exp(-B/B_0)$ [72] They attribute this to a field dependence of the activation energy and the attempt time.

Another surprising finding concerns the magnetization following FC at the center field $M_{\mathrm{FC}}(0.4 H_{\mathrm{c2}})$, shown in Fig. 4.14(b) as red symbols, normalized to the saturation magnetization. It reveals an essentially constant value of $M_{\mathrm{FC}}(0.4 H_{\mathrm{c2}})/M_{\mathrm{s}} = 0.5$ as a

function of temperature. For comparison grey symbols show the magnetization following HFC at the same magnetic field $M_{\mathrm{HFC}}(0.4H_{c2})$, which surprisingly shows approximately the same magnetization value as the FC. This implies that the intersection of both magnetization curves occurs always at the center field. As an example, Fig. 4.14(a) presents the magnetization curves at $T = 2\,\mathrm{K}$, with a dashed blue line marking $0.4 \cdot H_{c2}$. This implies that both states, skyrmion lattice and conical helix, posses the same Zeeman energy at the center field, which might help in stabilizing the skyrmion lattice state.

4.4 Nonequilibrium Skyrmion Lattices in Chiral Magnets

In this section we compare the nonequilibrium phase diagram of $Fe_{0.5}Co_{0.5}Si$ with metastable skyrmion lattices reported in other cubic chiral magnets. We discuss common features as well as differences. Since the first discovery in $Fe_{1-x}Co_xSi$, metastable skyrmion lattices have been found in a variety of materials. To understand the generic features of the metastable state, it is instructive to compare $Fe_{1-x}Co_xSi$ with other materials.

Typical phase diagrams hosting a metastable skyrmion lattice are presented in Fig. 4.15. These belong to $Fe_{0.5}Co_{0.5}Si$ (Fig. 4.15(a)), inferred in this thesis, $Co_9Zn_9Mn_4$ [34] (Fig. 4.15(b)), MnSi [91] (Fig. 4.15(c)) and Cu_2OSeO_3 [93] (Fig. 4.15(d)). At first glance, all phase diagrams look very similar despite the fact that all these materials have distinctly different temperature and field scales. These generic properties may be summarized as follows: (i) The metastable state is generated by field cooling across the skyrmion lattice state. In case of MnSi and Cu_2OSeO_3, however, additional measures must be taken which will be addressed below. (ii) The metastable state covers a major region of the magnetic phase diagram, increasing in field range with decreasing temperature. (iii) The metastable state is centered around $\approx 0.4 \cdot H_{c2}$, plotted within the phase diagram as a dashed blue line. Blue symbols correspond to the center field H_{center}, calculated from the upper and lower phase boundary.

The existence of such generic characteristics across vastly different materials is another testimony of the generic nature of skyrmions in chiral magnets. Nevertheless, some distinct differences are present. In both $Fe_{0.5}Co_{0.5}Si$ and $Co_9Zn_9Mn_4$ the metastable skyrmion lattice state can be formed simply by field cooling across the thermodynamically stable skyrmion lattice state using moderate cooling rates ($\approx 10\,\mathrm{K/\,min}$), whereby in MnSi (Fig. 4.15(c)), rapid quenching ($\gtrsim 400\,\mathrm{K/\,min}$) of the stable skyrmion state is neccessary[91]. The stable and metastable state are separated from each other by a small temperature window in which fast relaxation rates prevail. It must be crossed as fast as possible to prevent the disintegration of the skyrmion lattice.

Similarly, the metastable skyrmion lattice in Cu_2OSeO_3 is also separated from the stable skyrmion lattice phase by a finite temperature window and moderate cooling rates alone are not sufficient. Instead of rapid quenching, however, the magnetoelectric coupling of Cu_2OSeO_3 has been exploited to generate the metastable state. By applying an electric field of $E = 30\,\mathrm{kV\,cm^{-1}}$ with $E \parallel B \parallel \langle 111 \rangle$, the stable skyrmion lattice phase extends towards lower temperatures, covering the gap. This allows the skyrmion lattice to survive

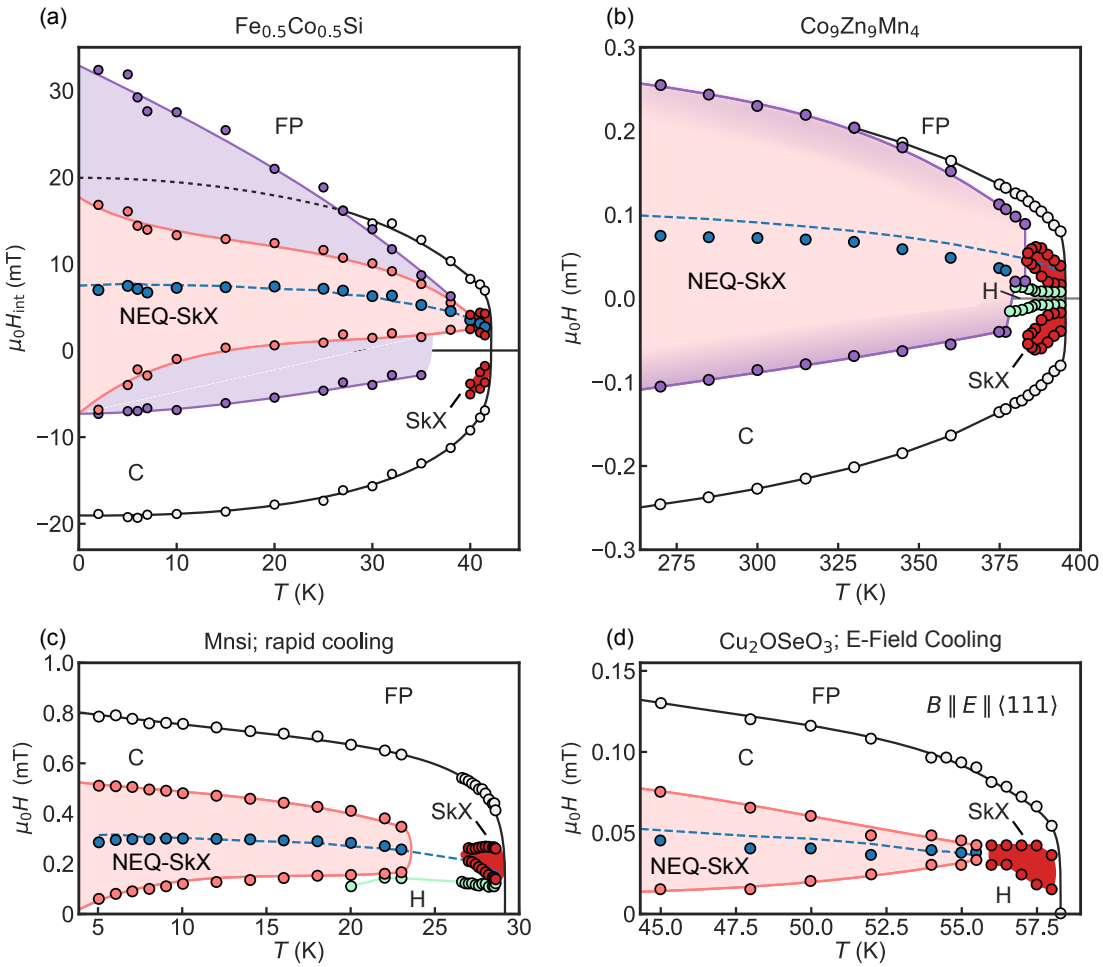

Figure 4.15: Phase diagrams hosting nonequilibrium skyrmion lattices in $Fe_{0.5}Co_{0.5}Si$ (a), $Co_9Zn_9Mn_4$ (b), MnSi (c) and Cu_2OSeO_3 (d). We distinguish helical (H), conical (C), field polarized (FP), skyrmion lattice (SkX) and nonequilibrium skyrmion lattice (NEQ-SkX) state. Light red shading indicates the nonequilibrium state. The transition region is indicated with yellow shading. Blue symbols correpond to the calculated center field $(H^*_{a2} + H^*_{a1})/2$ of the NEQ-SkX, the blue dashed line shows the theoretical value of $0.4 \cdot H_{c2}$. Data in (b)–(d) taken from [34, 91, 93]

at moderate cooling rates. As soon as the critical range is surpassed, the electric field may be removed without the metastable state disintegrating.

The phase diagram of $Fe_{0.5}Co_{0.5}Si$ is most similar to that of $Co_9Zn_9Mn_4$. Note that other definitions were used to define the phase boundaries in $Co_9Zn_9Mn_4$. The lower phase boundary is comparable to H^*_{c1} used in this work, while H^*_{a1} can not be determined, as differential susceptibility data dM/dH is not available. Analogous to $Fe_{0.5}Co_{0.5}Si$,

we expect $Co_9Zn_9Mn_4$ to be governed by a broad distribution of activation energies as well. Both materials show a metastable skyrmion lattice in zero field over a broad temperature range and in both materials, the skyrmion lattice survives at field cooling with moderate rates. This is corroborated by the non-exponential relaxation behavior reported for $Co_9Zn_9Mn_4$ at high temperatures, just below the stable skyrmion lattice phase [34].

Both, logarithmic and stretched exponential relaxation arise as an approximation of a broad distribution of activation energies [144]. The logarithmic approximation, however, implies that the thermally activated region of the barrier distribution is essentially flat. This breaks down at high temperatures, where larger regions of the barrier distribution are sampled and the finite curvature of the barrier distribution can not be neglected.

In contrast, for both MnSi and Cu_2OSeO_3 the metastable state decays completely at moderate cooling rates. Similar relaxation measurements in MnSi at temperatures just below the stable skyrmion lattice phase reveal an approximately exponential decay [91]. This suggests a narrow distribution of activation energies. In addition, rapid decay occurs once the transition lines associated with the nucleation barrier are crossed. As a result, the metastable skyrmion lattice is absent in a broad temperature region at zero field, unlike $Fe_{0.5}Co_{0.5}Si$ or $Co_9Zn_9Mn_4$. As discussed in the previous chapter, the broad distribution of activation energies is connected to the pinning of (anti-)monopoles. This is corroborated by the fact that both $Fe_{0.5}Co_{0.5}Si$ and $Co_9Zn_9Mn_4$ exhibit strong constitutional site disorder while MnSi and Cu_2OSeO_3 are relatively clean, defect free materials.

This behavior shares many similarities with glass formers and ordinary first order phase transitions, where the high temperature state can also be arrested if the cooling rate is fast enough. In strong glass formers, such as O-terphenyl, cooling at moderate rates is sufficient to arrest the high temperature state [3]. Metallic glasses, in contrast, require violent quenching of the high temperature state ($\geq 1 \times 10^6\,\mathrm{K/\,min}$). The transformation towards the low temperature state in glasses and ordinary first order phase transitions occurs via a nucleation and subsequent growth process, which may be arrested thermally if cooled fast enough and shares many similarities with the Bloch point mediated decay of skyrmion lattices [72, 74].

Note that the structural disorder of glasses is not important for this discussion. It is merely a result of the disordered nature of the arrested state, the liquid. The same concepts also apply to structural transitions between two crystalline phases.

It has been recognized that lowering the diffusivity of the atoms, e.g. by doping, decreases the critical cooling rate. The lower diffusivity essentially slows down the timescales of the formation and growth of the interfaces between high-temperature and low-temperature order[3]. Similarily the (anti-)monopoles represent the interface between a sykrmion and conventional order. Decreasing the (anti-)monopoles mobility likewise decreases the critical cooling rate.

In conclusion, once created, the metastable skyrmion states share a great amount of similarity. Differences arise especially at the phase boundaries, where disorder extends the lifetime and aids in the stabilization during the initial cooldown.

4.5 Conclusions

Skyrmions are considered one of the most promising candidates for future spintronic applications. A vast amount of research is focused on thermodynamically stable skyrmion lattices albeit metastable skyrmion states are a necessity for most applications. To date, the understanding of metastable skyrmion lattices is still lacking. Especially the stabilization of said states remains one of the most challenging tasks for the engineering of skyrmion based devices.

Motivated by the potential for future applications, we conducted a comprehensive study of the cubic chiral magnet $Fe_{0.5}Co_xSi$, hosting a nonequilibrium skyrmion lattice state. The nonequilibrium skyrmion lattice state is formed by field-cooling across the stable skyrmion lattice phase at high temperatures, using moderate cooling rates in the order of $10\,\mathrm{K\,min^{-1}}$. Using extensive magnetization and ac-susceptibility measurements, we investigated the stability of the nonequilibrium state against temperature and magnetic field. The nonequilibrium skyrmion lattice is found to survive in a broad temperature and field region of the magnetic phase diagram, consistent with previous reports [46, 90, 95, 135, 139]. The stability of the nonequilibrium state increases significantly towards low temperatures, where it extends deep into the field polarized state as well as into the negative field region. A comparison of $Fe_{0.5}Co_{0.5}Si$ with other cubic chiral magnets hosting a nonequilibrium skyrmion phase revealed a generic behavior of the nonequilibrium state. The most notable observation is that the skyrmion phase is always centered around a magnetic field value of $0.4\,H_{c2}$, which corresponds to the magnetic field where the free energy of the skyrmion phase is minimal with respect to the conical phase [37].

In addition, using time-dependent magnetization measurements, we have investigated the relaxation behavior of the nonequilibrium state. Sizable relaxation effects of the metastable state are only observed in two broadened bands in (H, T)-space at both low and high fields, confining the metastable state. Moreover, the regions of sizable relaxation are accompanied by quantitative differences between the differential susceptibility, $\mathrm{d}M/\mathrm{d}H$ calculated from the magnetization and the real part of the ac susceptibility, χ'. The relaxation is found to follow a logarithmic dependence on time, similar to magnetic viscosity in ferromagnets, and results from Arrhenius-type relaxations over a broad distribution of energy barriers. We have successfully applied, for the first time, master curve scaling to the relaxation measurements of skyrmion lattices, which allowed us to extract the distribution of activation energies. The barrier distribution is comprised of a narrow peak at $E \approx 6\,J$ associated with the topological protection, superimposed on a broad distribution, extending up to $E \approx 35\,J$. We attribute the broad distribution to pinning of monopoles, resulting in a non-equilibrium skyrmion lattice state, kinetically stabilized beyond topological protection.

In conclusion, although it has been known that defect pinning might stabilize the skyrmion lattice, the extent was quite surprising. The remarkably robust stabilization might offer an additional tuning parameter which has not yet been explored.

CHAPTER 5

Independent Skyrmion Phases and Tilted Conical Phase in Cu_2OSeO_3

In this chapter, we report a comprehensive study of the magnetic properties of single-crystal Cu_2OSeO_3. Using magnetization, ac-susceptibility, nonlinear ac-susceptibility and specific heat, we investigate the influence of crystal orientation, cooling history, and demagnetizing effects. Particular emphasis is placed on the $\langle 100 \rangle$ orientation, where recent neutron scattering experiments have identified a second skyrmion phase and a tilted conical phase.

This chapter is organized as follows. We begin the presentation of the experimental results, in Sec. 5.1.1, with a brief introduction of the designations and terminology used throughout this chapter. This is followed by a presentation of the orientation and history dependence of the magnetic phase diagram in Sec. 5.1.2. In Sec. 5.1.3, we present typical magnetization and ac-susceptibility data following ZFC and HFC and provide a direct comparison of the thermodynamic signatures with the scattering intensities observed in neutron scattering. In Sec. 5.1.4, we present the results of nonlinear harmonic ac-susceptibility measurements. In Sec. 5.1.5 we demonstrate the effects of demagnetizing fields, followed by a presentation of selected specific heat data in Sec. 5.1.6. Finally, in Sec. 5.1.7 we address the nucleation of the low-temperature skyrmion phase utilizing first-order reversal curves. We begin the discussion of the results in Sec. 5.2.1 with a comparison of typical magnetization data of MnSi, $Fe_{0.8}Co_{0.2}Si$, and Cu_2OSeO_3, illustrating the effects of cubic anisotropy. In Sec. 5.2.2, we quantitatively infer the magnetocrystalline anisotropy constant from the experimental data. In Sec. 5.2.3 we discuss the peculiar interplay of magnetocrystalline anisotropy and modulated magnetic structures. Finally, in Sec. 5.2.4 we discuss our findings with regard to the nucleation of the low-temperature skyrmion phase. We end this chapter with a conclusion in Section 5.3.

5.1 Experimental Results

5.1.1 Designations and Terminology

Apart from the trivial paramagnetic and field polarized state, the phase diagram of Cu_2OSeO_3 exhibits five modulated magnetic structures, three of which are well known. These are (i) the helical phase, (ii) the conical phase, and (iii) the high-temperature skyrmion lattice phase. In addition, as recently shown, for magnetic fields along the $\langle 100 \rangle$ direction at low temperatures two additional magnetic phases emerge, namely (iv) the tilted conical phase and (v) the low-temperature skyrmion phase.

In consequence, eight phase boundaries may be distinguished as a function of magnetic field. The designations and definitions of the phase boundaries are summarized in Table 5.1. On account of strong hysteretic effects, we further distinguish between increasing and decreasing field strength indicated by superscript u and d, respectively. As a final remark, the low-temperature skyrmion phase always emerges within the field range of the tilted conical phase. The substantial overlap of features of both phases does not allow to unambiguously identify the magnetic field, where the low-temperature skyrmion phase

Table 5.1: Definitions of the transition fields between the various magnetic phases observed as part of this study.

Field	Phase	Definition	Direction
H_{c1}^{u}, H_{c1}^{d}	Helical	Peak in dM/dH at low fields	up / down
H_{c2}^{u}, H_{c2}^{d}	Conical	Point of inflection in dM/dH at high fields	up / down
H_{a1}^{u}, H_{a1}^{d}	High-temperature skyrmion	Peak in dM/dH	up / down
H_{a2}^{u}, H_{a2}^{d}	High-temperature skyrmion	Peak in dM/dH	up / down
H_{t1}^{u}, H_{t1}^{d}	Tilted conical	point of inflection in χ'' towards low fields	up / down
H_{t2}^{u}, H_{t2}^{d}	Tilted conical	point of inflection in χ'' towards high fields	up / down
H_{s1}^{d}	Low-temperature skyrmion	peak in dM/dH at low fields	down
H_{s2}^{u}	Low-temperature skyrmion	shoulder in dM/dH at high fields	up

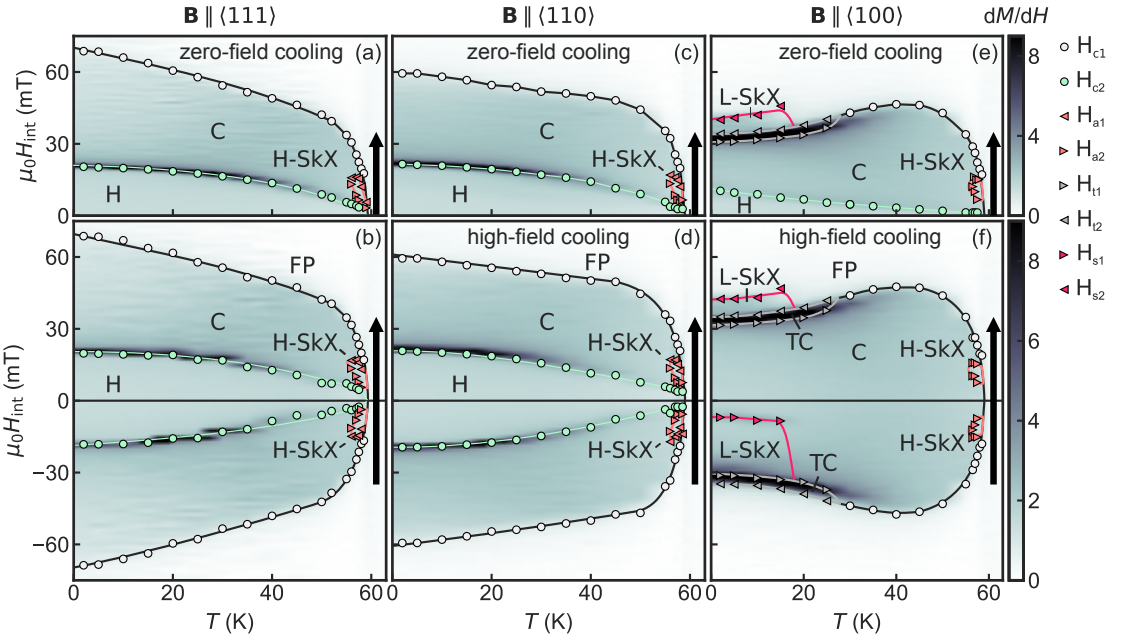

Figure 5.1: Magnetic phase diagrams extracted from magnetization and susceptibility data for fields along ⟨111⟩, ⟨110⟩ and ⟨100⟩ axis. Diagrams are shown as a function of internal field, corrected for demagnetizing fields. Phase boundaries are marked with colored symbols. We distinguish helical (H), conical (C), tilted-conical (TC), field polarized (FP), high-temperature skyrmion (H-SkX) and low-temperature skyrmion order (L-SkX). Grey colormap shows differential susceptibility data $\mathrm{d}M/\mathrm{d}H$ with dark colors corresponding to large values. Red and green shading highlights helical and skyrmion order. Data were measured in field scans following zero-field cooling (first row) and high-field cooling (second row). The sweep direction of the magnetic field is marked with a black arrow.

appears. As a result, H_{s1}^{u} and H_{s2}^{d} are not listed in Table 5.1.

5.1.2 Magnetic Phase Diagrams

Considering the complexity of the magnetic phase diagrams, hosting five modulated magnetic structures with significant hysteretic effects, it is instructive to start the presentation of the results with the magnetic phase diagrams inferred from magnetization and susceptibility data.

Fig. 5.1 presents the magnetic phase diagrams for field along all major crystallographic directions, with the ⟨111⟩, ⟨110⟩ and ⟨100⟩ orientation shown in the first, second and third row, respectively. The phase diagrams are shown as a function of internal field, corrected for demagnetizing effects. The phase diagrams have been inferred from isothermal mag-

netization and ac-susceptibility measurements. We distinguish between two measurement protocols, namely zero-field cooling (ZFC, first row) and high-field cooling (HFC, second row), with the sweep direction of the magnetic field indicated by a black arrow. The phase boundaries are marked with colored symbols. The definition of the phase boundaries is given in the following sections. A colormap of the strength of the differential susceptibility $\mathrm{d}M/\mathrm{d}H$ is shown in the background of the phase diagrams, with dark colors corresponding to large values. Both helical and skyrmion order are further highlighted with green and red shading.

The magnetic phase diagrams of the $\langle 111 \rangle$ and $\langle 110 \rangle$ orientation (Fig. 5.1(a)–(d)) resemble the generic phase diagram of the cubic chiral magnets (c.f. Sec. 2.1) with the helimagnetic groundstate, the conical state at intermediate fields, the field polarized state (FP) at high fields and the skyrmion lattice state (HS) at finite fields and high temperatures just below T_c. A steady increase of both transition lines $H_{\mathrm{c}1}$ and $H_{\mathrm{c}2}$ towards lower temperatures may be observed, with $H_{\mathrm{c}2}$ increasing slightly steeper along $\langle 111 \rangle$. Additionally, a distinct signature appears in $\mathrm{d}M/\mathrm{d}H$ at the border between helical and conical phase $H_{\mathrm{c}1}$.

The phase diagrams of the $\langle 100 \rangle$ orientation displays some similarities with the $\langle 110 \rangle$ and $\langle 111 \rangle$ orientation. The high-temperature skyrmion phase appears, consistently with the $\langle 110 \rangle$and $\langle 111 \rangle$ orientation, at finite fields and high temperatures just below the ordering temperature. Down to $T \approx 40\,\mathrm{K}$, $H_{\mathrm{c}2}$ increases monotonically. Following ZFC, a signature of the helical to conical transition $H_{\mathrm{c}1}$ may be seen that is however much weaker and shifted towards lower fields. Also, the temperature dependence is almost entirely linear in contrast to the curved temperature dependence of the $\langle 110 \rangle$ and $\langle 111 \rangle$ orientations.

In addition, there are some significant differences. Below 40 K the upper critical field $H_{\mathrm{c}2}$ starts to decrease with decreasing temperature. This is accompanied by the emergence of the tilted-conical phase below $T \approx 30\,\mathrm{K} \approx T_\mathrm{c}/2$ at the border between conical and field-polarized state. Further, with the emergence of the tilted-conical phase, a distinct signature appears in $\mathrm{d}M/\mathrm{d}H$. Signatures of the low-temperature skyrmion phase appear below $T \approx 15\,\mathrm{K} \approx T_\mathrm{c}/4$. The low-temperature skyrmion phase emerges approximately in the field range of the tilted-conical phase but extends well beyond it. The phase boundaries of the low-temperature skyrmion phase (light red circles) are highly hysteretic, but the following statements always apply: First, the tilted-conical phase always emerges first, followed by the low-temperature skyrmion phase. Second, the tilted-conical phase always disappears first, followed by the low-temperature skyrmion phase. As a result, for field scans with increasing field, the low-temperature skyrmion order extends beyond the tilted-conical phase towards higher magnetic fields and for decreasing fields beyond the tilted conical phase towards lower magnetic fields.

In conclusion, the emergence of a skyrmion lattice in the zero temperature limit clearly shows that thermal fluctuations play no major role in the formation. Instead, the existence of the low-temperature skyrmion lattice only along the $\langle 100 \rangle$ orientation identifies cubic anisotropies as a crucial driving force for stabilization. This is further supported by the anisotropies of the critical fields as compared to other cubic chiral magnets. A quantitative comparison of the critical field scales $H_{\mathrm{c}1}$ and $H_{\mathrm{c}2}$ reveals that both are the

largest along the ⟨111⟩ orientation, followed by the ⟨110⟩ orientation and smallest along the ⟨100⟩ orientation, hereby identifying ⟨100⟩ as the easy magnetic axis, consistent with the alignment of the helix propagations in zero field [49, 100].

One additional observation regarding H_{c1} may be made: Albeit clear signatures of H_{c1} appear following ZFC, they are absent following HFC which may be explained as follows. In this configuration, one easy axis is parallel to the magnetic field while the others are perpendicular to the field direction. Therefore, when the magnetic field is reduced from the conical to the helical state only the ⟨100⟩ domain parallel to the field may be populated, leading to a single domain helical state indistinguishable in the susceptibility from the conical state.

5.1.3 Experimental Data

The following section presents the experimental results of the magnetization and susceptibility measurements. The presentation is organized in three parts. First, in Sec. 5.1.3, typical data following ZFC is shown, illustrating the orientation dependence of the key features of magnetization and susceptibility. Subsequently, in Sec. 5.1.3, typical magnetization and susceptibility data following HFC are shown, demonstrating the strong hysteretic effects associated with the low-temperature skyrmion phase. Finally, a comparison of selected susceptibility data with neutron scattering data is made. This serves to justify the interpretation and definitions of the transition fields.

(a) Magnetization and Susceptibility under ZFC

Typical magnetization and susceptibility data for field along all major crystallographic orientations, ⟨111⟩ (blue), ⟨110⟩ (green) and ⟨100⟩ (red), is shown in Fig. 5.2. The data is recorded following ZFC and shown as a function of internal field, corrected for demagnetizing fields.

It is instructive to start the presentation of the experimental data at high temperatures, where the qualitative behavior is essentially isotropic. Fig. 5.2(a) presents the magnetization data at a temperature of $T = 57.5\,\mathrm{K}$, crossing the high-temperature skyrmion phase. With increasing field, the system changes, in this order, from helical, conical, skyrmion lattice, conical to the field polarized state. The magnetization increases almost linearly before approaching the saturation above $\approx 20\,\mathrm{mT}$. A slight decrease of the incline at intermediate fields signals the skyrmion phase. Such small deviations from the linear behavior, however, are best seen in the differential susceptibility, $\mathrm{d}M/\mathrm{d}H$, calculated from the magnetization, as shown in Fig. 5.2(d)–(f) (symbols).

For magnetic field aligned along all three major axes, the susceptibility exhibits three distinct maxima as a function of the increasing field. They represent, in this order, the well-known characteristic signatures of the helical to conical, the conical to high-temperature skyrmion and the high-temperature skyrmion to conical transition at H_{c1}^{up}, H_{a1}^{u} and H_{a2}^{u}, respectively. A rapid decline of the susceptibility at high fields marks the transition into the field-polarized state, with the critical field H_{c2}^{u} corresponding to the inflection point. Both the helical and the skyrmion lattice state show a reduced

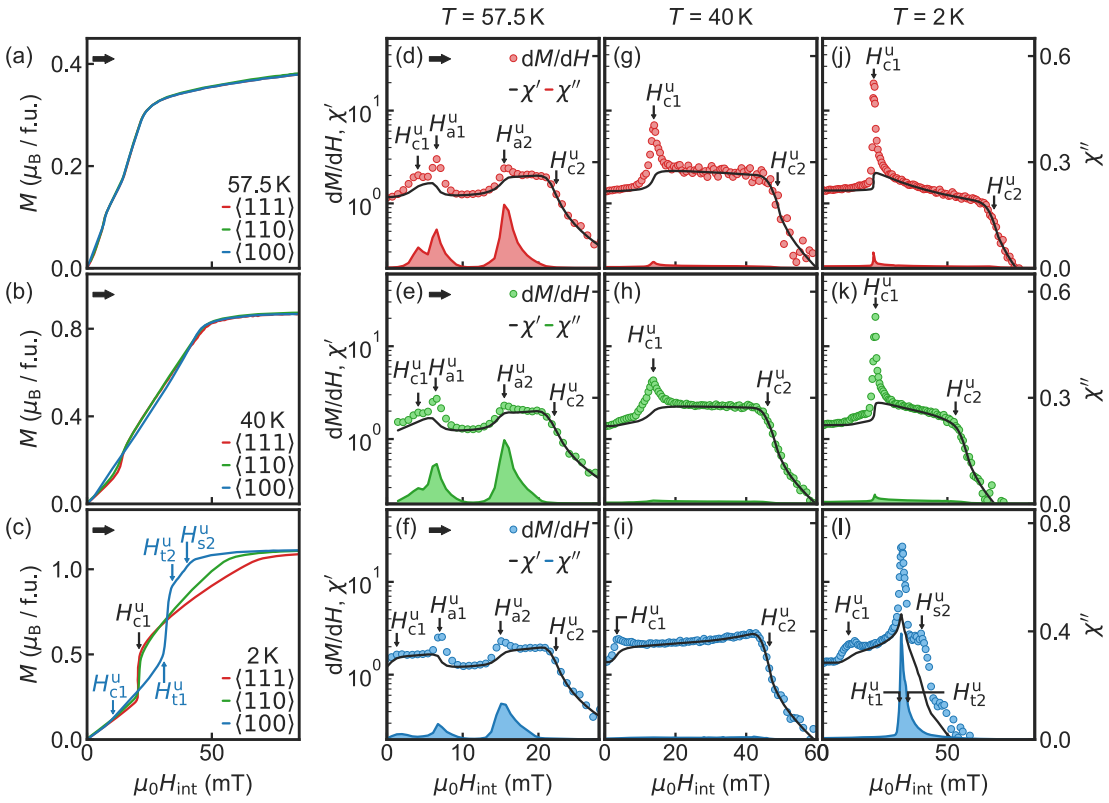

Figure 5.2: Typical magnetization and susceptibility data for field along ⟨111⟩ (red), ⟨110⟩ (green) and ⟨100⟩ (blue). Data is shown as a function of internal field, following ZFC.

susceptibility compared to the conical state.

The real and imaginary part of the ac-susceptibility, χ' and χ'', are shown as a black and a colored line. With the exception of the the transition regimes surrounding $H^{\mathrm{u}}_{\mathrm{c1}}$, $H^{\mathrm{u}}_{\mathrm{a1}}$ and $H^{\mathrm{u}}_{\mathrm{a2}}$, quantitative agreement between $\mathrm{d}M/\mathrm{d}H$ and χ' is found. In contrast, χ'' shows distinct signatures only at $H^{\mathrm{u}}_{\mathrm{c1}}$, $H^{\mathrm{u}}_{\mathrm{a1}}$ and $H_{\mathrm{a2^u}}$ but vanishes elsewhere. The differences between $\mathrm{d}M/\mathrm{d}H$ and χ' in combination with the dissipative signatures in χ'' indicate slow relaxation processes related to domain formation and reorientation processes [134–137]. Note that $H^{\mathrm{u}}_{\mathrm{c1}}$ is slightly smaller along ⟨100⟩, while $H^{\mathrm{u}}_{\mathrm{c2}}$ is essentially isotropic. Furthermore, the dissipative signal at $H^{\mathrm{u}}_{\mathrm{c1}}$ is notably smaller for ⟨100⟩ compared to the other directions.

The qualitative behavior remains isotropic at intermediate temperatures, as illustrated in Fig. 5.2(b) for a temperature of 40 K. As a function of increasing field, signatures of the helical, conical and field-polarized state are present. Apart from the missing skyrmion phase, the behavior is equivalent to the response at high temperatures, and only the field scales are increased. The corresponding susceptibility data is shown in Fig. 5.2(g)–

(i). Albeit H_{c2}^{u} is approximately equal for all orientations, H_{c1}^{u} is significantly smaller for field along $\langle 100 \rangle$. One additional observation regards the susceptibility within the conical phase. Neglecting cubic anisotropies, a constant susceptibility is expected in the conical phase. Experimentally, however, we observe a slight concave curvature along $\langle 111 \rangle$ and $\langle 110 \rangle$ and a convex curvature along $\langle 100 \rangle$. The difference in curvature shows that compared to the isotropic case, additional energy is required to magnetize along $\langle 111 \rangle$ and $\langle 110 \rangle$, while the energy requirement is reduced along $\langle 100 \rangle$.

Significant differences emerge at lower temperatures, where the behavior is highly anisotropic. Shown in Fig. 5.2(c) is the magnetization at a low temperature of 2 K. Initially, the magnetization increases with the same slope, regardless of orientation. A sizable jump of M at low fields indicates the helical to conical transition of the $\langle 111 \rangle$ and $\langle 110 \rangle$ orientation and is followed by a quasilinear increase towards saturation.

Markedly more complex behavior is seen for field along $\langle 100 \rangle$. With increasing field, M shows a tiny signature at H_{c1}^{u}, indicating the helical to conical transition, followed by an approximately linear increase up to H_{t1}^{u}. From H_{t1}^{u} to H_{t2}^{u}, M exhibits a large, almost vertical jump, followed by a quasilinear increase into saturation, with a slope comparable to low fields. This behavior is reminiscent of the helical to conical transition observed in the other directions. A comparison with neutron scattering, however, identifies these signatures with the emergence of the tilted-conical and the low-temperature skyrmion phase, as shown in a later section.

The corresponding susceptibilities are show in Fig. 5.2(j)–(l) For the $\langle 111 \rangle$ and $\langle 110 \rangle$ orientation, the behavior is qualitatively equivalent to 40 K, albeit the signatures are much more pronounced. In contrast, the $\langle 100 \rangle$ orientation shows a large peak in $\mathrm{d}M/\mathrm{d}H$ at high fields, originating from the jump-like increase in M, followed by a sizable shoulder. Both signatures are not entirely tracked by χ', suggesting relaxation effects. Surprisingly, the imaginary part of the ac-susceptibility χ'', measuring the magnetic dissipation, shows a signature only between H_{t1}^{u} and H_{t2}^{u}. The broad shoulder in $\mathrm{d}M/\mathrm{d}H$, albeit not tracked by χ', shows no dissipation. The dissipative signal, as we will show in a later section, is a key signature of the tilted conical state. As such, we use the inflection points at both sides of the dissipative signal to track the phase boundaries of the tilted conical phase, denoted as H_{t1} and H_{t2}.

Finally, it may be noted that the susceptibility in the conical phase is much more curved than at higher temperatures, suggesting an increase in strength of the cubic anisotropy at low temperatures.

(b) Magnetization and Susceptibility under HFC

We now focus on the experimental data following HFC. This serves to demonstrate the hysteretic effects that are particularly pronounced for the low-temperature skyrmion phase. Fig. 5.3(a) presents magnetization data following HFC of all major crystallographic orientations. The corresponding susceptibilities are shown in Fig. 5.3(c)–(e). The data is recorded at 2 K and shown as a function of internal field, corrected for demagnetizing fields. The magnetic field is swept from negative fields to positive fields, as indicated by an arrow. Thus, data in negative fields demonstrates the behavior with decreasing

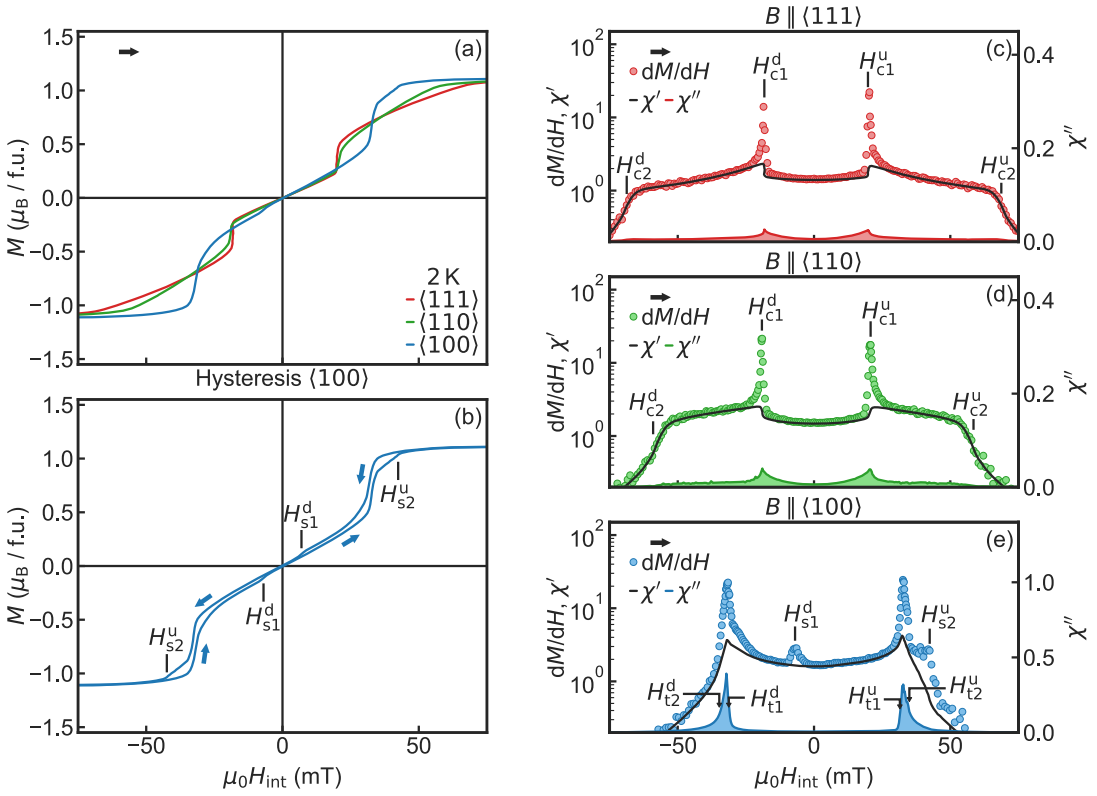

Figure 5.3: Typical magnetization and susceptibility data for field along ⟨111⟩ (blue), ⟨110⟩ (green) and ⟨100⟩ (red). Data is shown as a function of internal field, following HFC.

field strength, whereas data in positive fields displays the behavior with increasing field strength.

It is instructive to start the presentation with the magnetization data of the ⟨111⟩ and ⟨110⟩ orientation, which shows, in essence, the behavior following ZFC. The observations may be summarized as follows: First, the magnetization is almost perfectly point-symmetric with respect to the origin. Second, the experimental data displays signatures characteristic of helical order at low fields, conical order at intermediate fields and of the field polarized state at high fields, reminiscent of the familiar behavior of the chiral magnets. Sizable, step-like changes of M signal the helical to conical transition at H_{c1} and result in distinct maxima of $\mathrm{d}M/\mathrm{d}H$. Third, on closer inspection, minor hysteresis may be observed at H_{c1}, yet no hysteresis is seen at H_{c2}, as expected.

Unlike the ⟨111⟩ and ⟨110⟩ orientation, the behavior of the ⟨100⟩ direction is notably asymmetric. Starting at large negative fields, as a function of decreasing field transitions from field polarized state across tilted-conical state to the low-temperature skyrmion state and finally into the conical state are seen. The respective transition fields are marked as

H_{t2}^{d}, H_{t1}^{d} and H_{s1}^{d}. With a further increase of field towards positive fields one observes transitions from conical state into the tilted-conical state followed by the low-temperature skyrmion state and finally the field-polarized state, marked as H_{t1}^{u}, H_{t2}^{u} and H_{s2}^{u}. This resembles the behavior following ZFC, except for the missing helical phase at low fields. At both H_{s1}^{d} and H_{s2}^{u}, the distinct signatures in $\mathrm{d}M/\mathrm{d}H$ are not tracked in χ' and no dissipative signal in χ'' is seen. Additionally, the phase boundaries of the tilted conical phase show no noticeable hysteresis.

It is worth pointing out that independent of increasing or decreasing field, clear signatures are only seen when leaving the low-temperature skyrmion lattice. Entering the low-temperature skyrmion lattice occurs within the tilted conical phase. As such, the features of both phases overlap. This issue will be addressed in a later section using FORC measurements.

The pronounced asymmetry is further emphasized in Fig. 5.3(b), showing a full hysteresis loop. Sizable hysteretic effects between increasing and decreasing fields are observed in the field range from H_{s1} to H_{s2}. With a reduction in field, the magnetization remains longer in the saturated state, due to the absence of the low-temperature skyrmion phase. Once the tilted-conical phase is crossed, the magnetization remains at an elevated level down to H_{s1}^{d}. In contrast, with increasing field, the skyrmion phase appears above the tilted conical phase, and the magnetization remains longer at a reduced value. Thus, independent of the field direction, the tilted conical phase appears first, while the low-temperature skyrmion phase vanishes last.

(c) Comparison with Small-Angle Neutron Scattering

The definition of the phase boundaries based on feature tracking may be justified by comparison with neutron scattering data. Small-angle neutron scattering (SANS) probes the magnetic structure in reciprocal space. Accordingly, the measured intensity patterns reflect the symmetry and periodicity of the magnetic structure.

A comparison of the SANS data with corresponding susceptibility data is given in Fig. 5.4. The SANS data originate from the study reported in Ref.[119] and were provided by Alfonso Chacon. A quantitative comparison of the individual intensity profiles is not possible since the scattering intensities are not rocked. For further technical details, we refer to Ref.[119]. Great care was taken to allow for a direct comparison. Since the neutron study was conducted on a spherical sample with a demagnetizing factor of $N = 1/3$, a cuboid sample with a comparable demagnetizing factor has been chosen in the magnetization and susceptibility study, namely VTG1-19 (c.f. Sec. 3.1). Data are shown as a function of internal field, further eliminating the effects of sample shape. Due to the lack of magnetization data of the spherical sample, the magnetization correction has been calculated from a different sample, namely VTG1-19 (c.f. Sec. 3.1), using the following procedure: Starting from the magnetization curve of the reference sample as a function of applied field, the demagnetization correction is applied, yielding the magnetization as a function of internal field. Next, the demagnetization correction is inverted, using the demagnetizing factor of the sphere ($N = 1/3$) yielding, again, the magnetization curve as a function of applied field. As a result, we obtain a mapping from the external field

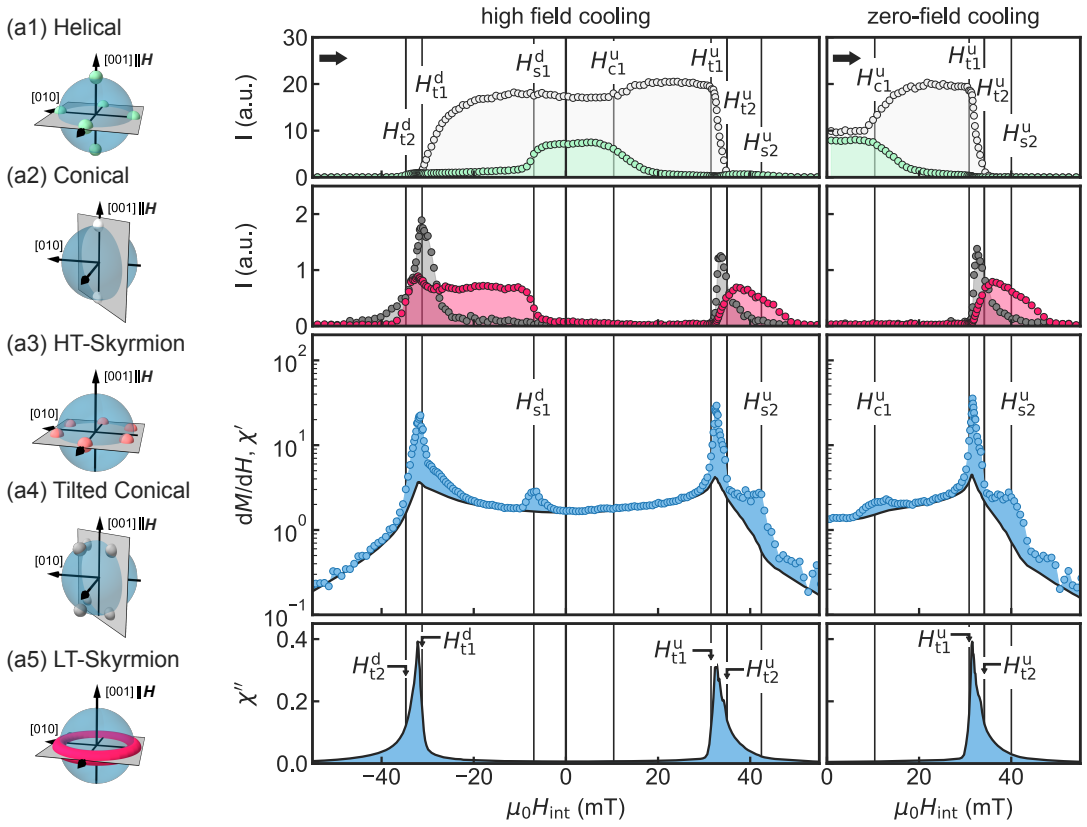

Figure 5.4: Susceptibilities and SANS intensities as a function of internal field following HFC (left column) and ZFC (right column). Schematics of the modulated SANS intensities are shown on the left side.

scale used in the SANS study to the internal field scale.

Schematics of the intensity patterns in reciprocal space, characterizing the five modulated magnetic structures of Cu_2OSeO_3, are shown in Fig.5.4(a1)–(a5). Small colored spheres illustrate the location of scattering intensity in reciprocal space. The scattering intensities are located on the surface of a sphere, shown in blue shading, with a characteristic radius $|Q| \approx D/J$, resulting in first approximation from the competition between exchange interaction J and Dzyaloshinskii-Moriya interaction D. The crystallographic (100) orientations are visualized as black arrows. The detection plane, probed by the SANS experiment, is illustrated as a grey rectangle. The five different intensity patterns shown correspond to the well-established intensity patterns of the helical (green), conical (grey) and high-temperature skyrmion (light red) state as well as the recently discovered tilted conical (dark grey) and low-temperature skyrmion state (dark red). In this context, it is important to note the different orientations of the applied magnetic field and the detection plane with respect to the crystallographic orientations. For a thorough explanation of the scattering intensities, please refer to Sec. 2.7.

Shown in Fig. 5.4(b1)–(b4) is a comparison of SANS intensities associated with the modulated magnetic structures and magnetic susceptibility data inferred within this thesis. The data is shown as a function of internal field following HFC (left column) and ZFC (right column) at a temperature of 2 K. The color coding used for the SANS intensities corresponds to the colors used in the schematics.

When decreasing the magnetic field after HFC, scattering intensity of the tilted-conical phase emerges simultaneously with the large dissipation signal in χ'' and a large peak in $\mathrm{d}M/\mathrm{d}H$, spanning a comparable field range. The upper phase boundary of the tilted conical phase H_{t2}^{d}, defined as a point of inflection in χ'' is in excellent agreement with a point of inflection in the SANS intensity. In contrast, the lower phase boundary, H_{t2}^{d}, matches the peak of the intensity instead of the point of inflection towards low fields. One may speculate if this is a result of slight imperfections in the demagnetization correction, which is particularly sensitive in this field range due to the nearly vertical increase of M.

The scattering intensity of the low-temperature skyrmion phase emerges in between H_{t2}^{d} and H_{t1}^{d} and extends far beyond the phase boundaries of the tilted conical state, towards low magnetic fields. The emergence of the low-temperature skyrmion phase may not unambiguously be associated with any signature in the susceptibilities, as signatures in $\mathrm{d}M/\mathrm{d}H$ tracking both tilted-conical and low-temperature skyrmion phase overlap. On disappearing, however, a distinct peak in $\mathrm{d}M/\mathrm{d}H$ emerges, marked as H_{s1}^{d}, without signatures in the ac-susceptibility.

With a successive increase in magnetic field, scattering intensity of the tilted-conical phase emerges again simultaneously with the large dissipation signal in χ'' and a significant peak in $\mathrm{d}M/\mathrm{d}H$, spanning a comparable field range from H_{t1}^{u} to H_{t2}^{u}. Similarly, the intensity of the low-temperature skyrmion phase emerges within the field range of the tilted conical state. With a further increase in magnetic field, the intensity of the low-temperature skyrmion lattice extends beyond the tilted conical phase towards higher fields, correlating with a sizable shoulder in $\mathrm{d}M/\mathrm{d}H$. The edge of the shoulder, marked as H_{s2}^{u} precisely corresponds to the point of inflection of the scattering intensity.

In general, the behavior observed after ZFC is equivalent to the response at increasing fields following HFC. One notable difference, however, is the observation of a helical phase at low fields in both studies Following ZFC, a small peak, denoted as H_{c1}^{u} appears in $\mathrm{d}M/\mathrm{d}H$ at the transition from helical to conical state and corresponds precisely with the point of inflection in the helical intensity.

As a final remark, following HFC, helical intensity is seen in the SANS study whereas signatures of the helical state are absent in both magnetization and susceptibility. A small misalignment of the sample during the SANS study may explain this inconsistency and is corroborated by the observation of a similar helical signature following HFC in the magnetization data when a small misalignment was present (not shown).

5.1.4 Higher Harmonics of the AC Susceptibility

A detailed introduction of higher harmonics may be found in Sec. 3.2.3.

Shown in Fig. 5.5 are the fundamental, second and third harmonic of the ac-susceptibility at typical temperatures following HFC. Data are shown as a function of internal magnetic field with field along ⟨110⟩ (green, (a)–(f)) and ⟨100⟩ (blue, (g)–(l)). Here, rows correspond to fundamental, second and third harmonic whereas columns correspond to different temperatures.

We begin the presentation with field along ⟨110⟩ at a temperature of 2 K. Note that only the positive half is shown, as the behavior at negative fields is equivalent. In this context, we observe, with respect to the origin, a point symmetry for the even and mirror symmetry for the odd harmonics of the susceptibility. The susceptibility at the fundamental frequency, as shown in Fig. 5.5, shows the well-known behavior as reported in previous chapters. At low fields, the helical phase reveals itself as a dip in the susceptibility, followed by the conical phase between H_{c1} and H_{c2} and the field polarized state at high fields, above H_{c2}. The second harmonics χ_2' and χ_2'', as shown in Fig. 5.5(b), vanish over the complete field range, except for a tiny positive peak in χ_2' at H_{c2}. Note that this signature appears without the emergence of a dissipative signal in χ''. Similarly, the third harmonics χ_3' and χ_3'' vanish over the complete field range.

Additional signatures appear at high temperatures, when the system crosses through the high-temperature skyrmion phase, as shown in Fig. 5.5(d)–(f) for a temperature of 57.5 K. Shown in Fig. 5.5(d)–(f) are fundamental, second and third harmonics at a temperature of 57.5 K. At the phase boundaries of the high-temperature skyrmion phase, H_{a1} and H_{a2}, two additional small peaks emerge in the second harmonic, χ_2', while the third harmonic remains negligible.

Similarly, at the same temperature of 57.5 K and field along ⟨100⟩ we observe qualitatively equivalent behavior. We observe sizable peaks at H_{a1}, H_{a2} and H_{c2} in the second harmonic χ_2' and vanishing third harmonics. The signatures appear for both increasing and decreasing field strength with a comparable size and shape. Further, the second harmonic exhibits a point symmetry with respect to the origin.

In contrast, at low temperatures notably different signatures arise. At 2 K, as shown in Fig. 5.5(j), the linear susceptibility exhibits a strong peak in χ' at the border of the field polarized state, accompanied by a sizable dissipative signal in χ''. We note that the ac-susceptibility shows no signatures of the low-temperature skyrmion phase.

The corresponding second harmonics, shown in Fig. 5.5(k), display a prominent peak in the field range of the tilted conical phase for both increasing and decreasing fields. The real part of the second harmonic, χ_2', is approximately twice as large as the imaginary part, χ_2''. Compared to the signature at H_{c2}, as observed for 57.5 K, for example, the signal is significantly stronger and has the opposite sign. Similarly, both χ_3' and χ_3'' show a clear peak in the field range of the tilted-conical phase. The real part of the third harmonic, χ_3', is approximately three times as large as the imaginary part, χ_3'', and extends significantly further into the high-field region. Moreover, the third harmonics show a strong asymmetry with respect to the origin, not present for the second harmonic. The signatures with decreasing field strength (negative fields) are almost twice as a large compared to increasing fields (positive fields).

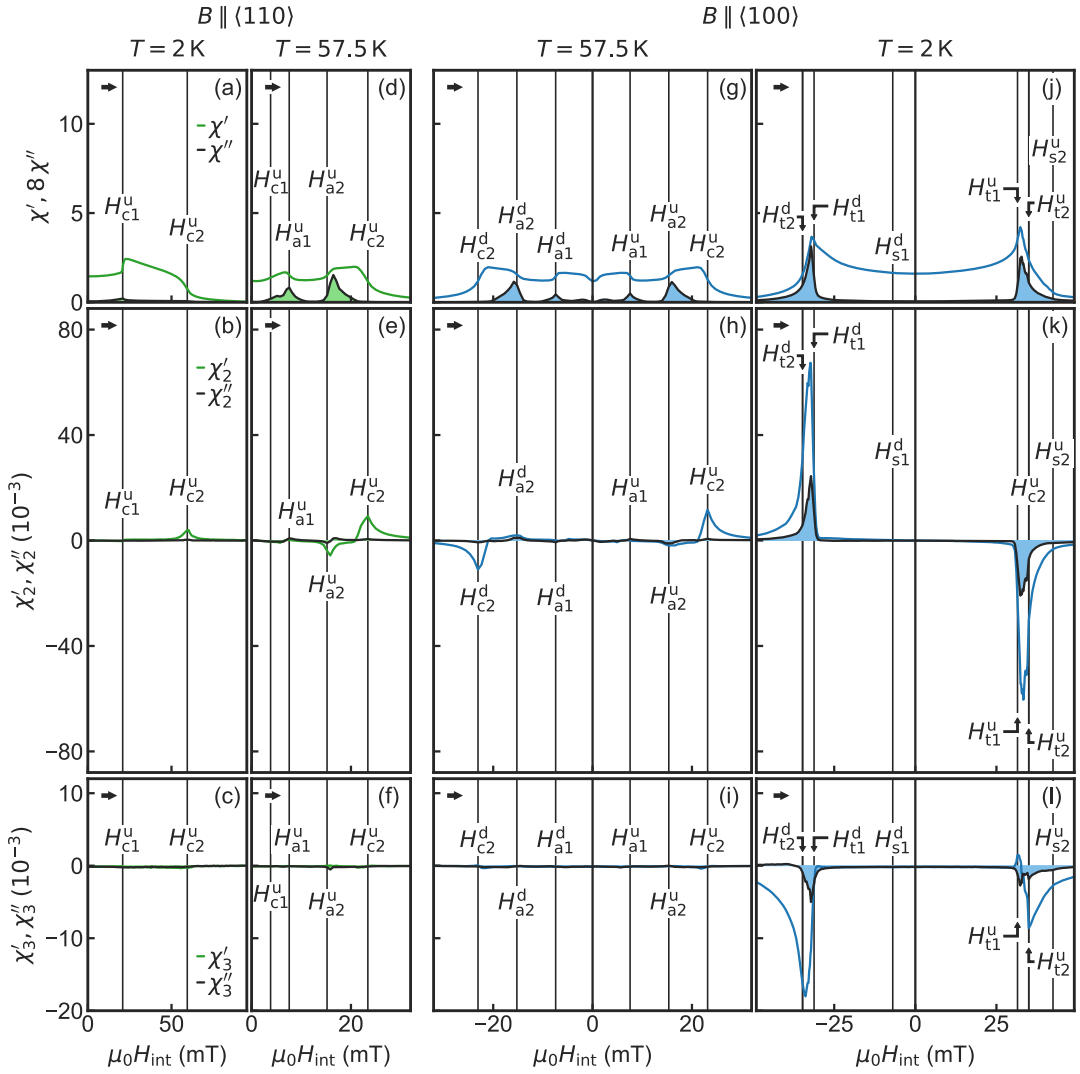

Figure 5.5: Nonlinear harmonic susceptibility as a function of field at 2 K and 57.5 K. Data is recorded following HFC with $H \parallel \langle 110 \rangle$ (green, (a)–(f)) and $H \parallel \langle 100 \rangle$ (blue, (g)–(l)). Fundamental, second and third harmonics of the ac-susceptibility are shown in the first, second and third row, respectively. The sweep direction is marked with an arrow. Note that only the positive fields are shown for the $\langle 110 \rangle$ orientation. Analogous behavior is observed at negative fields.

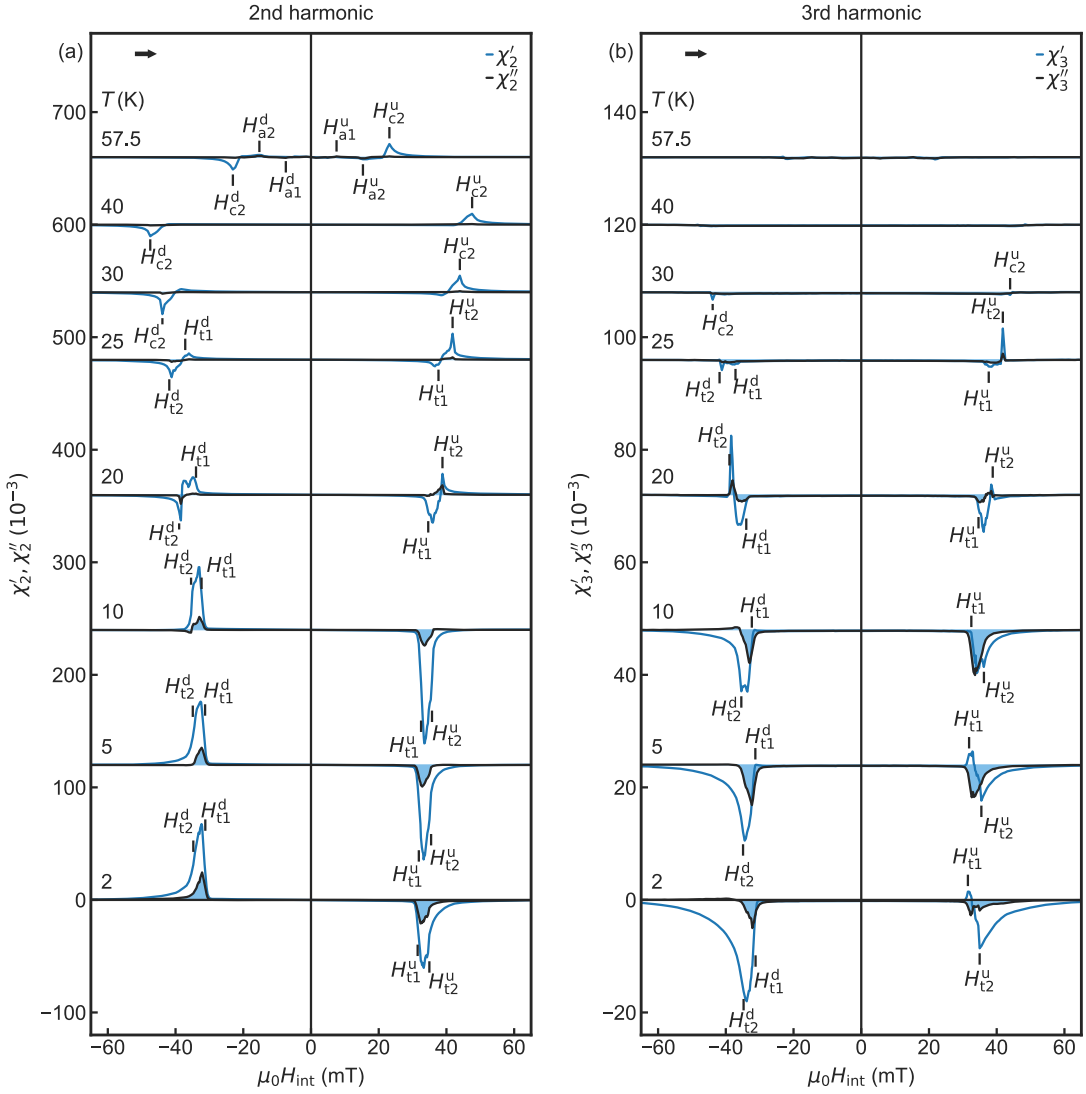

Figure 5.6: Nonlinear harmonic susceptibility as a function of field at various temperatures. Second (a) and third (b) harmonics of the ac-susceptibility for selected temperatures Data is recorded as a function of field following HFC with $B \parallel \langle 100 \rangle$. For clarity, χ_2' and χ_2'' are shifted by 120×10^{-3} for $T \leq 25\,\mathrm{K}$ and 60×10^{-3} for $T > 25\,\mathrm{K}$. χ_3' and χ_3'' are shifted by 24×10^{-3} for $T \leq 25\,\mathrm{K}$ and 12×10^{-3} for $T > 25\,\mathrm{K}$.

The evolution with temperature of the unusual higher harmonics as seen the ⟨100⟩ orientation is illustrated in Fig. 5.6. Data are shown as a function of internal field following HFC. Overall, the large signatures observed at low temperatures in both second and third harmonics develop smoothly with increasing temperature and vanish at approximately 30 K, consistent with the temperature regime of the tilted conical phase.

On closer inspection, the real part of the second harmonic, χ_2', becomes notably asymmetric from 2 K to 10 K as the peak at positive fields gains in size. At 20 K, an additional sharp peak, opposite in sign, emerges at the outer edge of the low-temperature signature towards high fields. With a further increase in temperature, it evolves into the signature characteristic of H_{c2}. Additionally, at 20 K, the low-temperature signature reveals a double peak structure at negative fields.

In comparison, the real part of the third harmonic, χ_3', as shown in Fig.5.6(b) decreases notably in size from 2 K to 10 K, while the the imaginary part, χ_3'', increases. Similarly to the second harmonic, a sharp signature emerges at 20 K at the outer edge, opposite in sign. With a further increase in temperature, however, the third harmonic vanishes at approximately 30 K unlike the second harmonic, which shows a signature at H_{c2}.

In summary, the strong higher harmonics are clearly connected to tilted conical phase, with strong correlations in both temperature and field regime. As such, they only emerge in the ⟨100⟩ orientation. Further, they sensitively depend on the field history, resulting in asymmetry between increasing and decreasing fields. In literature, the emergence of nonlinear susceptibility is reported in vortex matter, spin glasses and in particular magnetic systems, where it is connected to domain wall dynamics. Still, the origin of the harmonics in Cu_2OSeO_3 remains unknown.

5.1.5 Demagnetizing Effects

Finite samples are subject to demagnetizing effects that arise from the magnetic H-field generated by the magnetization of the sample itself. The dipolar demagnetizing field generated within the sample opposes the applied field, thereby reducing the total internal field. As a function of applied field, the magnetization appears sheared towards larger fields. In modulated magnetic structures additional, more subtle effects arise and demagnetizing effects may stabilize or destabilize certain magnetic structures[145–148]. As for Cu_2OSeO_3, theoretical calculations have revealed that dipolar interactions play an important role for the details of the magnetic phase diagram.

The effects of demagnetization on magnetization and susceptibility are illustrated in Fig. 5.7. The data is shown as a function of applied field for both increasing (red) and decreasing (blue) magnetic field. All data is recorded at a temperature of 2 K following HFC and field along ⟨100⟩. The data is organized in columns with the demagnetizing factor increasing from left to right, further indicated above each column.

Starting with a low demagnetizing factor of $N = 0.07$, as shown in Fig. 5.7(a)–(e), we observe all previously discussed signatures, in particular the hysteresis in M, associated with the low-temperature skyrmion phase and the pronounced dissipation signature of the tilted-conical phase. With increasing demagnetizing factor the steep incline of magnetization within the tilted conical phase diminishes. This is accompanied by a

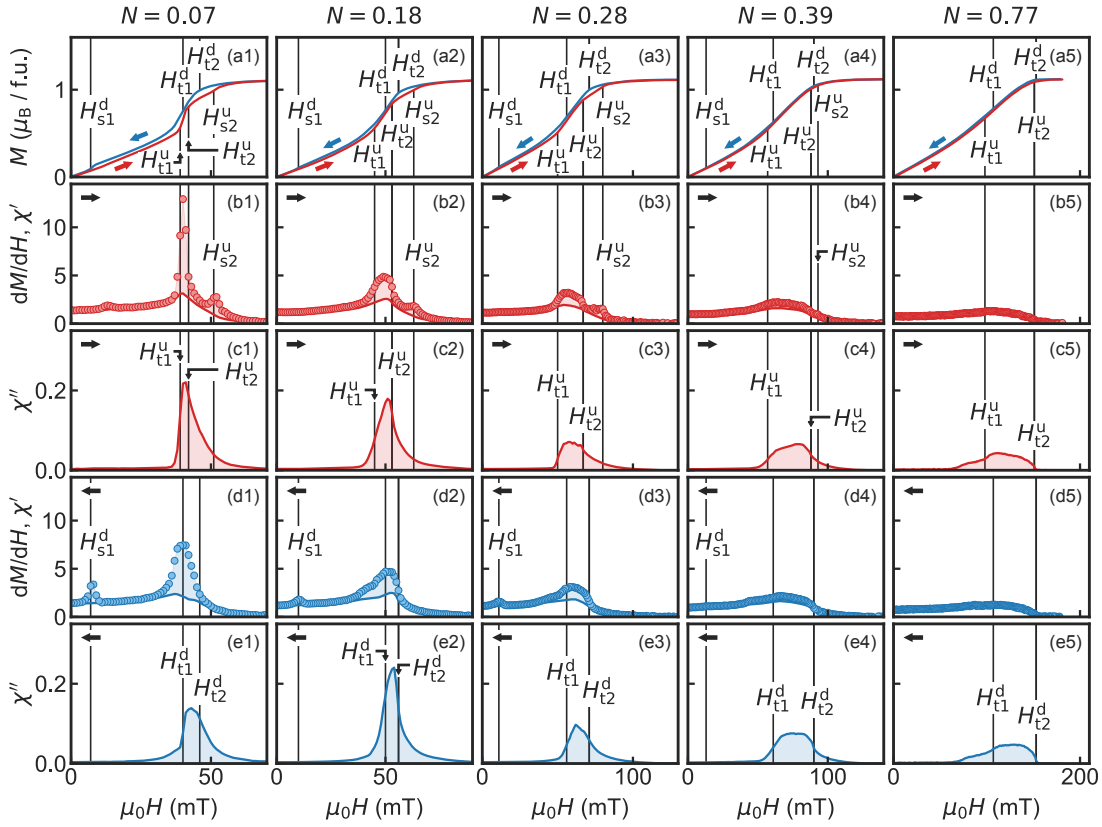

Figure 5.7: Effects of demagnetization on magnetization and susceptibility for various demagnetizing factors. All data is recorded at a temperature of 2 K following HFC and field along ⟨100⟩. Data is shown as a function of applied field for both increasing (red) and decreasing (blue) magnetic field.

drastic increase in the associated field scale and a smearing of the signatures with N. Nonetheless, a dissipation signal characteristic of the tilted conical phase is observed up to $N = .77$, the largest demagnetizing factor investigated. In contrast, the signatures of the low-temperature skyrmion phase may no longer be seen at a large demagnetizing factor of $N = 0.39$ and above. The absence of traceable signatures does not rule out the existence of skyrmions and may solely result from the smearing of the signatures. In particular, the non-ellipsoidal sample shape leads gives rise to a non-uniform distribution of the demagnetizing field that is particularly pronounced at large demagnetizing fields and may further broaden the signatures. Without additional microscopic information, however, it is not possible to gain further insights into the low-temperature skyrmion state at large demagnetizing factors.

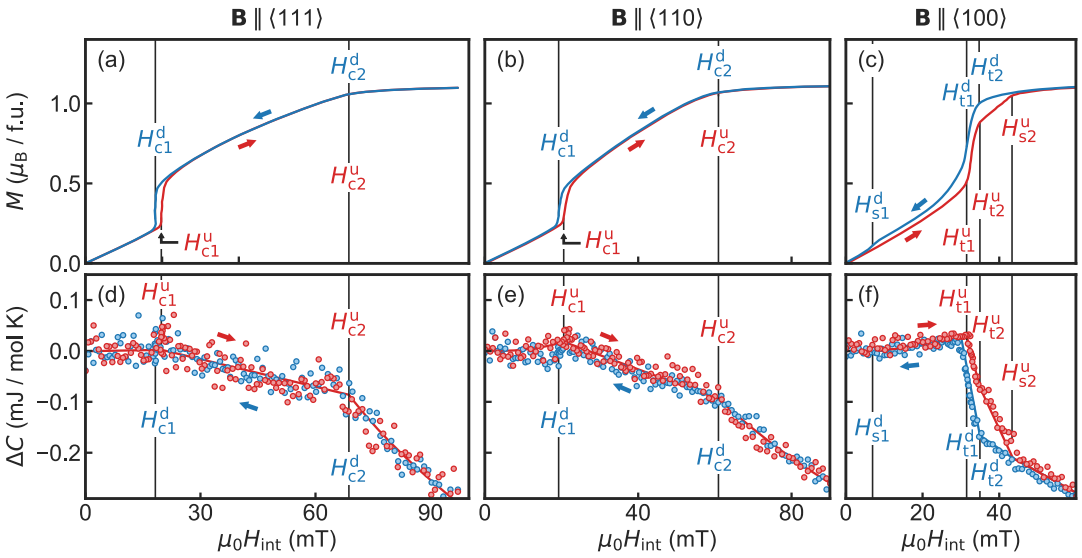

Figure 5.8: Magnetization (first row) and specific heat (second row) as a function of internal field at 2 K for all major directions. Data were measured in a single field sweep from positive to negative fields with data at negative fields mirrored back into the first quadrant. Data measured with increasing field is shown in blue, with decreasing field in orange. Colored shading of the background indicates the magnetic phases. We distinguish helical (green), conical (grey), tilted conical (dark grey), low-temperature skyrmion (red) and field-polarized (white) state. Zero field value of C has been subtracted.

5.1.6 Specific Heat

At low temperatures the specific heat mainly explores the magnetic structure and as such may allow us to gain further insights. Given the nearly horizontal course of the phase boundaries in B-T space as well as the pronounced signatures as a function of field, we have opted for isothermal field dependent specific heat measurements.

Shown in Fig. 5.8 is a comparison of quasi-isothermal magnetization, M, and specific heat, C, as a function of internal field for field along ⟨111⟩ (first column), ⟨110⟩ (second column) , and ⟨100⟩ (third column). All data was measured at a temperature of 2 K in a single field scan following HFC, with data in negative fields mirrored back to positive fields. We distinguish between increasing (red) and decreasing (blue) magnetic field strength, indicated by colored arrows. Magnetization and respective specific heat were measured on the same sample for each orientation. The specific heat values shown represent an average of at least 15 successive measurements for each field value. A tiny heat pulse of a few percents has been used .Further, a value of $C_0 \approx 13.2\,\mathrm{mJ\,mol^{-1}\,K^{-1}}$ has been subtracted from the specific heat data, representing the specific heat in zero fields.

Comparable behavior is observed for both ⟨111⟩ and ⟨110⟩ orientation, as shown in Fig. 5.8(a), (b) and Fig. 5.8 (c), (d), respectively. The magnetization, as previously

shown, shows the familiar behavior with the helical phase at low magnetic fields, followed by the conical phase and the field-polarized phase at high fields. The transition fields are marked as H_{c1} and H_{c2}, respectively. At H_{c1}, a tiny hysteresis may be observed. Similarly, the specific heat of both orientations displays three regions of distinct slopes, which may be attributed to the helical, conical and field polarized state. The transition fields agree exceptionally well with the magnetization data. In the helical phase, the specific heat remains approximately constant as a function of field but declines linearly within the conical phase and even more steeply within the field polarized state. The same behavior is observed between increasing, and decreasing fields and hysteresis at H_{c1} as seen in the magnetization may not be resolved.

With field along $\langle 100 \rangle$ as shown in Fig. 5.8(e), (f), we observe a notably different behavior, both in comparison with the other orientations and between increasing and decreasing field. With increasing field (red), three distinct kinks are clearly visible in the specific heat, associated with the critical fields H_{t1}^{u}, H_{t2}^{u} and H_{s2}^{u}, respectively. At low fields, below H_{t1}^{u}, the specific heat is essentially constant, similar to the low field behavior of the other directions. Note that unlike the $\langle 110 \rangle$ and $\langle 111 \rangle$ orientations, the constant range corresponds to the conical and not the helical state. At H_{t1}^{u}, the specific heat drops rapidly and exhibits a step-like behavior similar to the magnetization albeit in the opposite direction. From H_{t1}^{u} to H_{t1}^{u}, the specific heat drops sharply, coinciding with a steep increase in the magnetization. From H_{t2}^{u} up to H_{s2}^{u} the rate of change, $\mathrm{d}C/\mathrm{d}H$, reduces significantly, concurrent with a reduction in susceptibility $\mathrm{d}M/\mathrm{d}H$. Moreover, above H_{s2}^{u} both dC/dH and $\mathrm{d}M/\mathrm{d}H$ are reduced once again. In contrast, under decreasing fields only two distinct kinks may be seen, associated with H_{t1}^{d} and H_{t2}^{d}. This gives rise to sizable hysteresis in the field range from H_{t1}^{u} to H_{s2}^{u}. However, no signature of the low field phase boundary, H_{s1}^{d}, of the low-temperature skyrmion lattice is seen. Being already a subtle effect in the magnetization, this is most likely a sensitivity issue.

In conclusion, only tiny differences in entropy are to be expected between the various magnetic states, arising as a function of field. Nonetheless, we have successfully determined the field dependence of the specific heat along all major crystallographic orientations. We observe suppression of the specific heat as a function of the field, which may be attributed to a reduction of entropy. Furthermore, the specific field dependence exhibits characteristics of the individual phases, in particular, the low-temperature skyrmion and tilted conical phase, which are consistent with magnetization and susceptibility.

5.1.7 First-Order Reversal Curves

In standard magnetization and susceptibility measurements, the entry into the low-temperature skyrmion phase may not unambiguously be determined, as the field region coincides with the tilted conical phase. Only the signatures when leaving the low-temperature skyrmion phase, H_{s1}^{d} and H_{s2}^{u}, are clearly visible. By using first-order reversal curves, however, we are able to determine the entry into the low-temperature skyrmion phase accurately.

The FORC protocol, as described in detail in Sec. 3.2.4, may be summarized as follows.

Starting in the saturated state in positive fields, the magnetic field is lowered to the reversal field, B_{rev}. Subsequently, data is taken while increasing the magnetic field back towards the saturated state in positive fields. Repeating this process for various reversal fields allows us to identify irreversible behavior.

Shown in Fig. 5.9(a) are magnetization curves, recorded following the FORC protocol. All data is measured at a temperature of 2 K with the magnetic field along the $\langle 100 \rangle$ orientation and various reversal fields. For clarity a major hysteresis loop is plotted as a black line, outlining the FORC data. In the field range from H_{s1}^{d} to H_{s2}^{u}, at both positive and negative fields strong irreversibilities are evident. This is further illustrated in Fig. 5.9(b), showing an enlarged view of the irreversible region in positive fields. With a reduction in reversal field, the magnetization initially tracks the descending branch of the major hysteresis loop. On entering the field region of the tilted-conical phase, however, the magnetization curve decreases and evolves towards the lower-lying ascending branch of the major loop, which indicates the nucleation of skyrmions.

To better understand the influence of the reversal field it proves helpful to examine the susceptibilities instead of the magnetization. Therefore, the corresponding differential susceptibility, $\mathrm{d}M/\mathrm{d}H$, calculated from the magnetization as well as the real-part of the ac-susceptibility, χ' are shown in Fig. 5.10(a). In view of the divergent behavior of $\mathrm{d}M/\mathrm{d}H$ in the tilted-conical phase, the logarithm of $\mathrm{d}M/\mathrm{d}H$ and χ' is shown. The imaginary part of the ac-susceptibility, χ'', is shown in Fig. 5.10(b) and serves as an indicator of the tilted conical phase. In the following, it will become clear that signatures of the low-temperature skyrmion phase appear once the tilted conical phase is entered.

With a reduction of the reversal field B_{r}, initially no difference between $\mathrm{d}M/\mathrm{d}H$ and χ' is observed. As soon as the reversal field is lowered into the field range of the tilted-conical, however, clear differences between $\mathrm{d}M/\mathrm{d}H$ and χ' emerge. This is achieved for the first time at a reversal field of $B_{\mathrm{r}} = 65\,\mathrm{mT}$. Here, dissipative signatures appear in χ'', indicating the tilted conical phase. In addition, a signature of the low-temperature skyrmion phase emerges towards high fields, marked as H_{s2}^{u}. With a further reduction of B_{r}, the signatures of the low-temperature skyrmion phase become more pronounced at first and subsequently remain unchanged.

Until the reversal field reaches the field range of the tilted conical phase at negative fields, a virtually unchanged behavior is observed. At a reversal field of $B_{\mathrm{r}} = 55\,\mathrm{mT}$ first signatures of the low-temperature skyrmion phase appear towards low fields, marked as H_{s1}^{d}. Simultaneously, a dissipative signature emerges at negative fields, indicating the tilted-conical phase.

In conclusion, this behavior unambiguously demonstrates that the low-temperature skyrmion lattice nucleates only within the tilted conical phase.

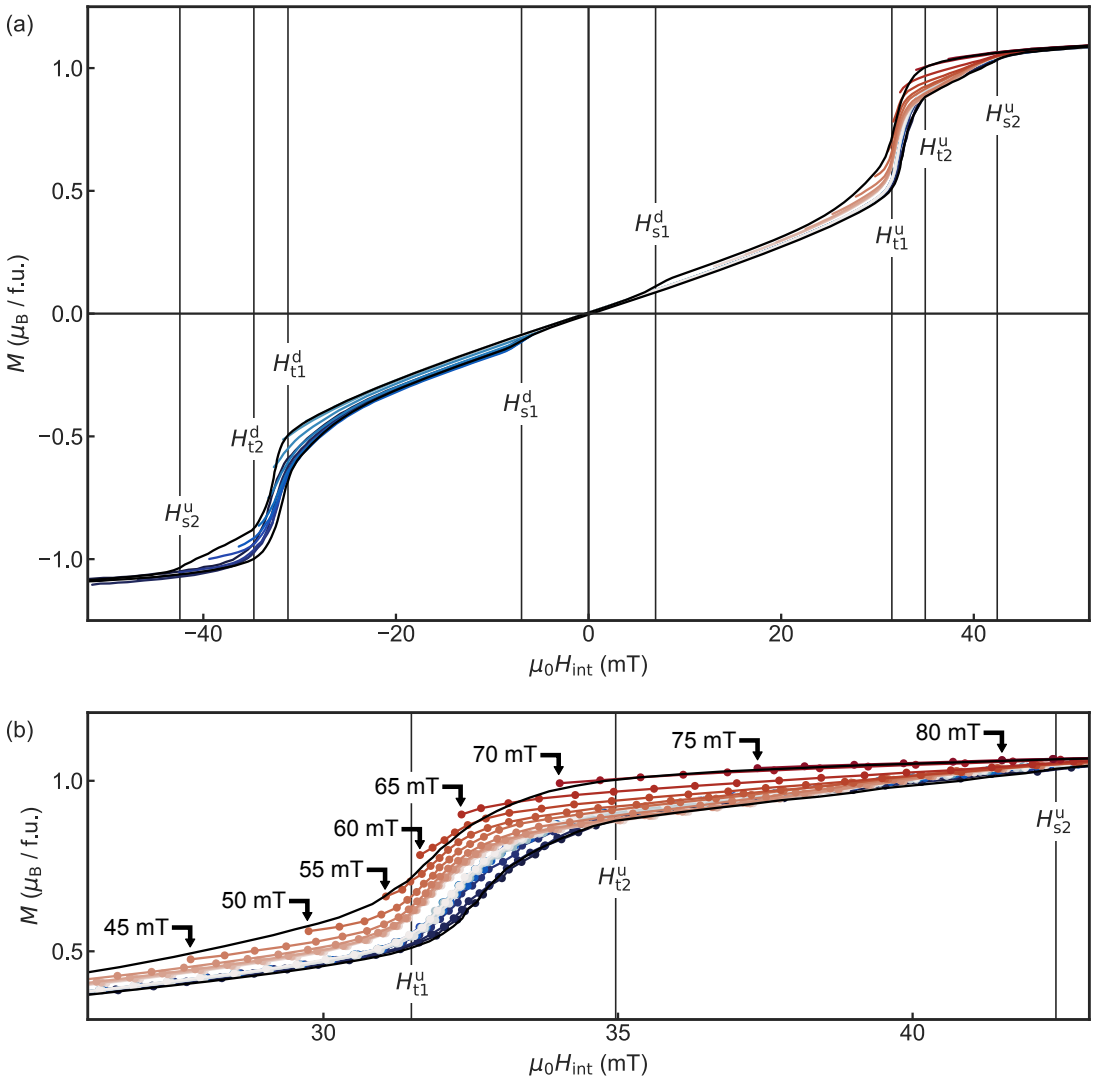

Figure 5.9: First order reversal curves of the magnetization at a temperature of 2 K with field along ⟨100⟩. The black outline shows a conventional hysteresis loop. From the saturated state at positive fields, the field is reduced to a reversal field, B_{rev}. Subsequently, data is taken while increasing the field back towards the saturated state at positive fields. Irreversible behavior is seen in the field range of the low-temperature skyrmion phase in between H_{s1} and H_{s2} at both positive and negative fields. (b) Enlarged view of the irreversible region at positive fields. The reversal field of each trace is marked with an arrow. Note that the reversal field is given in units of applied field.

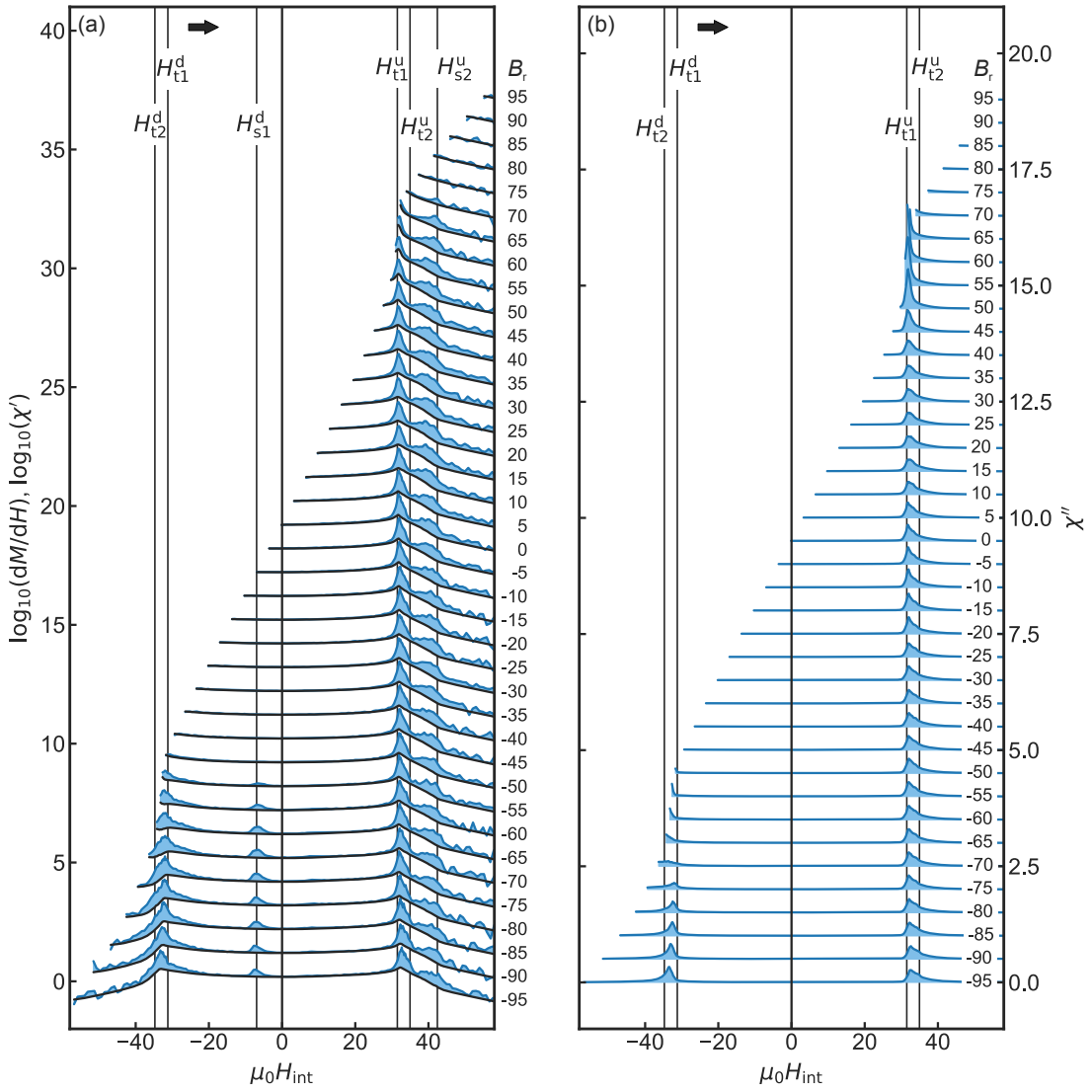

Figure 5.10: Susceptibility data inferred from FORC measurements at a temperature of 2 K with field along ⟨100⟩ for various reversal fields. The respective reversal field is labeled on the right side of each trace. (a) Logarithm of differential susceptibility, dM/dH, and real part of ac-susceptibility, χ_r. (b) Imaginary part of the ac-susceptibility, χ''.

5.2 Discussion

The importance of magnetocrystalline anisotropies for stabilizing the low-temperature skyrmion phase and the tilted-conical phase was highlighted in the recent neutron study [119]. This understanding is further supported by the strong anisotropies of magnetization, susceptibility, and heat capacity measured during this work. In the following, we will discuss the effects of magnetocrystalline anisotropy in further detail.

This Section is organized as follows. In Sec. 5.2.1, we begin with a discussion of anisotropy effects in field dependent magnetization measurements, comparing the behavior of Cu_2OSeO_3 with other chiral magnets. Next, in Sec. 5.2.2, we discuss in detail the anisotropy effects of Cu_2OSeO_3. Moreover, based on the extensive magnetization data, we extract the temperature dependence of the associated energies and ultimately infer the temperature dependence of the cubic anisotropy constant. In Sec. 5.2.3, we address the effective energy landscape arising from the interaction of a modulated magnetic structure with the cubic anisotropy. Finally, in Sec. 5.2.4 we discuss the strong hysteretic effects of the low-temperature skyrmion phase, focusing on the nucleation of skyrmions.

5.2.1 Anisotropy of the Magnetization

Compared to other cubic chiral magnets, Cu_2OSeO_3 has an unusually strong magnetocrystalline anisotropy. Nonetheless, effects of magnetocrystalline anisotropy are also prevalent in other cubic chiral magnets, although not as pronounced.

The magnetization behavior of chiral magnets with vanishing anisotropy is based solely on the rotation of the individual spins into the field direction, which without anisotropy also corresponds to the propagation direction of the conical helix. This results in a linear increase in magnetization until saturation and is comparable to the behavior of a uniaxial ferromagnet with an easy-plane anisotropy, magnetized along the hard axis. The slope is determined solely by the competition of Dzyaloshinskii-Moriya interaction and ferromagnetic exchange. In contrast, non-vanishing magnetocrystalline anisotropy results in orientation dependent deviations from the linear behavior.

A comparison of the magnetization behavior of Cu_2OSeO_3 with two archetypal chiral magnets, namely $Fe_{0.8}Co_{0.2}Si$ and MnSi, is given in Fig. 5.11. For a better comparison, the magnetization and field axes are shown in units of the saturation magnetization, M_s, and the upper critical field, H_{c2}. The saturation magnetization, M_s, is determined at fields well above H_{c2} while the upper critical field, H_{c2}, was selected for the direction which shows the largest value. Of the three materials shown, Cu_2OSeO_3 displays the strongest orientational anisotropy, and the magnetization as a function of field is clearly nonlinear.

It must be emphasized that if the magnetization is rising faster along one direction compared to other directions, this direction is favored by the magnetocrystalline anisotropy. As a function of field, we observe two intersections of the magnetization of the $\langle 111 \rangle$ and $\langle 100 \rangle$ orientation where the ordering of the magnetization changes. At very low fields, the magnetization is essentially isotropic up to H_{c1} of the $\langle 100 \rangle$ orientation. With a further increase in field, the magnetization of the $\langle 100 \rangle$ orientation rises above the

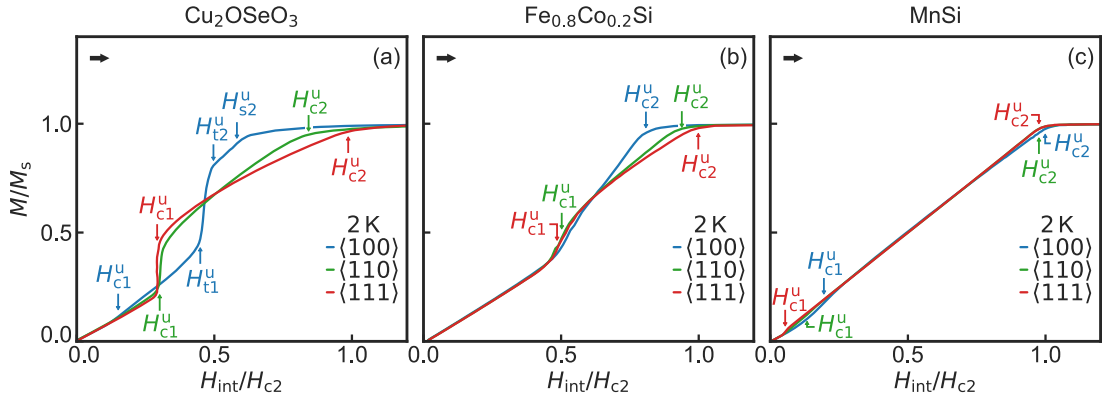

Figure 5.11: Magnetization of Cu_2OSeO_3, $Fe_{0.8}Co_{0.2}Si$, and MnSi illustrating the effects of magnetocrystalline anisotropy on the magnetization. (a) Magnetization of Cu_2OSeO_3, exhibiting strong $\langle 100 \rangle$ easy axis anisotropy. (b) Magnetization of $Fe_{0.8}Co_{0.2}Si$, exhibiting moderate $\langle 100 \rangle$ easy axis anisotropy. (c) Magnetization of MnSi, exhibiting very weak $\langle 111 \rangle$ easy axis anisotropy.

magnetization of the other orientations, suggesting magnetocrystalline anisotropy favors the $\langle 100 \rangle$ orientation. Surprisingly at H_{c1} of the $\langle 111 \rangle$ orientation, the order changes and the magnetization of the $\langle 111 \rangle$ orientation rises to the top, suggesting a favorable $\langle 111 \rangle$ orientation at intermediate fields. At larger fields, at approximately H_{t1} the ordering changes once again and the $\langle 100 \rangle$ orientation rises to the top, suggesting a favored $\langle 100 \rangle$ orientation again. We note that this effect does not indicate a field dependence of the magnetocrystalline anisotropy constant. Rather, it is the result of the modulated magnetic structure changing with field, which in turn changes the anisotropy energy contribution.

The magnetization of $Fe_{0.8}Co_{0.2}Si$, as shown in Fig. 5.11(b) resembles that of Cu_2OSeO_3, albeit with less pronounced anisotropy. Similar to Cu_2OSeO_3, $Fe_{0.8}Co_{0.2}Si$ exhibits an easy $\langle 100 \rangle$ orientation. The H_{c1} field, however, is located at much larger fields and is almost isotropic, which might be related to strong disorder pinning, prevalent in the series of $Fe_{1-x}Co_xSi$ alloys. As a function of field $Fe_{0.8}Co_{0.2}Si$ shows a preferred $\langle 111 \rangle$ orientation at intermediate fields and a favored $\langle 100 \rangle$ orientation at large fields. The magnetization shows a single intersection of the $\langle 111 \rangle$ and $\langle 100 \rangle$ direction, with an elevated magnetization in the $\langle 100 \rangle$ direction at magnetic fields above the intersection and an elevated magnetization in the $\langle 111 \rangle$ direction at fields below, down to H_{c1}. The second intersection at low fields as seen in Cu_2OSeO_3, however, is not observed, possibly due to the large H_{c1} value. Also, the signatures of the tilted-conical and low-temperature skyrmion phase, the almost vertical increase of M followed by the step increase above, are apparently absent.

MnSi, in comparison, is the perfect example of a very weak anisotropy, easy $\langle 111 \rangle$ axis system. The field dependent magnetization, as shown in Fig. 5.11(c) is nearly linear, and only minor differences between the various orientations may be observed, notably at low and high fields. Similar to Cu_2OSeO_3 two intersections between the $\langle 111 \rangle$ and

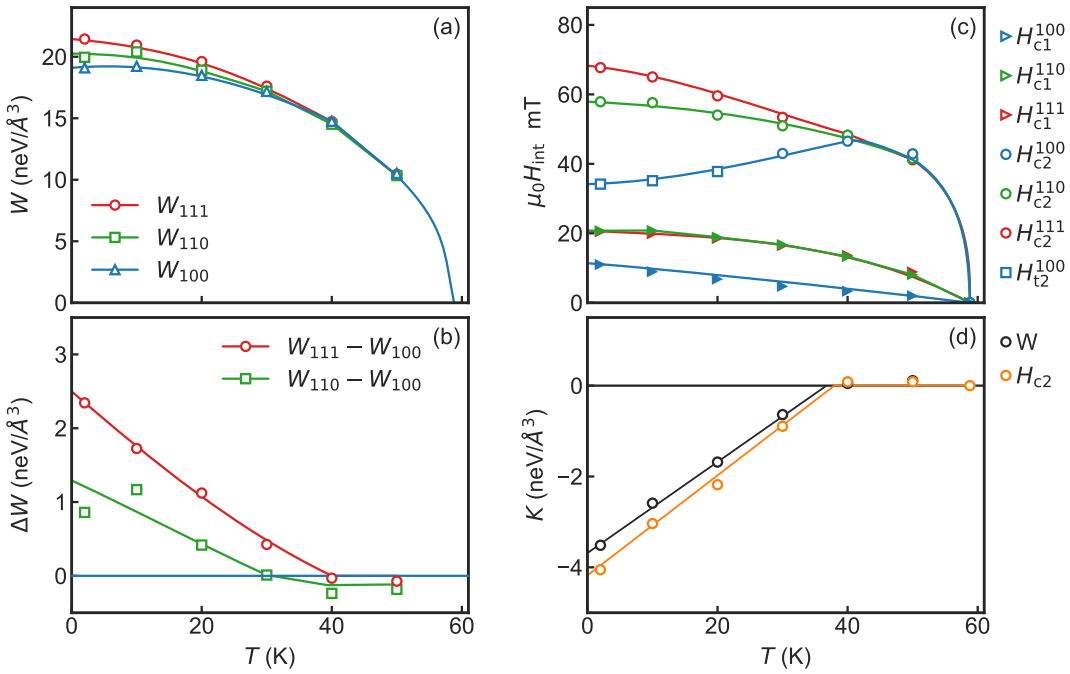

Figure 5.12: Magnetic work, W, critical fields and cubic anisotropy constant, K, inferred from magnetization and susceptibility data following ZFC. (a) Temperature dependence of the magnetic work expended to reach saturation for field along $\langle 111 \rangle$ (red), $\langle 110 \rangle$ (green) and $\langle 100 \rangle$ (blue). (b) Difference in magnetic work relative to the $\langle 100 \rangle$ orientation. (c) Orientation dependence of the critical fields. (d) Cubic anisotropy constant, K, inferred from the magnetization work (black) and critical fields (orange).

$\langle 100 \rangle$ magnetization may be seen, although barely visible. At low and high fields an elevated magnetization in the $\langle 111 \rangle$ orientation may be seen and a barely visible elevated magnetization in the $\langle 100 \rangle$ orientation at intermediate fields. Furthermore, the helical to conical transition, H_{c1}, occurs at a drastically smaller field compared to Cu_2OSeO_3.

In summary, the effects of magnetocrystalline anisotropy yield a surprisingly complex magnetization behavior as a function of field. The magnetocrystalline anisotropy is undoubtedly the strongest in Cu_2OSeO_3, followed by $Fe_{0.8}Co_{0.2}Si$ and weakest in MnSi. Both Cu_2OSeO_3, $Fe_{0.8}Co_{0.2}Si$ have an easy $\langle 100 \rangle$ axis, while MnSi favors the $\langle 111 \rangle$ orientation. The helical to conical transition, H_{c1}, is smallest in MnSi and largest in $Fe_{0.8}Co_{0.2}Si$ yet almost isotropic suggesting a disorder-driven effect.

5.2.2 Magnetocrystalline Anisotropy

The magnetic anisotropy energy may be inferred quantitatively from the field dependent magnetization data by means of the magnetic work,

$$W = \int_{M_0}^{M_1} \mu_0 H dM, \tag{5.1}$$

corresponding to the area between the ordinate and the magnetization curve in a $M(B)$ diagram. The magnetic work is related to the free energy density, dF, by the laws thermodynamics, reading [24, p. 123]

$$dW = dF + \underbrace{T\delta_i S}_{\text{entropy production}} + \underbrace{S\mathrm{d}T}_{\text{magneto caloric effect}} \tag{5.2}$$

In isothermal conditions and assuming reversible behavior ($T\delta_i S = S\mathrm{d}T = 0$), the magnetic work equals exactly the change in free energy from M_1 to M_2. Strictly speaking, irreversible processes as they are found in the $\langle 100 \rangle$ orientation do not justify fully the assumption of reversibility. Nonetheless, these energetic corrections are much weaker compared to the anisotropy energy and will be ignored in the following.

The change in free energy

$$\Delta F = \int_{M_0}^{M_1} dF = \Delta F_\mathrm{I} + \Delta F_\mathrm{A} \tag{5.3}$$

is comprised of an isotropic contribution, ΔF_I, incorporating the exchange and Dzyaloshinskii-Moriya interactions as well as an anisotropic contribution, ΔF_A, arising from the magnetocrystalline anisotropy. As a word caution, it should be noted that the sample geometry itself may lead to anisotropic contributions to the free energy due to demagnetizing fields. Great care has been taken to avoid such systematic errors. The magnetic work is therefore always calculated after the demagnetizing field correction.

Shown in Fig. 5.12(a) is the magnetic work expended to saturate the magnetization at various temperatures with the magnetic field aligned along the $\langle 111 \rangle$, $\langle 110 \rangle$ and $\langle 100 \rangle$ orientations. The magnetic work is calculated from field dependent magnetization measurements following ZFC, starting in zero field with $M_1 = 0$ and ending in saturation with $M_2 = M_\mathrm{s}$.

With decreasing temperature, below T_c, the magnetic work increases monotonically. In the zero temperature limit, we find a magnetic work of $W \approx 20\,\mathrm{neV\,\AA^{-3}}$, in excellent agreement with DFT calculations, yielding $\Delta F = 23.8\,\mathrm{neV\,\AA^{-3}}$ [149]. Towards low temperatures, differences between the individual orientations may be observed, resulting from the magnetocrystalline anisotropy. This is further illustrated in Fig. 5.12(b) showing the difference in magnetic work between $\langle 111 \rangle$ and $\langle 100 \rangle$ as well as $\langle 110 \rangle$ and $\langle 100 \rangle$, respectively. Differences arise below 40 K, increasing monotonically with decreasing temperature and are most pronounced between the $\langle 111 \rangle$ and $\langle 100 \rangle$ orientation. In the

zero temperature limit, we find an energy difference of $\Delta W \approx 2\,\mathrm{neV\,\AA^{-3}}$, approximately one-tenth of the isotropic energy contribution.

Assuming a purely cubic anisotropy of the form

$$F_{\mathrm{A}} = K(\hat{M}_x^4 + \hat{M}_y^4 + \hat{M}_z^4), \tag{5.4}$$

with $\hat{M}_i = M_i/|M|$ the direction cosines of the magnetization vector, the anisotropy constant K may be inferred from the energy differences, shown in Fig.5.12(b).

We refer to Sec. 3.4.2 for technical details. We note that in modulated magnetic structures, Eq. 5.4 must be replaced by an integral over the magnetic unit-cell, as shown in the following section. In the field polarized state, however, this is not necessary.

In a seminal study Grigoriev et al. have shown recently how cubic anisotropies affect the upper critical field H_{c2} [88]. The upper critical field may be inferred by minimizing the free energy, including ferromagnetic exchange, Dzyaloshinskii-Moriya, Zeeman interaction as well as cubic anisotropies with respect to the opening angle of a conical helix propagating along field. The upper critical field is then given by the magnetic field at which the opening angle vanishes. In turn, the cubic anisotropy may then be determined by comparing the upper critical field of two different orientations Considering the assumption of $\mathbf{k} \parallel \mathbf{H}$, this type of analysis prohibits comparisons of the $\langle 100 \rangle$ orientation due to the emergence of the tilted-conical phase.

A surprising result of this study is that for sufficiently strong magnetic anisotropies the conical helix becomes unstable at finite opening angles and a first-order transition into the field polarized state is anticipated, with a vertical increase of the magnetization at this transition. The experimentally observed tilted-conical phase, however, shows that the first order transition is avoided by tilting against the magnetic field direction. Moreover, more complex magnetic structures such as skyrmion lattices have not been considered.

Shown in Fig.5.12(c) is the orientation dependence of the critical fields H_{c1} and H_{c2} as a function of temperature. The critical fields are inferred from field dependent susceptibility data following ZFC, with field along $\langle 111 \rangle$ (red), $\langle 110 \rangle$ (green) and $\langle 100 \rangle$ (blue). We note that due to the emergence of the tilted-conical phase in the $\langle 100 \rangle$ orientation at low fields, H_{c2} is replaced by H_{t2} at temperatures below 30 K. With decreasing temperature, the helical to conical transition, H_{c1} increases monotonically for all orientations. Compared to the $\langle 111 \rangle$ and $\langle 110 \rangle$ orientation, the H_{c1} value of the $\langle 100 \rangle$ orientation is notably smaller. The $\langle 111 \rangle$ and $\langle 110 \rangle$ orientations, however have an almost identical H_{c1}. In contrast, at high temperatures the upper critical field, H_{c2}, is essentially isotropic but diverges at temperatures below 40 K, with the $\langle 111 \rangle$ orientation showing the largest and the $\langle 100 \rangle$ orientation, the lowest values.

The anisotropy constant, K, calculated from H_{c2} in the $\langle 111 \rangle$ and $\langle 110 \rangle$ orientation is shown in Fig. 5.12(d). We refer to Sec. 3.4.3 for details of the analysis procedure. Overall excellent agreement between K inferred from the magnetization work and H_{c2} is observed, shown as black and orange symbols, respectively. At high temperatures, the anisotropy constant is essentially zero. Below $T \approx 40$ K, however, a finite anisotropy constant emerges, decreasing monotonically towards low temperatures.

Theoretically, an instability of the conical phase is expected if the anisotropy energy in the $\langle 100 \rangle$ orientation exceeds 1/18 of the isotropic energy contribution, arising from

the Dzyaloshinskii Moriya interaction [88]. This criterion is met at temperatures below $T \approx 25\,\mathrm{K}$, consistent with the emergence of the tilted-conical phase.

We note that within the accuracy of the estimate it is not possible to rule out a finite K constant and a change in sign at temperatures above $\approx 40\,\mathrm{K}$. However, it is important to emphasize that the easy axis of the magnetic helix in zero-field remains in the $\langle 100 \rangle$ orientation at all temperatures. Deviations between the anisotropy constant inferred from the magnetization work and the critical fields may further hint towards higher order contributions. To resolve these questions, however, more specific measurements of the magnetocrystalline anisotropy are necessary, using, for example, magnetic torque or ferromagnetic resonance based methods on specially prepared isotropic samples, which is beyond the scope of this study.

5.2.3 Effective Energy Landscape

The complex anisotropic behavior observed in chiral magnets as a function of field is an effect of the cubic anisotropy, acting on a nonuniform magnetic structure. For what follows, it proves helpful to review the effects of cubic magnetocrystalline anisotropy for uniform magnetic structures, such as ferromagnets before turning towards the helical spin texture.

Magnetocrystalline anisotropy is the directional dependence of the magnetic properties of a material in relation to its crystal lattice and was first discovered by K. Beck in 1918 in cubic Fe-Si steel single crystals [30]. Phenomenologically, the magnetocrystalline anisotropy may be described as an additional anisotropic contribution F_A to the total free energy, which is typically represented as an expansion in direction cosines of the magnetization vector,

$$\hat{M}_i = \frac{M_x}{|\mathbf{M}|}. \tag{5.5}$$

The leading-order contribution to the magnetocrystalline anisotropy energy allowed by the cubic symmetry is then given by the quartic term

$$F_\mathrm{aniso} = K(\hat{M}_x^4 + \hat{M}_y^4 + \hat{M}_z^4) = \begin{cases} 1 & \langle 100 \rangle \\ 1/2 & \langle 110 \rangle \\ 1/3 & \langle 111 \rangle \end{cases} \tag{5.6}$$

with the anisotropy constant K.

Shown in Fig.5.13 is the energy surface of the quartic term of the cubic anisotropy acting on a single spin for $K = 0$, $K > 0$ and $K < 0$. The size of the anisotropy energy is encoded in the radius and the color, with red corresponding to large and blue to small energies. For vanishing anisotropy, the energy surface is equivalent to a sphere indicating the isotropic nature. This rotational degeneracy is lifted at finite values of K. For $K > 0$ as shown in Fig. 5.13(b), this gives rise to six energetically equivalent magnetic easy axes along the $\langle 100 \rangle$ orientations, representing the orientations with the lowest anisotropy

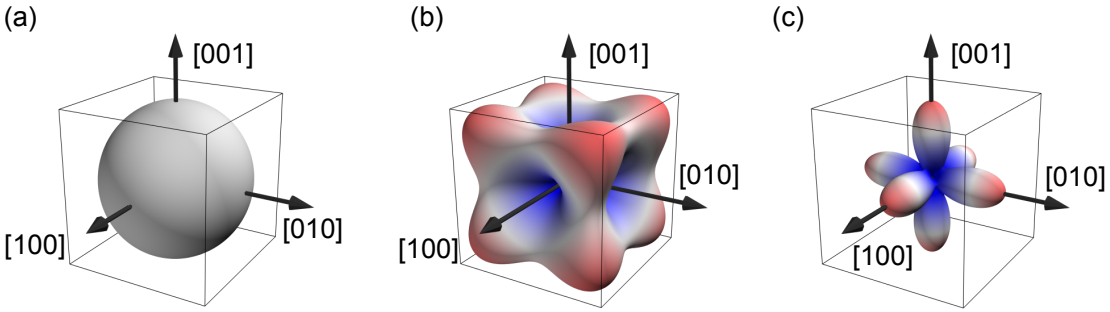

Figure 5.13: Illustration of the three-dimensional energy surface associated the leading-order cubic anisotropy term. The size of the anisotropy energy is encoded in the radius and the color, with red corresponding to large and blue to small energies. (a) Isotropic, spherical energy surface for vanishing anisotropy constant $K = 0$. (b) Energy surface, associated with $K < 0$, leading to easy $\langle 100 \rangle$ and hard $\langle 111 \rangle$ axes. (c) Energy surface, associated with $K > 0$, leading to easy $\langle 111 \rangle$ and hard $\langle 100 \rangle$ axes.

energy. The highest magnetocrystalline energy is found along the eight $\langle 111 \rangle$ orientations, representing the hard magnetic axes of the system.

Changing the sign of K reverses the hard and easy axes of the system. This is illustrated in Fig.X showing the energy surface for $K < 0$. Here, the $\langle 111 \rangle$ orientations are the easy magnet axes while the $\langle 100 \rangle$ orientations are the hard magnetic axes.

The effects of magnetocrystalline anisotropy on modulated magnetic structures are non-trivial. As each spin is oriented differently, Eq. 5.6 must be replaced by an integral

$$F_{\text{aniso}} = K \int (\hat{M}_x^4 + \hat{M}_y^4 + \hat{M}_z^4) \mathrm{d}V \tag{5.7}$$

capturing the individual contributions of each spin in the magnetic unit cell. The non-trivial behavior is further complicated by field dependent changes of the spin arrangement, which in turn change the energetic contributions to the free energy. In the following, we will discuss the effects on a conical spin arrangement, which may help in understanding the peculiar field dependence of the magnetization of chiral magnets. We assume a pristine conical helix with a propagation vector k and an opening angle α, defined as the angle between the spins and the propagation direction.

Shown in Fig. 5.14 is the angular spin distribution of a conical helix at various helix angles and orientations relative to the energy surface of the quartic anisotropy term with $K < 0$. The spin distribution is illustrated by colored arrows with the helical propagation aligned along [001] (first row, blue), [011] (second row, green) and [111] (third row, red). Helix angles of $\alpha = 80°$, $\alpha = 55°$ and $\alpha = 10°$ are shown in the first, second and third column, respectively. The energy surface of the quartic anisotropy term with $K < 0$ is equivalent to the energy surface shown previously in Fig. 5.13(b), where $\langle 100 \rangle$ and $\langle 111 \rangle$ correspond to the magnetic easy and hard axis, respectively. The size of the energy is

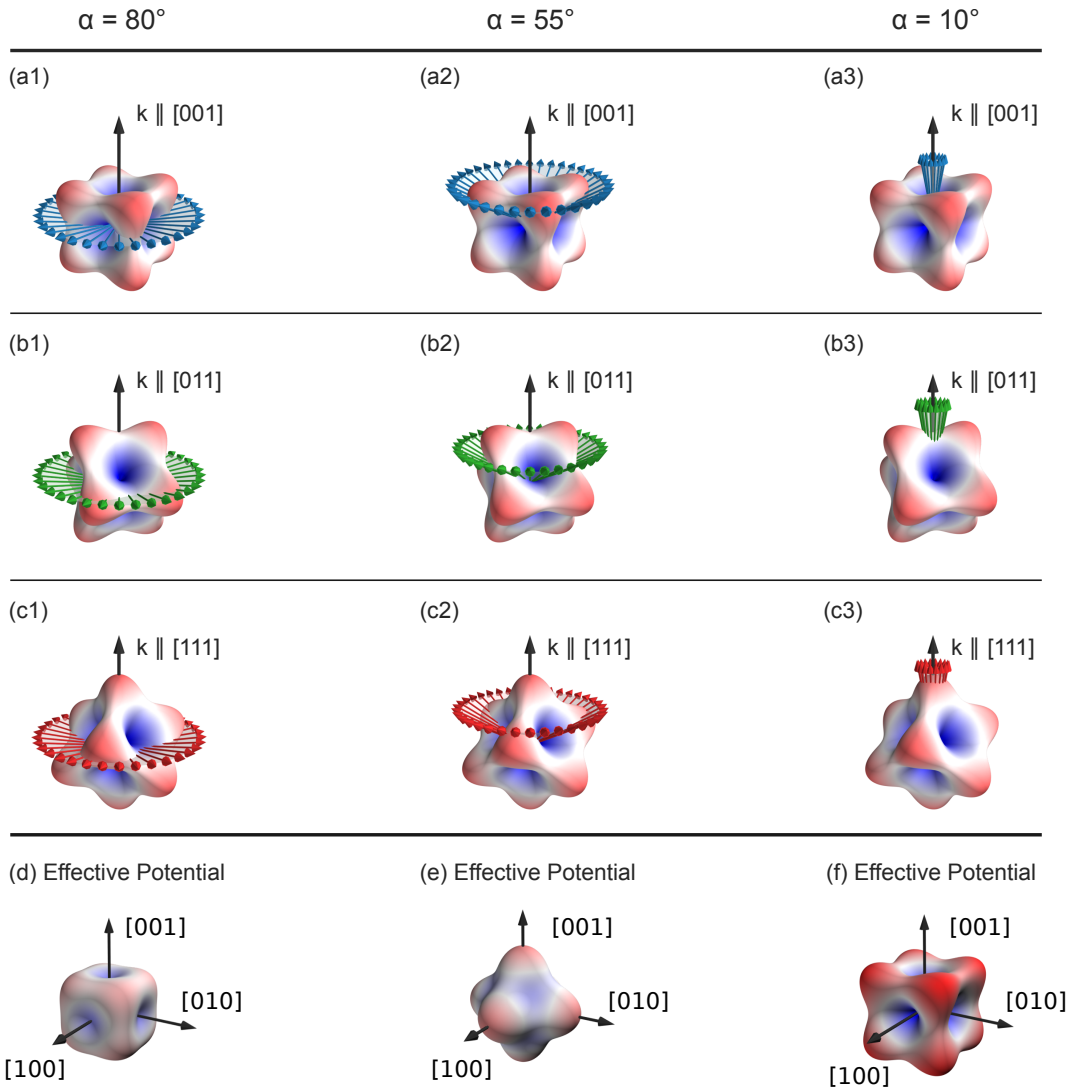

Figure 5.14: Angular spin distribution of the conical helix relative to the energy surface of the quartic cubic anisotropy term with $K > 0$. Spin distribution is shown as colored arrows with the helical propagation k along [001] (first row, blue), [011] (second row, green) and [111] (third row, red) and helical opening angles $\alpha = 80°$ (1st column), $\alpha = 55°$ (2nd column) and $\alpha = 10°$ (3rd column) (d1)–(d3) Corresponding effective energy surface.

encoded in the radius as well as the color shading, with blue and red colors corresponding to small and large energies, respectively.

Due to the non-colinear magnetic structure, the individual spins are arranged differently and thus contribute different amounts to the total anisotropy energy. The total anisotropy energy is thus obtained by integrating all individual contributions of the spins of a helix.

Accordingly, an effective energy surface may be derived by varying the propagation direction, which reflects the orientation dependence of the helix at a given opening angle. The corresponding effective potential, ignoring a constant offset, reads

$$K_{eff}(\alpha)(\hat{q}_x^4 + \hat{q}_y^4 + \hat{q}_z^4) \tag{5.8}$$

with $\hat{q}_i = q_i/|q|$ the direction cosines of the helix propagation and an effective anisotropy constant, $K_{eff}(\alpha)$, depending on the opening angle α. It is analogous to the conventional cubic potential, but depends on the orientation of the helix instead of the spin.

The effective energy surface for the three opening angles $\alpha = 80°$, $\alpha = 55°$ and $\alpha = 10°$, is shown in Fig. 5.14(d1)–(d3), respectively. At large opening angles, as shown by the example of $\alpha = 80°$ in Fig. 5.14(d1), the energy surface exhibits a weak $\langle 100 \rangle$ easy-axis anisotropy with hard $\langle 111 \rangle$ axes. By aligning along the $\langle 100 \rangle$ axis, the conical helix gains the most energy since all helical spins are close to one of four easy $\langle 100 \rangle$ axes while avoiding all hard $\langle 111 \rangle$ axes.

Surprisingly, at intermediate opening angles, illustrated in Fig. 5.14(d2) for $\alpha = 55°$, the easy and hard axes switch and a weak $\langle 111 \rangle$ easy-axis anisotropy is observed. This results from the fact that at intermediate opening angles and propagation along $\langle 100 \rangle$ all spins are very close to one of four $\langle 111 \rangle$ hard axes, resulting in a substantial energy penalty which is avoided for other helix orientations.

At small opening angles, shown in Fig. 5.14(d2) for $\alpha = 10°$, the easy and hard axes switch once again as the spins converge towards the field polarized state and the effective energy surface approaches the conventional energy surface (c.f. Fig.5.13(b)).

The change of the effective anisotropy during the magnetization process is further illustrated in Fig. 5.15, showing magnetization data and corresponding magnetic work. Fig. 5.15(a) presents typical magnetization data, shown with H_{int} against M. The data is measured at a temperature of 2 K following ZFC with field along $\langle 111 \rangle$, $\langle 110 \rangle$, and $\langle 100 \rangle$. The magnetization features two intersections of the $\langle 111 \rangle$ and $\langle 110 \rangle$ orientations with the $\langle 100 \rangle$ orientation. The magnetic work $W(M) = \int B \, \mathrm{d}M$, inferred from the magnetization data, is shown in Fig. 5.15(b), relative to the magnetic work of the $\langle 100 \rangle$ orientation. It shows the difference in free energy between the various orientations as a function of M. As a function of M it reflects the behavior of the effective anisotropy shown in Fig. 5.14(d1)–(d3). In the limit of large M, close to the saturation magnetization, the $\langle 100 \rangle$ orientation is clearly lowest in energy, identifying the $\langle 100 \rangle$ orientation as the easy magnetic axis. Similarly at small values of M ($M \leq 0.4\mu_B$/f.u.), both $\langle 111 \rangle$ and $\langle 110 \rangle$ are energetically larger than $\langle 100 \rangle$. At intermediate magnetization levels, however, the free energy of the $\langle 111 \rangle$ and $\langle 110 \rangle$ orientation drops below the $\langle 100 \rangle$ orientation, equivalent to a change of the effective anisotropy (change in sign of K_{eff}) The magnetization interval in which the inversion occurs corresponds to the magnetization interval of the tilted-conical phase.

We note that, the magnetization work at very small values of M ($M \leq 0.2\mu_B$/f.u.) is essentially isotropic and does not reflect the effective anisotropy landscape, as shown in Fig. 5.14(d1). This is a result of the somewhat indirect control of the helix propagation using the magnetic field. At low fields, the helix propagation is always aligned along

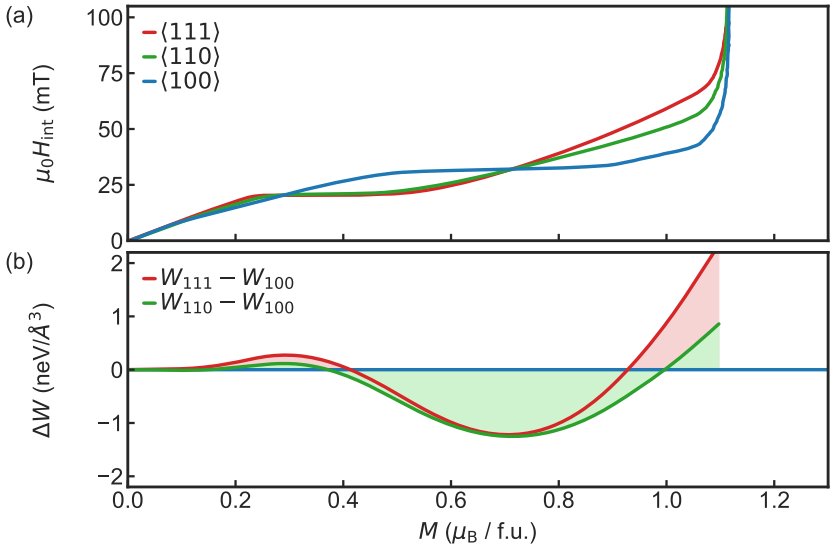

Figure 5.15: Magnetization and magnetic work illustrating the field dependence of the effective anisotropy. (a) Internal magnetic field as a function of magnetization. (b) Magnetic work, inferred from magnetization data, relative to the ⟨100⟩ orientation.

⟨100⟩, and as such we do not probe the energy landscape. It is also helpful to note that the magnetic work, calculated from the magnetization measures the change in free energy relative to the initial state. Therefore, to accurately compare the free energy between different orientations, we need to guarantee the same initial state. This is not possible under HFC because, in the ⟨100⟩ orientation, the helical domains are not populated equally, evident as the missing H_{c1} transition.

In conclusion, the complex interplay between the conical helix and the cubic anisotropies may be described by an effective cubic anisotropy. At intermediate fields, the sign of the effective anisotropy constant changes, thus penalizing a helical propagation along the ⟨100⟩ orientation. This is consistent with measurements of magnetic work, which show an energetic disadvantage of ⟨100⟩ orientation at intermediate magnetic fields, where the tilted-conical phase emerges. This might explain the tilting away from the ⟨100⟩ orientation of the tilted-conical phase. It must be stressed, however, that in contrast to the theoretical considerations the opening angle is controlled rather indirectly, using the magnetic field. Furthermore, we have not considered harmonic distortions of the conical helix, which might also play a role.

5.2.4 Nucleation of the Low-Temperature Skyrmion Phase

Finally, in this section, we will compile and discuss our findings regarding the nucleation of the low-temperature skyrmion phase. As we have extensively shown, the low-temperature skyrmion phase emerges in the ⟨100⟩ orientation only. Regardless of the temperature vs.

field protocol, the tilted-conical phase always appears first, the skyrmion phase second. Similarly, the tilted conical phase disappears first, the skyrmion second. Moreover, FORC measurements have unambiguously shown that the low-temperature skyrmion phase nucleates only within the field range of the tilted-conical phase, consistent with neutron scattering. Unlike the high-temperature skyrmion phase, however, no dissipative signatures are observed when leaving the low-temperature skyrmion phase, suggesting a drastic reduction of the associated timescales. In addition, the phase boundaries of the skyrmion phase are highly hysteretic, while no hysteresis is observed for the tilted-conical phase. This may be understood by the fact that the phase transition into the tilted conical phase is of second-order, and as such appears as soon as the tilted-conical phase is thermodynamically stable. In contrast, a transition from trivial phases to a skyrmion phase is always first order and in general accompanied by hysteresis.

Considering the wide hysteresis in the magnetic field and the coexistence of the LT-skyrmion phase with the conical, tilted-conical and field polarized state, the question arises how wide the thermodynamically stable field range of the low-temperature skyrmion phase may be. Two limiting scenarios, compatible with the experimental phase diagram, may be distinguished:

(i) The low-temperature skyrmion phase is thermodynamically stable only within the narrow field region of the tilted-conical phase, but survives as a metastable state within the conical and the field-polarized state.

(ii) The low-temperature skyrmion phase is stable in a much wider field region, extending beyond the field range of the tilted-conical phase, yet nucleates only within the tilted-conical phase.

Experimentally, the stabilization of the high-temperature skyrmion phase of Cu_2OSeO_3 at low temperatures, covering a wide field range has already been shown [93, 119]. Therefore, an exceptionally wide hysteresis is not unlikely. Theoretical calculations, however, suggest that the skyrmion phase is stable in a much wider field range compared to the field range of the tilted-conical phase [119]. This would imply a reduction of the nucleation barrier within the tilted-conical phase compared to the conical or field-polarized state and a number of factors may contribute to a reduction of the barrier.

It is well known, that for a nucleus to form the energy barrier resulting from the interfacial energy to the surrounding phase must be overcome [80]. The major contribution to the interfacial energy results from the formation of Bloch points. In a conical environment, however, the generation of a skyrmion requires the formation of a spiraling interface surrounding the skyrmion, due to the incompatibility of the longitudinal modulation of the conical helix with the rotational symmetry of a skyrmion[78, 79]. The formation of this interface is energetically costly and may further increase the nucleation barrier. Moreover, the energy contribution increases with the length of the skyrmion nucleus. It has been shown recently to affect the nucleation and may be responsible for the exceptional stability of metastable skyrmions within the conical phase at low temperatures [80].

Finally, in contrast to the conical or field-polarized state, the tilted-conical phase is a multi-domain state and thus forms domain walls. Topological defects naturally occurring

in chiral domain walls may then act as nucleation seeds for heterogeneous nucleation [80, 136].

In conclusion, given the experimental evidence in combination with theoretical calculations, the second scenario is more likely. Nonetheless, additional experiments such as relaxation experiments may lead to further insights, as relaxation is only expected within metastable states.

5.3 Conclusions

In recent years, the cubic chiral insulator Cu_2OSeO_3 attracted great scientific interest, combining the skyrmion lattice phase with strong magneto-electric coupling [49, 93, 100, 108, 112–114, 150]. Our recent discovery of a second skyrmion phase at low temperatures, disconnected from the conventional skyrmion phase at high temperatures and accompanied by a tilted-conical phase has shed new light on the stabilization mechanisms of skyrmion order [119]. Based on the observation of the formation of the novel phases only in the $\langle 100 \rangle$ orientation and supported by theoretical calculations, cubic anisotropy has been identified to play an essential role in the stabilization of the low-temperature skyrmion phase [119].

Motivated by these results, we have conducted a comprehensive study of single-crystal Cu_2OSeO_3, focussing on the low-temperature skyrmion phase, thermodynamically stabilized by cubic anisotropies and the tilted-conical phase. Using precision measurements of the magnetization and ac-susceptibility, we have studied in detail the magnetic properties of Cu_2OSeO_3 for magnetic fields along all major crystallographic orientations, complemented by specific heat measurements at selected temperatures and magnetic field orientations. We found clear thermodynamic signatures of a second skyrmion phase, emerging at low temperatures at the border between conical and field polarized state, accompanied by a tilted-conical phase.

Unlike the conventional skyrmion phase, emerging isotropically at high temperatures in finite fields, the low-temperature skyrmion phase, and the tilted conical phase emerge for field along $\langle 100 \rangle$ only. The phase boundaries of the low-temperature skyrmion phase are highly hysteretic, consistent with a previous neutron scattering study [119]. In contrast to the conventional skyrmion phase, the low-temperature skyrmion phase showed no signatures of dissipation in the ac-susceptibility at the phase boundaries. The tilted-conical phase, however, is associated with distinct dissipation effects and further accompanied by strong higher harmonics of the ac-susceptibility. To study the effects of dipolar interactions on the formation of skyrmion order, we investigated several different sample shapes and found enhanced smearing of the signatures with increasing demagnetizing factor. For large demagnetizing factors, we were thus unable to unambiguously identify the somewhat subtle signature of the low-temperature skyrmion phase. The dissipation signature of the tilted-conical phase, however, is found up to the largest demagnetizing factor investigated. As a major result, we quantitatively estimated the cubic anisotropy constant consistently from both magnetic work and critical magnetic fields. We found a cubic anisotropy constant of $K \approx -4\,\mathrm{neV\,\AA^{-3}}$ at low temperatures, vanishing above temperatures of $T \approx 40\,\mathrm{K}$.

In addition, we studied the nucleation of the low-temperature skyrmion phase through first-order reversal curve measurements and found compelling evidence that the low-temperature skyrmion lattice phase requires the tilted-conical phase to lower the nucleation barrier. Finally, we have demonstrated how cubic anisotropies influence the energy landscape of chiral magnets, which may aid the understanding of such complex phenomena.

CHAPTER 6

Summary and Outlook

Magnetic skyrmions represent noncollinear spin textures, found in a variety of different materials, consisting of nanometer-sized spin-whirls with particle-like properties. They have sparked the interest of the scientific community based on a variety of exciting properties ranging from emergent electrodynamics [61] including a topological Hall effect [51, 52] and spin transfer torques [61, 151] to magnetoelectric effects [49, 114]. In this study, we have addressed two critical issues related to magnetic skyrmions, namely kinetic and thermodynamic stability.

We began with a brief introduction Chapter 1, addressing nucleation and growth, magnetic viscosity and magnetocrystalline anisotropy. In Chapter 2, we provided a compact overview of the material class of cubic chiral magnets, addressing the generic phase diagram, the skyrmion lattice, emergent electrodynamics, topological stability and the nucleation and annihilation of magnetic skyrmions. This was followed by a specific introduction of $Fe_{1-x}Co_xSi$ and Cu_2OSeO_3, the chiral magnets investigated during this thesis. In Chapter 3, we summarized the experimental methods, techniques, and analyses used during this thesis.

In Chapter 4, we conducted a comprehensive study on a non-equilibrium skyrmion lattice state in bulk $Fe_{0.5}Co_{0.5}Si$, addressing the issue of stability and the associated energetics of the metastable state. Using extensive magnetization and ac-susceptibility measurements, we inferred the non-equilibrium phase diagram, hosting a metastable skyrmion lattice in a major portion of the phase diagram. A comparison with nonequilibrium skyrmion lattice states in other chiral magnets revealed a generic behavior of the nonequilibrium phase diagram. In addition, to investigate the relaxation dynamics and the associated energetics of the metastable skyrmion lattice, we conducted magnetic relaxation measurements and found a slow logarithmic decay of the metastable state with time. From the relaxation data, we inferred the distribution of activation energies in zero field using master-curve scaling. The distribution of activation energies consists of

a narrow peak at low energies, associated with the monopole-antimonopole nucleation barrier, superimposed on a broad distribution, dominating the relaxation behavior. As a result, the skyrmion lattice survives in a broadened band outside the thermodynamically metastable phase boundaries, where the system is thermodynamically unstable but kinetically stabilized beyond the topological protection. We suspect that the broad distribution originates from pinning of (anti-)monopoles since $Fe_{0.5}Co_{0.5}Si$ is known to exhibit strong compositional site disorder.

The exceptional stabilization of the nonequilibrium skyrmion phase, attributed to pinning of monopoles, may offer a new tuning mechanism for skyrmionic applications, not considered before. However, further studies may be necessary to establish the microscopics of the pinning mechanism. Moreover, the application of master curve scaling, not used before in the context of skyrmions, to infer the barrier distribution has proven to be very successful. Employing a similar analysis may allow further studies to infer the underlying energetics in other materials and may enable a straightforward evaluation of external effects such as electric fields, strain or even pressure on the formation of nonequilibrium skyrmion phases.

In Chapter 5, we reported the results of a comprehensive study of the magnetic properties of single-crystal Cu_2OSeO_3 utilizing measurements of the magnetization, ac-susceptibility, and specific heat, in particular tracking the influence of crystal orientation, cooling history and demagnetizing effects on the formation of skyrmion order.

We have successfully identified the thermodynamic signatures of the low-temperature skyrmion phase as well as tilted-conical phase, consistent with the recent neutron study, confirming the existence of these novel phases only within the $\langle 100 \rangle$ orientation. The low-temperature skyrmion phase is found to be highly hysteretic, yet lacks signs of dissipation. In contrast, the tilted-conical is linked to strong dissipation effects, further accompanied by strong higher harmonic ac-susceptibility signatures. Based on the magnetic work as well as the upper critical field H_{c2}, we have quantitatively inferred the cubic anisotropy constant as a function of temperature. Furthermore, using the example of a conical helix, we have demonstrated the complex interplay of modulated magnetic structures with cubic anisotropy, generic for all cubic chiral magnets. Using first-order reversal curves, we find that the low-temperature skyrmion phase nucleates only within the field range of the tilted-conical phase. Together with neutron scattering and ac-susceptibility, this provides compelling evidence that the tilted-conical phase aids the nucleation of the low-temperature skyrmion phase.

In summary, the formation of the low-temperature skyrmion phase and the tilted-conical phase raises further questions, among other things concerning the dynamics of these phases in the presence of strong cubic anisotropies, as well as magnetoelectric effects. Moreover, analogous to the metastable skyrmion phase in $Fe_{1-x}Co_xSi$, which enabled the study of the skyrmion decay by slowing down the timescales at low temperatures [46], Cu_2OSeO_3 offers the possibility to study the inverse process, the nucleation, in the zero temperature limit. Furthermore, the generic nature of the underlying mechanism may allow for similar phenomena in other materials. Although the cubic anisotropies in the materials reported so far appear to be weaker compared to Cu_2OSeO_3, they may play an essential role in new materials or hydrostatic pressure experiments. A potential candidate

worth revisiting might be MnSi under hydrostatic pressure. A short reevaluation of the literature concerning the magnetization under hydrostatic pressure [52, 152] reveals a peculiar field dependence, which suggests a significant increase in cubic anisotropy and may play a more important role in the formation of the partial order and non-Fermi liquid behavior than previously anticipated [153, 154].

Taken together, we have successfully investigated the thermodynamic and kinetic stabilization of skyrmion order in cubic chiral magnets and have provided valuable new insights into the underlying energetics.

Acknowledgements

This thesis would not have been possible without the help and support of many. First and foremost, I would like to thank my supervisor, Prof. Dr. Christian Pfleiderer, for giving me the opportunity to graduate. I'm particularly grateful for the guidance and support, for all the interesting projects and the opportunities to visit conferences all around the world. I have learned a lot in the last years. Secondly, I would like to express my gratitude to Prof. Dr. Peter Böni for the wonderful working environment at E21, the interesting conversations and legendary Christmas speeches.

In addition, I am particularly grateful for the assistance given by

- Dr. Andreas Bauer who has been an unstinting source of support and advise. Many plots and abstracts would have been much worse without your help. Moreover, I'm thankful for providing the $Fe_{1-x}Co_xSi$ and proof reading.
- Dr. Michael Wagner, for guiding me through my diploma thesis and the first years of my PhD,
- Alfonso Chacon, for the endless discussions, enhancing my understanding of skyrmions physics in general,
- My office mates, Dr. Andreas Bauer, Alfonso Chacon, and Pau Jorba, for the pleasant working atmosphere,
- Georg Benka, for helping with measurements and working on the gainz, #LEGDAY.
- Markus Kleinhans, for experimental support,
- Stefan Giemsa for technical support,
- the secretaries, Astrid Mühlberg and Martina Michel, for their support over the last years, and
- Helmuth Berger for providing the Cu_2OSeO_3 samples.

Throughout my PhD I had the pleasure to work with many great current and former colleagues at E21/E51. I am grateful for all support given and the great times we had

at work, conferences and triple D-days. I will always remember our discussions at coffee breaks, the barbecues, the oktoberfest, or simply enjoying an after work beer. In no particular order, I would like to thank Christian Pfleiderer, Peter Böni, Christoph Morkel, Alexander Regnat, Andreas Bauer, Alfonso Chacon, Andreas Wendl, Birgit Wiedemann, Christopher Duvinage, Christian Franz, Felix Rucker, Franz Haslbeck, Georg Benka, Jan Spallek, Marc Seifert, Markus Kleinhans, Michael Wagner, Pau Jorba, Philip Schmakat, Robert Ritz, Schorsch Sauther, Sebastian Mühlbauer, Stefan Giemsa, Steffen Säubert, Tim Adams, Tomek Schultz, Tommy Reimann, Wolfgang Simeth, Yingfan Ye and many more.

My acknowledgments would not be complete without thanking my fellow friends, Christoph Zollitsch, Christian Steyer, Sasha Mühlbrandt, and Christian Veth that have accompanied me on my journey through physics. A very special thank you goes out to my best friend, Christoph Zollitsch, for all the help over the years, and the strong support in mosh and circle pits a topologically nontrivial human vortex state, confirming the predominant counter clockwise rotation mode [155].

Also, I would like to thank my family for their endless support and encouragement. An finally, my loving and supporting wife, Sibylle Halder. Without all your help this would not have been possible.

Publications

1. **Observation of two independent skyrmion phases in a chiral magnetic material**
   A. Chacon, L. Heinen, M. Halder, W. Simeth, S. Mühlbauer, H. Berger, M. Garst, A. Rosch and C. Pfleiderer
   Nature Physics **14**, 936–941 (2018).

2. **Entropy-limited topological protection of skyrmions**
   J. Wild, T.N.G. Meier, S. Pöllath, M. Kronseder, A. Bauer, A. Chacon, M. Halder, M. Schowalter, A. Rosenauer, J. Zweck, J. Müller, A. Rosch, C. Pfleiderer and C.H. Back.
   Science Advances **3**, e1701704 (2017).

3. **Symmetry breaking, slow relaxation dynamics, and topological defects at the field-induced helix reorientation in MnSi**
   A. Bauer, A. Chacon, M. Wagner, M. Halder, R. Georgii, A. Rosch, C. Pfleiderer and A. Rosch
   Physical Review B **95**, 024429 (2017).

4. **Formation of a topological non-Fermi liquid in MnSi**
   R. Ritz, M. Halder, M. Wagner, C. Franz, A. Bauer, and C. Pfleiderer
   Nature **497**, 231 (2013).

5. **Giant generic topological Hall resistivity of MnSi under pressure**
   R. Ritz, M. Halder, C. Franz, A. Bauer, M. Wagner, R. Bamler, A. Rosch, and C. Pfleiderer
   Physical Review B **87**, 134424 (2013).

6. **Emergent electrodynamics of skyrmions in a chiral magnet**
   T. Schulz, R. Ritz, A. Bauer, M. Halder, M. Wagner, C. Franz, C. Pfleiderer, K. Everschor, M. Garst, and A. Rosch
   Nature Physics **8**, 301 (2012).

Bibliography

[1] R. Becker and W. Döring, Kinetische Behandlung der Keimbildung in übersättigten Dämpfen, Annalen der Physik **416**, 719 (1935).

[2] I. Lifshitz, Kinetics of ordering during second-order phase transitions, Sov. Phys. JETP **15**, 939 (1962).

[3] P. Chaddah, *First Order Phase Transitions of Magnetic Materials: Broad and Interrupted Transitions* (CRC Press, 2017).

[4] K. O'Grady, M. El-Hilo, and R. W. Chantrell, Time dependence effects in disordered systems, Journal of Applied Physics **76**, 6368 (1994).

[5] D. S. Fisher, M. P. A. Fisher, and D. A. Huse, Thermal fluctuations, quenched disorder, phase transitions, and transport in type-II superconductors, Physical Review B **43**, 130 (1991).

[6] S. B. Roy, G. K. Perkins, M. K. Chattopadhyay, A. K. Nigam, K. J. S. Sokhey, P. Chaddah, A. D. Caplin, and L. F. Cohen, First order magnetic transition in $CeFe_2$ alloys: Phase-coexistence and metastability, Physical Review Letters **92** (2004), 10.1103/PhysRevLett.92.147203, arXiv:cond-mat/0312352 .

[7] R. Becker, W. Döring, and J. Tillmans, *Ferromagnetismus* (Springer Berlin Heidelberg, 1939).

[8] G. Bertotti and I. D. Mayergoyz, *The Science of Hysteresis: 3-Volume Set* (Elsevier, 2005).

[9] J. Hopkinson, E. Wilson, and F. Lydall, I. Magnetic viscosity, Proceedings of the Royal Society of London **53**, 352 (1893).

[10] R. W. Chantrell, Magnetic viscosity of recording media, Journal of Magnetism and Magnetic Materials **95**, 365 (1991).

[11] R. Skomski, R. D. Kirby, and D. J. Sellmyer, Equivalence of sweep-rate and magnetic-viscosity dynamics, Journal of Applied Physics **93**, 6820 (2003).

[12] W. Brown, Thermal fluctuation of fine ferromagnetic particles, IEEE Transactions on Magnetics **15**, 1196 (1979).

[13] V. I. Mel'nikov, The Kramers problem: Fifty years of development, Physics Reports **209**, 1 (1991).

[14] P. Hänggi, P. Talkner, and M. Borkovec, Reaction-rate theory: Fifty years after Kramers, Reviews of Modern Physics **62**, 251 (1990).

[15] Z. JiangLin, J.-D. Bao, and G. Wenping, Kramers escape rate in nonlinear diffusive media, The Journal of Chemical Physics **124**, 024112 (2006).

[16] Weber Wilhelm, Ueber die Elasticität der Seidenfäden, Annalen der Physik **110**, 247 (1835).

[17] D. Kuhlmann, Zur Theorie der Nachwirkungserscheinungen, Zeitschrift für Physik **124**, 468 (1948).

[18] R. Street and J. C. Woolley, A Study of Magnetic Viscosity, Proceedings of the Physical Society. Section A **62**, 562 (1949).

[19] P. Gaunt, Magnetic viscosity in ferromagnets Part I, The Philosophical Magazine: A Journal of Theoretical Experimental and Applied Physics **34**, 775 (1976).

[20] P. Gaunt and G. J. Roy, Magnetic viscosity in ferromagnets Part II, The Philosophical Magazine: A Journal of Theoretical Experimental and Applied Physics **34**, 781 (1976).

[21] P. Gaunt, Magnetic viscosity and thermal activation energy, Journal of Applied Physics **59**, 4129 (1986).

[22] C. N. Guy, Spin glasses in low DC fields. II. Magnetic viscosity, Journal of Physics F: Metal Physics **8**, 1309 (1978).

[23] A. C. Mota, A. Pollini, P. Visani, K. A. Müller, and J. G. Bednorz, Relaxation effects in high T c superconductors, Physica Scripta **37**, 823 (1988).

[24] G. Bertotti, *Hysteresis in Magnetism: For Physicists, Materials Scientists, and Engineers* (Elsevier Science, 1998).

[25] Berndt Thomas, Muxworthy Adrian R., and Paterson Greig A., Determining the magnetic attempt time $t0$, its temperature dependence, and the grain size distribution from magnetic viscosity measurements, Journal of Geophysical Research: Solid Earth **120**, 7322 (2015).

[26] M. Volmer, *Kinetik Der Phasenbildung* (J. W. Edwards, 1939).

[27] K. Thieme, I. Avramov, and C. Rüssel, The mechanism of deceleration of nucleation and crystal growth by the small addition of transition metals to lithium disilicate glasses, Scientific Reports **6**, 25451 (2016).

[28] J. E. Shelby, *Introduction to Glass Science and Technology* (Royal Society of Chemistry, 2005).

[29] B. Cullity and C. Graham, *Introduction to Magnetic Materials* (Wiley, 2011).

[30] K. Beck, *Das magnetische Verhalten von Eisenkristallen bei gewöhnlicher Temperatur*, Tech. Rep. (ETH Zurich, 1918).

[31] J. Seidel, *Topological Structures in Ferroic Materials: Domain Walls, Vortices and Skyrmions* (Springer International Publishing, 2016).

[32] Y. Tokunaga, X. Z. Yu, J. S. White, H. M. Rønnow, D. Morikawa, Y. Taguchi, and Y. Tokura, A new class of chiral materials hosting magnetic skyrmions beyond room temperature, Nature Communications **6**, 7638 (2015).

[33] K. Karube, J. S. White, N. Reynolds, J. L. Gavilano, H. Oike, A. Kikkawa, F. Kagawa, Y. Tokunaga, H. M. Rønnow, Y. Tokura, and Y. Taguchi, Robust metastable skyrmions and their triangular–square lattice structural transition in a high-temperature chiral magnet, Nature Materials **15**, 1237 (2016).

[34] K. Karube, J. S. White, D. Morikawa, M. Bartkowiak, A. Kikkawa, Y. Tokunaga, T. Arima, H. M. Rønnow, Y. Tokura, and Y. Taguchi, Skyrmion formation in a bulk chiral magnet at zero magnetic field and above room temperature, Physical Review Materials **1**, 074405 (2017).

[35] L. D. Landau and E. M. Lifshitz, *Electrodynamics of Continuous Media* (Pergamon, 1984).

[36] P. Bak and M. H. Jensen, Theory of helical magnetic structures and phase transitions in MnSi and FeGe, Journal of Physics C: Solid State Physics **13**, L881 (1980).

[37] S. Mühlbauer, B. Binz, F. Jonietz, C. Pfleiderer, A. Rosch, A. Neubauer, R. Georgii, and P. Böni, Skyrmion lattice in a chiral magnet, Science **323**, 915 (2009).

[38] A. Bogdanov and D. Yablonskii, Thermodynamically stable "vortices" in magnetically ordered crystals. The mixed state of magnets, Zh. Eksp. Teor. Fiz **95**, 178 (1989).

[39] A. Bogdanov and A. Hubert, Thermodynamically stable magnetic vortex states in magnetic crystals, Journal of Magnetism and Magnetic Materials **138**, 255 (1994).

[40] A. Bogdanov and A. Hubert, The stability of vortex-like structures in uniaxial ferromagnets, Journal of Magnetism and Magnetic Materials **195**, 182 (1999).

[41] S. Buhrandt and L. Fritz, Skyrmion lattice phase in three-dimensional chiral magnets from Monte Carlo simulations, Physical Review B **88**, 195137 (2013).

[42] K. Everschor, *Current-Induced Dynamics of Chiral Magnetic Structures: Skyrmions, Emergent Electrodynamics and Spin-Transfer Torques*, Ph.D. thesis, Universität zu Köln (2012).

[43] T. H. R. Skyrme, A unified field theory of mesons and baryons, Nuclear Physics **31**, 556 (1962).

[44] P. Jaikumar and R. Ouyed, Skyrmion Stars: Astrophysical Motivations and Implications, The Astrophysical Journal **639**, 354 (2006).

[45] G. E. Brown and M. Rho, *The Multifaceted Skyrmion* (World Scientific, 2010).

[46] P. Milde, D. Köhler, J. Seidel, L. M. Eng, A. Bauer, A. Chacon, J. Kindervater, S. Mühlbauer, C. Pfleiderer, S. Buhrandt, C. Schütte, and A. Rosch, Unwinding of a Skyrmion Lattice by Magnetic Monopoles, Science **340**, 1076 (2013).

[47] T. Adams, S. Mühlbauer, C. Pfleiderer, F. Jonietz, A. Bauer, A. Neubauer, R. Georgii, P. Böni, U. Keiderling, K. Everschor, M. Garst, and A. Rosch, Long-Range Crystalline Nature of the Skyrmion Lattice in MnSi, Physical Review Letters **107**, 217206 (2011).

[48] Y. Hu, Direction-dependent stability of skyrmion lattice in helimagnets induced by exchange anisotropy, Journal of Magnetism and Magnetic Materials **455**, 54 (2018).

[49] S. Seki, X. Z. Yu, S. Ishiwata, and Y. Tokura, Observation of skyrmions in a multiferroic material, Science **336**, 198 (2012).

[50] X. Z. Yu, Y. Onose, N. Kanazawa, J. H. Park, J. H. Han, Y. Matsui, N. Nagaosa, and Y. Tokura, Real-space observation of a two-dimensional skyrmion crystal, Nature **465**, 901 (2010).

[51] A. Neubauer, C. Pfleiderer, B. Binz, A. Rosch, R. Ritz, P. G. Niklowitz, and P. Böni, Topological hall effect in the *a* phase of MnSi, Physical Review Letters **102**, 186602 (2009).

[52] R. Ritz, M. Halder, C. Franz, A. Bauer, M. Wagner, R. Bamler, A. Rosch, and C. Pfleiderer, Giant generic topological Hall resistivity of MnSi under pressure, Physical Review B **87**, 134424 (2013).

[53] M. M. a. Shinichiro Seki, *Skyrmions in Magnetic Materials*, 1st ed. (Springer International Publishing, 2016).

[54] C. Pfleiderer and A. Rosch, Condensed-matter physics: Single skyrmions spotted, Nature **465**, 880 (2010).

[55] N. Kanazawa, M. Kubota, A. Tsukazaki, Y. Kozuka, K. S. Takahashi, M. Kawasaki, M. Ichikawa, F. Kagawa, and Y. Tokura, Discretized topological Hall effect emerging from skyrmions in constricted geometry, Physical Review B **91**, 041122 (2015).

[56] J. C. Slonczewski, Current-driven excitation of magnetic multilayers, Journal of Magnetism and Magnetic Materials **159**, L1 (1996).

[57] L. Berger, Emission of spin waves by a magnetic multilayer traversed by a current, Physical Review B **54**, 9353 (1996).

[58] J. Grollier, P. Boulenc, V. Cros, A. Hamzić, A. Vaurès, A. Fert, and G. Faini, Switching a spin valve back and forth by current-induced domain wall motion, Applied Physics Letters (2003), 10.1063/1.1594841.

[59] M. Tsoi, R. E. Fontana, and S. S. P. Parkin, Magnetic domain wall motion triggered by an electric current, Applied Physics Letters (2003), 10.1063/1.1578165.

[60] A. V. Khvalkovskiy, D. Apalkov, S. Watts, R. Chepulskii, R. S. Beach, A. Ong, X. Tang, A. Driskill-Smith, W. H. Butler, P. B. Visscher, D. Lottis, E. Chen, V. Nikitin, and M. Krounbi, Basic principles of STT-MRAM cell operation in memory arrays, Journal of Physics D: Applied Physics **46**, 074001 (2013).

[61] T. Schulz, R. Ritz, A. Bauer, M. Halder, M. Wagner, C. Franz, C. Pfleiderer, K. Everschor, M. Garst, and A. Rosch, Emergent electrodynamics of skyrmions in a chiral magnet, Nature Physics **8**, 301 (2012).

[62] A. S. Schwarz, *Topology for Physicists*, 1st ed. (Springer-Verlag Berlin Heidelberg, 1994).

[63] G. Toulouse and M. Kléman, Principles of a classification of defects in ordered media, Journal de Physique Lettres **37**, 149 (1976).

[64] N. D. Mermin, The topological theory of defects in ordered media, Reviews of Modern Physics **51**, 591 (1979).

[65] H.-B. Braun, Topological effects in nanomagnetism: From superparamagnetism to chiral quantum solitons, Advances in Physics **61**, 1 (2012).

[66] S. Gupta and A. Saxena, *The Role of Topology in Materials* (Springer, 2018).

[67] A. Garel, Boundary conditions for textures and defects, Journal de Physique **39**, 225 (1978).

[68] D. Finkelstein and J. Rubinstein, Connection between Spin, Statistics, and Kinks, Journal of Mathematical Physics **9**, 1762 (1968).

[69] O. Eriksson, A. Bergman, L. Bergqvist, and J. Hellsvik, *Atomistic Spin Dynamics: Foundations and Applications* (Oxford University Press, 2017).

[70] A. Thiaville, J. M. García, R. Dittrich, J. Miltat, and T. Schrefl, Micromagnetic study of Bloch-point-mediated vortex core reversal, Physical Review B **67**, 094410 (2003).

[71] R. G. Elías and A. Verga, Magnetization structure of a Bloch point singularity, The European Physical Journal B **82**, 159 (2011).

[72] C. Schütte and A. Rosch, Dynamics and energetics of emergent magnetic monopoles in chiral magnets, Physical Review B **90**, 174432 (2014).

[73] D. Cortés-Ortuño, W. Wang, M. Beg, R. A. Pepper, M.-A. Bisotti, R. Carey, M. Vousden, T. Kluyver, O. Hovorka, and H. Fangohr, Thermal stability and topological protection of skyrmions in nanotracks, Scientific Reports **7**, 4060 (2017).

[74] F. Kagawa, H. Oike, W. Koshibae, A. Kikkawa, Y. Okamura, Y. Taguchi, N. Nagaosa, and Y. Tokura, Current-induced viscoelastic topological unwinding of metastable skyrmion strings, Nature Communications **8**, 1332 (2017).

[75] I. S. Lobanov, H. Jónsson, and V. M. Uzdin, Mechanism and activation energy of magnetic skyrmion annihilation obtained from minimum energy path calculations, Physical Review B **94**, 174418 (2016).

[76] A. Siemens, Y. Zhang, J. Hagemeister, E. Y. Vedmedenko, and R. Wiesendanger, Minimal radius of magnetic skyrmions: Statics and dynamics, New Journal of Physics **18**, 045021 (2016).

[77] J. Müller, J. Rajeswari, P. Huang, Y. Murooka, H. M. Rønnow, F. Carbone, and A. Rosch, Magnetic skyrmions and skyrmion clusters in the helical phase of Cu_2OSeO_3, Physical Review Letters **119**, 137201 (2017).

[78] J. C. Loudon, A. O. Leonov, A. N. Bogdanov, M. C. Hatnean, and G. Balakrishnan, Direct observation of attractive skyrmions and skyrmion clusters in the cubic helimagnet Cu_2OSeO_3, Physical Review B **97**, 134403 (2018).

[79] A. O. Leonov, T. L. Monchesky, J. C. Loudon, and A. N. Bogdanov, Three-dimensional chiral skyrmions with attractive interparticle interactions, Journal of Physics: Condensed Matter **28**, 35LT01 (2016).

[80] A. O. Leonov and K. Inoue, Homogeneous and heterogeneous nucleation of skyrmions in thin layers of cubic helimagnets, arXiv:1805.04990 [cond-mat] (2018), arXiv:1805.04990 [cond-mat] .

[81] V. Jaccarino, G. K. Wertheim, J. H. Wernick, L. R. Walker, and S. Arajs, Paramagnetic Excited State of FeSi, Physical Review **160**, 476 (1967).

[82] D. Shinoda and S. Asanabe, Magnetic Properties of Silicides of Iron Group Transition Elements, Journal of the Physical Society of Japan **21**, 555 (1966).

[83] M. A. Chernikov, L. Degiorgi, E. Felder, S. Paschen, A. D. Bianchi, H. R. Ott, J. L. Sarrao, Z. Fisk, and D. Mandrus, Low-temperature transport, optical, magnetic and thermodynamic properties of $Fe_{1-x}Co_xSi$, Physical Review B **56**, 1366 (1997).

[84] J. Beille, J. Voiron, and M. Roth, Long period helimagnetism in the cubic B20 $Fe_xCo_{1-x}Si$ and $Co_xMn_{1-x}Si$ alloys, Solid State Communications **47**, 399 (1983).

[85] N. Manyala, Y. Sidis, J. F. DiTusa, G. Aeppli, D. P. Young, and Z. Fisk, Magnetoresistance from quantum interference effects in ferromagnets, Nature **404**, 581 (2000).

[86] M. Motokawa, S. Kawarazaki, H. Nojiri, and T. Inoue, Magnetization measurements of $Fe_{1-x}co_x$Si, Journal of Magnetism and Magnetic Materials **70**, 245 (1987).

[87] O. Nakanishi, A. Yanase, A. Hasegawa, and M. Kataoka, The origin of the helical spin density wave in MnSi, Solid State Communications **35**, 995 (1980).

[88] S. V. Grigoriev, A. S. Sukhanov, and S. V. Maleyev, From spiral to ferromagnetic structure in B20 compounds: Role of cubic anisotropy, Physical Review B **91**, 224429 (2015).

[89] S. V. Maleyev, Cubic magnets with Dzyaloshinskii-Moriya interaction at low temperature, Physical Review B **73**, 174402 (2006).

[90] W. Münzer, A. Neubauer, T. Adams, S. Mühlbauer, C. Franz, F. Jonietz, R. Georgii, P. Böni, B. Pedersen, M. Schmidt, A. Rosch, and C. Pfleiderer, Skyrmion lattice in the doped semiconductor $Fe_{1-x}Co_xSi$, Physical Review B **81**, 041203 (2010).

[91] H. Oike, A. Kikkawa, N. Kanazawa, Y. Taguchi, M. Kawasaki, Y. Tokura, and F. Kagawa, Interplay between topological and thermodynamic stability in a metastable magnetic skyrmion lattice, Nature Physics **12**, 62 (2016).

[92] D. Morikawa, X. Yu, K. Karube, Y. Tokunaga, Y. Taguchi, T.-h. Arima, and Y. Tokura, Deformation of topologically-protected supercooled skyrmions in a thin plate of chiral magnet $Co_8Zn_8Mn_4$, Nano Letters **17**, 1637 (2017).

[93] Y. Okamura, F. Kagawa, S. Seki, and Y. Tokura, Transition to and from the skyrmion lattice phase by electric fields in a magnetoelectric compound, Nature Communications **7**, 12669 (2016).

[94] F. N. Rybakov, A. B. Borisov, S. Blügel, and N. S. Kiselev, New Type of Stable Particlelike States in Chiral Magnets, Physical Review Letters **115**, 117201 (2015).

[95] J. Wild, T. N. G. Meier, S. Pöllath, M. Kronseder, A. Bauer, A. Chacon, M. Halder, M. Schowalter, A. Rosenauer, J. Zweck, J. Müller, A. Rosch, C. Pfleiderer, and C. H. Back, Entropy-limited topological protection of skyrmions, Science Advances **3**, e1701704 (2017).

[96] X. Z. Yu, N. Kanazawa, Y. Onose, K. Kimoto, W. Z. Zhang, S. Ishiwata, Y. Matsui, and Y. Tokura, Near room-temperature formation of a skyrmion crystal in thin-films of the helimagnet FeGe, Nature Materials **10**, 106 (2011).

[97] A. Tonomura, X. Yu, K. Yanagisawa, T. Matsuda, Y. Onose, N. Kanazawa, H. S. Park, and Y. Tokura, Real-Space Observation of Skyrmion Lattice in Helimagnet MnSi Thin Samples, Nano Letters **12**, 1673 (2012).

[98] O. Janson, I. Rousochatzakis, A. A. Tsirlin, M. Belesi, A. A. Leonov, U. K. Rößler, J. van den Brink, and H. Rosner, The quantum nature of skyrmions and half-skyrmions in Cu_2OSeO_3, Nature Communications **5**, 5376 (2014).

[99] G. Meunier and M. Bertaud, Constantes cristallographiques de CuSe2O5, CuSeO3 et Cu2SeO4, Journal of Applied Crystallography **9**, 364 (1976).

[100] T. Adams, A. Chacon, M. Wagner, A. Bauer, G. Brandl, B. Pedersen, H. Berger, P. Lemmens, and C. Pfleiderer, Long-wavelength helimagnetic order and skyrmion lattice phase in Cu_2OSeO_3, Physical Review Letters **108**, 237204 (2012).

[101] K. Kohn, A new ferrimagnet Cu_2SeO_4, Journal of the Physical Society of Japan **42**, 2065 (1977).

[102] H. Effenberger and F. Pertlik, Die Kristallstrukturen der Kupfer(II)-oxo-selenite Cu2O(SeO3) (kubisch und monoklin) und Cu4O(SeO3)3 (monoklin und triklin)The crystal structures of the copper(II)-oxo-selenites Cu2O(SeO3) (cubic and monoclinic), and Cu4O(SeO3)3 (monoclinic and triclinic), Monatshefte für Chemie / Chemical Monthly **117**, 887 (1986).

[103] J.-W. G. Bos, C. V. Colin, and T. T. M. Palstra, Magnetoelectric coupling in the cubic ferrimagnet Cu_2OSeO_3, Physical Review B **78**, 094416 (2008).

[104] M. Belesi, I. Rousochatzakis, H. C. Wu, H. Berger, I. V. Shvets, F. Mila, and J. P. Ansermet, Ferrimagnetism of the magnetoelectric compound Cu_2OSeO_3 probed by ^{77}Se NMR, Physical Review B **82**, 094422 (2010).

[105] M. Belesi, T. Philippe, I. Rousochatzakis, H. C. Wu, H. Berger, S. Granville, I. V. Shvets, and J.-P. Ansermet, Magnetic properties of the magnetoelectric compound Cu_2OSeO_3 : Magnetization and ^{77}Se NMR study, Journal of Physics: Conference Series **303**, 012069 (2011).

[106] A. Authier, *International Tables for Crystallography, Volume D: Physical Properties of Crystals* (Springer Netherlands, 2003).

[107] N. J. Laurita, G. G. Marcus, B. A. Trump, J. Kindervater, M. B. Stone, T. M. McQueen, C. L. Broholm, and N. P. Armitage, Low-energy magnon dynamics and magneto-optics of the skyrmionic Mott insulator Cu_2OSeO_3, Physical Review B **95**, 235155 (2017).

[108] T. Schwarze, J. Waizner, M. Garst, A. Bauer, I. Stasinopoulos, H. Berger, C. Pfleiderer, and D. Grundler, Universal helimagnon and skyrmion excitations in metallic, semiconducting and insulating chiral magnets, Nature Materials **14**, 478 (2015).

[109] K. H. Miller, X. S. Xu., H. Berger, E. S. Knowles, D. J. Arenas, M. W. Meisel, and D. B. Tanner, Magnetodielectric coupling of infrared phonons in single-crystal Cu_2OSeO_3, Physical Review B **82**, 144107 (2010).

[110] V. P. Gnezdilov, K. V. Lamonova, Y. G. Pashkevich, P. Lemmens, H. Berger, F. Bussy, and S. L. Gnatchenko, Magnetoelectricity in the ferrimagnetic Cu2OSeO3: Symmetry analysis and Raman scattering study, Low Temperature Physics **36**, 550 (2010).

[111] R. B. Versteeg, I. Vergara, S. D. Schäfer, D. Bischoff, A. Aqeel, T. T. M. Palstra, M. Grüninger, and P. H. M. van Loosdrecht, Optically probed symmetry breaking in the chiral magnet Cu_2OSeO_3, Physical Review B **94**, 094409 (2016).

[112] Y. Okamura, F. Kagawa, S. Seki, M. Kubota, M. Kawasaki, and Y. Tokura, Microwave Magnetochiral Dichroism in the Chiral-Lattice Magnet Cu_2OSeO_3, Physical Review Letters **114**, 197202 (2015).

[113] M. Belesi, I. Rousochatzakis, M. Abid, U. K. Rößler, H. Berger, and J.-P. Ansermet, Magnetoelectric effects in single crystals of the cubic ferrimagnetic helimagnet Cu_2OSeO_3, Physical Review B **85**, 224413 (2012).

[114] S. Seki, S. Ishiwata, and Y. Tokura, Magnetoelectric nature of skyrmions in a chiral magnetic insulator Cu_2OSeO_3, Physical Review B **86**, 060403 (2012).

[115] Y. Okamura, F. Kagawa, M. Mochizuki, M. Kubota, S. Seki, S. Ishiwata, M. Kawasaki, Y. Onose, and Y. Tokura, Microwave magnetoelectric effect via skyrmion resonance modes in a helimagnetic multiferroic, Nature Communications **4**, 2391 (2013).

[116] S. Seki, J.-H. Kim, D. S. Inosov, R. Georgii, B. Keimer, S. Ishiwata, and Y. Tokura, Formation and rotation of skyrmion crystal in the chiral-lattice insulator, Physical Review B **85**, 220406 (2012).

[117] J. S. White, K. Prša, P. Huang, A. A. Omrani, I. Živković, M. Bartkowiak, H. Berger, A. Magrez, J. L. Gavilano, G. Nagy, J. Zang, and H. M. Rønnow, Electric-Field-Induced Skyrmion Distortion and Giant Lattice Rotation in the Magnetoelectric Insulator Cu_2OSeO_3, Physical Review Letters **113**, 107203 (2014).

[118] J. S. White, I. Levatić, A. A. Omrani, N. Egetenmeyer, K. Prša, I. Živković, J. L. Gavilano, J. Kohlbrecher, M Bartkowiak, H. Berger, and H. M. Rønnow, Electric field control of the skyrmion lattice in Cu_2 $OSeO_3$, Journal of Physics: Condensed Matter **24**, 432201 (2012).

[119] A. Chacon, L. Heinen, M. Halder, A. Bauer, W. Simeth, S. Mühlbauer, H. Berger, M. Garst, A. Rosch, and C. Pfleiderer, Observation of Two Thermodynamically Disconnected Skyrmion Phases in Cu_2OSeO_3, Nature Physics (2018), (to be published).

[120] F. Qian, H. Wilhelm, A. Aqeel, T. T. M. Palstra, A. J. E. Lefering, E. H. Brück, and C. Pappas, Dissipation phenomena and magnetic phase diagram of Cu_2OSeO_3 below 50 K, arXiv:1611.06014 [cond-mat] (2016), arXiv:1611.06014 [cond-mat] .

[121] F. Qian, H. Wilhelm, A. Aqeel, T. T. M. Palstra, A. J. E. Lefering, E. H. Brück, and C. Pappas, Dissipation phenomena and magnetic phase diagram of Cu_2OSeO_3 below 50 K, arXiv:1611.06014 [cond-mat] (2016), arXiv:1611.06014 [cond-mat] .

[122] M. Jackson, Imaginary susceptibility, a primer, The Institute for Rock Magnetism, Quaterly **13**, 1,10 (2003).

[123] M. I. Youssif, A. A. Bahgat, and I. A. Ali, AC magnetic susceptibility technique for the characterization of high temperature superconductors, Egyptian Journal of Solids **23**, 231 (2000).

[124] M. Bałanda, Ac susceptibility studies of phase transitions and magnetic relaxation: Conventional, molecular and low-dimensional magnets, Acta Physica Polonica A **124**, 964 (2013).

[125] H. G. Katzgraber, F. Pázmándi, C. R. Pike, K. Liu, R. T. Scalettar, K. L. Verosub, and G. T. Zimányi, Reversal-field memory in the hysteresis of spin glasses, Physical Review Letters **89**, 257202 (2002).

[126] C. R. Pike, C. A. Ross, R. T. Scalettar, and G. Zimanyi, First-order reversal curve diagram analysis of a perpendicular nickel nanopillar array, Physical Review B **71**, 134407 (2005).

[127] M. J. Benitez, O. Petracic, H. Tüysüz, F. Schüth, and H. Zabel, Fingerprinting the magnetic behavior of antiferromagnetic nanostructures using remanent magnetization curves, Physical Review B **83**, 134424 (2011).

[128] R. Casalini and C. M. Roland, Thermodynamical scaling of the glass transition dynamics, Physical Review E **69**, 062501 (2004).

[129] J.-P. Hansen, Clarifying the kinetic glass transition, Physics World **4**, 32 (1991).

[130] T. V. Chan, G. D. Shyu, and A. I. Isayev, Master curve approach to polymer crystallization kinetics, Polymer Engineering & Science **35**, 733 (1995).

[131] C. W. Hagen and R. Griessen, Distribution of activation energies for thermally activated flux motion in high- T c superconductors: An inversion scheme, Physical Review Letters **62**, 2857 (1989).

[132] A. Labarta, O. Iglesias, L. Balcells, and F. Badia, Magnetic relaxation in small-particle systems: Ln(t / τ 0) scaling, Physical Review B **48**, 10240 (1993).

[133] O. Iglesias, F. Badia, A. Labarta, and L. Balcells, Energy barrier distributions in magnetic systems from the Tln(t/τ0) scaling, Zeitschrift für Physik B Condensed Matter **100**, 173 (1996).

[134] I. Levatić, V. Šurija, H. Berger, and I. Živković, Dissipation processes in the insulating skyrmion compound Cu_2OSeO_3, Physical Review B **90** (2014), 10.1103/PhysRevB.90.224412.

[135] A. Bauer, M. Garst, and C. Pfleiderer, History dependence of the magnetic properties of single-crystal $Fe_{1-x}Co_xSi$, Physical Review B **93**, 235144 (2016).

[136] A. Bauer, A. Chacon, M. Wagner, M. Halder, R. Georgii, A. Rosch, C. Pfleiderer, and M. Garst, Symmetry breaking, slow relaxation dynamics, and topological defects at the field-induced helix reorientation in MnSi, Physical Review B **95**, 024429 (2017).

[137] A. Butykai, S. Bordács, L. F. Kiss, B. G. Szigeti, V. Tsurkan, A. Loidl, and I. Kézsmárki, Relaxation dynamics of modulated magnetic phases in the skyrmion host GaV_4S_8: An ac magnetic susceptibility study, Physical Review B **96**, 104430 (2017).

[138] A.-M. Racu, D. Menzel, J. Schoenes, and K. Doll, Crystallographic disorder and electron-phonon coupling in $Fe_{1-x}Co_xSi$ single crystals: Raman spectroscopy study, Physical Review B **76**, 115103 (2007).

[139] L. J. Bannenberg, K. Kakurai, F. Qian, E. Lelièvre-Berna, C. D. Dewhurst, Y. Onose, Y. Endoh, Y. Tokura, and C. Pappas, Extended skyrmion lattice scattering and long-time memory in the chiral magnet $Fe_{1-x}Co_xSi$, Physical Review B **94**, 104406 (2016).

[140] B. Gross, Time-Temperature Superposition Principle in Relaxation Theory, Journal of Applied Physics **40**, 3397 (1969).

[141] R. Li, Time-temperature superposition method for glass transition temperature of plastic materials, Materials Science and Engineering: A **278**, 36 (2000).

[142] M. Van Gurp and J. Palmen, Time-temperature superposition for polymeric blends, Rheol Bull **67**, 5 (1998).

[143] M. K. Forthaus, G. R. Hearne, N. Manyala, O. Heyer, R. A. Brand, D. I. Khomskii, T. Lorenz, and M. M. Abd-Elmeguid, Pressure-induced quantum phase transition in $Fe_{1-x}Co_xSi$ ($x = 0.1, 0.2$), Physical Review B **83**, 085101 (2011).

[144] R. V. Chamberlin, Mesoscopic model for the primary response of magnetic materials (invited), Journal of Applied Physics **76**, 6401 (1994).

[145] Y. S. Lin, P. J. Grundy, and E. A. Giess, Bubble domains in magnetostatically coupled garnet films, Applied Physics Letters **23**, 485 (1973).

[146] T. Garel and S. Doniach, Phase transitions with spontaneous modulation-the dipolar Ising ferromagnet, Physical Review B **26**, 325 (1982).

[147] S. Takao, A study of magnetization distribution of submicron bubbles in sputtered Ho-Co thin films, Journal of Magnetism and Magnetic Materials **31-34**, 1009 (1983).

[148] N. Nagaosa and Y. Tokura, Topological properties and dynamics of magnetic skyrmions, Nature Nanotechnology **8**, 899 (2013).

[149] J. H. Yang, Z. L. Li, X. Z. Lu, M.-H. Whangbo, S.-H. Wei, X. G. Gong, and H. J. Xiang, Strong Dzyaloshinskii-Moriya Interaction and Origin of Ferroelectricity in Cu_2OSeO_3, Physical Review Letters **109** (2012), 10.1103/PhysRevLett.109.107203.

[150] I. Stasinopoulos, S. Weichselbaumer, A. Bauer, J. Waizner, H. Berger, S. Maendl, M. Garst, C. Pfleiderer, and D. Grundler, Low spin wave damping in the insulating chiral magnet Cu_2OSeO_3, Applied Physics Letters **111**, 032408 (2017).

[151] F. Jonietz, S. Mühlbauer, C. Pfleiderer, A. Neubauer, W. Münzer, A. Bauer, T. Adams, R. Georgii, P. Böni, R. A. Duine, K. Everschor, M. Garst, and A. Rosch, Spin transfer torques in mnsi at ultralow current densities, Science **330**, 1648 (2010).

[152] M. Halder, *Präzisionsmessungen der Magnetisierung an Systemen mit komplexer Ordnung*, Diplomarbeit, Technische Universität München (2012).

[153] R. Ritz, M. Halder, M. Wagner, C. Franz, A. Bauer, and C. Pfleiderer, Formation of a topological non-Fermi liquid in MnSi, Nature **497**, 231 (2013).

[154] C. Pfleiderer, D. Reznik, L. Pintschovius, H. v Löhneysen, M. Garst, and A. Rosch, Partial order in the non-Fermi-liquid phase of MnSi, Nature **427**, 227 (2004).

[155] J. L. Silverberg, M. Bierbaum, J. P. Sethna, and I. Cohen, Collective Motion of Humans in Mosh and Circle Pits at Heavy Metal Concerts, Physical Review Letters **110**, 228701 (2013).